

Quarks and Pions at finite chemical potential

A study of the QCD Phase-diagram with Dyson-Schwinger equations

Pascal Gunkel

A thesis presented for the degree of
Master of Science



Supervisor: Prof. Dr. Christian Fischer
Institute for Theoretical Physics
Justus-Liebig-University Giessen
Germany March 30, 2017

Contents

1	Introduction	1
2	Theoretical framework	5
2.1	Elementary particles	6
2.1.1	Derivation of Dyson-Schwinger-equations	6
2.1.2	Introducing the medium	13
2.1.3	Quark and Gluon propagators	16
2.1.4	Quark-Gluon-Vertex	18
2.1.5	Quark renormalization	20
2.2	Bound-states	24
2.2.1	Bethe-Salpeter-equations	26
2.2.2	Normalization	31
2.2.3	Meson amplitudes	32
2.2.4	Pion decay constant	35
2.2.5	Gell-Mann-Oakes-Renner-relation	37
2.3	Observables	38
2.3.1	Symmetries and order parameters	39
2.3.2	QCD phase diagram	45
2.3.3	Silverblaze property	48
3	QCD phase diagram	50
3.1	Truncation scheme	50
3.2	Gluon renormalization	53
3.3	Results	57
3.3.1	Quark propagator	57
3.3.2	Gluon propagator	61
3.3.3	Chiral symmetry order parameter	63
3.3.4	QCD phase diagram	65
4	Quarks and pions in cold dense matter	67
4.1	Truncation scheme	67
4.2	Results for the quark propagator and the QCD phase diagram	69

4.2.1	Quark propagator and condensate in chiral limit	69
4.2.2	Quark propagator and condensate for cold dense matter	70
4.2.3	QCD phase diagram	77
4.3	Pion equations in vacuum and for finite chemical potential	78
4.4	Results for the pion in vacuum and for finite chemical potential	80
4.4.1	Pion in vacuum	80
4.4.2	Pion for finite chemical potential	82
5	Conclusion and outlook	88
A	Conventions	90
A.1	Dirac-part	90
A.1.1	Spin-1-particles	91
A.1.2	Spin- $\frac{1}{2}$ -particles	92
A.1.3	Euclidean space	94
A.1.4	Momentum space	96
A.2	Color and flavor part	96
B	Projected equations	99
B.1	Projected DSE's	99
B.1.1	Vacuum	100
B.1.2	Finite temperature	101
B.1.3	Cold dense matter	102
B.2	Projected BSE's	104
B.2.1	Meson amplitude normalization	106
B.2.2	Meson decay constant	106
C	Numerical details	108
C.1	Momentum integrals in vacuum and medium	108
C.2	Numerical treatment of the momentum integrals	111
C.3	Thermal mass calculation	116
C.4	Renormalization, order parameter and the phase diagram calculation	116
C.5	Numerical details of the pion	118

Chapter 1

Introduction

“The world would indeed be a dull place if there were no distinction among the different phases of matter.”

- Leo P. Kadanoff in [1].

This sentence stems from one of the most important pioneers concerning the theory of phase transitions: Leo P. Kadanoff. He significantly contributed to the development of a modern and comprehensive theory of phase transitions and critical phenomena, including universality and scaling behaviors. In his book *“Statistical Physics: Statics, Dynamics and Renormalization”*, he starts the chapter about phase transitions with the same quote I decided to start this thesis. He relates it to physical phase transitions of the daily experience, e.g. the separation of “oil” and “water” or “snowflakes” and “sitting water” as well as the separation between “sky” and “earth”. But it is also applicable to the elementary particles, known today. If there would be no separation of the different phases of these particles, the world as we know it, with all its complexity and beauty, would not exist. Instead, the world would be a uniform soup of the elementary particles, as it was at the beginning of time. With this in mind, we want to study the different phases of elementary particles today, which will help us understand how matter formed 13,8 billion years ago.

Nowadays, elementary particles are theoretically described by the general relativity and the quantum mechanical local gauge groups $SU_C(3) \otimes SU_L(2) \otimes U_Y(1)$. The latter two gauge groups thereby describe the electroweak interaction, which is a unification of the weak and electromagnetic interaction. It includes effects like the decay of particles and the attraction or the repulsion of particles due to their electromagnetic charge. On the other hand, the local non-Abelian gauge group $SU_C(3)$ is the foundation of a quantum mechanical gauge theory, also known as quantum-chromo-dynamic (QCD), which describes the strong interaction. In this gauge theory a “color-charge” for every elementary particle and a corresponding “color-force”

are introduced. This color-force, however, is important on lengths scales of physical particles and is much stronger than the other three fundamental interactions (gravitational, electro-magnetic and weak nuclear). Additionally, the color-force binds the colored elementary particles to colorless bound-states and these in turn to nuclei. In comparison to the electro-magnetic theory, which can be expanded in terms of the electro-magnetic coupling constant e , QCD's coupling constant is too big for an expansion parameter and thus we need to calculate non-perturbatively to describe processes including the strong interaction. Related to this, QCD provides a description for two interesting non-perturbative phenomena, namely color-confinement and spontaneous chiral symmetry breaking. Furthermore, breaking the chiral symmetry causes another phenomenon, which is known as the dynamical mass generation. While the absence of any colored particle in the particle detectors is related to the color-confinement, the masses of most of the colorless bound-state particles can not result from the Higgs-mechanism only. In most cases, the Higgs-mechanism generates a small fraction of the bound-state masses. The remaining part is explained by the dynamical generation of mass, in addition with anomalies. The mentioned two phenomena of the QCD depend on the thermodynamic circumstance and serve as classification for the different states of matter in QCD and in consequence for the elementary particles, too. The information, which state of strongly interacting matter occurs depending on the temperature, is combined in the QCD phase diagram. The latest data to this phase diagram within a Dyson-Schwinger approach can be found in reference [2].

The true manifestation of the QCD phase diagram is subject to many experimental and theoretical studies and one of the main goals of the compressed baryonic matter (CBM) experiment at the future facility for antiproton and ion research (FAIR) in Darmstadt. Existing operations, like the relativistic heavy ion collider (RHIC) at the Brookhaven national lab (BNL) or the large hadron collider (LHC) at CERN, already explored parts of the phase diagram, but until now experiments could not reassure the theoretical prediction of a critical end point (CEP). The technical limitations of these experiments make it difficult to reach the high density region, needed for the exploration of this critical end point. In order to study the phase transition, these experiments accelerate heavy ions to large fraction of the speed of light, before colliding them. This creates a zone of hot dense matter, which is equal under certain conditions to the quark-gluon-plasma (QGP) that the theoretical calculations predict at high temperatures and densities. The zone later expands and therefore cools down, to end up in a phase of ordinary hadrons.

On the theoretical side, there are multiple approaches to investigate the QCD phase diagram. On one hand dynamical theoretical systems can be considered. In this case, the system either is described by a transport theory of relativistic quantum many-body systems or a local equilibrium is assumed for the nearly perfect fluid of the QGP. In the latter approach the equation of state is used as input. On the other hand, there are static approaches to the full theory of QCD. In this domain, lattice QCD and functional methods have to be mentioned. But also effective QCD models, like the (Polyakov-loop extended) Nambu-Jona-Lasinio ((P)NJL) or the quark meson ((P)QM) model, are of importance. However, these effective models do not consider

gluons (elementary particles that mediate the strong interaction) as active degrees of freedom. Even though the lattice QCD approach is an ab initio approach, which discretises the theory on a finite space-time grid and uses statistic Monte-Carlo simulations, it suffers from the so-called fermion sign problem, as well as finite volume effects. The fermion sign problem states that the exponential function in the generating functional features an oscillatory contribution due to finite chemical potential values. Consequently, the results are well established for zero density, but rely on extrapolations for chemical potentials fulfilling $\frac{\mu q}{T} < 1$. Above this constrain, an extrapolation is not possible. For reviews to lattice QCD in medium see references [3] and [4]. To access the whole QCD phase diagram and the Yang-Mills sector, it remains to consider functional methods. These functional methods are based on the expansion of the theory in terms of correlation functions of the elementary particles. Consequently we get access to the fundamental degrees of freedom of the QCD, from which we can extract observables such as bound-state properties or order parameters for chiral symmetry and confinement. The trade-off using this approach, however, is that the calculation methods rely on truncations, which are less controlled as in lattice Monte-Carlo simulations. Within the field of functional methods, there are first of all the s-called functional renormalization group (FRG) methods. These methods are based on differential equations for the Green-functions. For reviews see references [5] and [6]. Another formalism of importance is the Dyson-Schwinger approach, which deals with an infinite tower of coupled integral equations. For reviews see reference [7] and [8].

In the last couple of years, much effort has been made to study the properties of the QCD phase diagram within the Dyson-Schwinger approach. Two main areas of research exist: On the one hand, we have the exploration of the true manifestation of the QCD phase diagram and the improvement of its calculation trough an improvement of the truncations and approximations as well as the inclusion of e.g. additional flavors [9], [10]. On the other hand, the study of thermodynamic quantities and the elementary degrees of freedom in certain areas of the QCD phase diagram is a point of interest. Thermodynamic quantities such as pressure, quark number or chiral susceptibility as well as quark spectral or baryon number densities have been studied [11]–[13]. Also the critical scaling and quantities like the quark-gluon-vertex or the quark spectral function have been investigated [2], [14]–[16]. Furthermore, the true manifestation of the phase diagram is still an open question. Thereby, the existence of most of the phases is confirmed, but the behavior of the coexistence lines and the existence of a critical end point are still an object of intense study. Investigations of the two color version of lattice QCD ($SU_C(2)$), for example, suggest that hadronic effects are crucial for the QCD phase diagram. Reference [17] showed, that the existence of the critical end point is affected by the two color equivalent of baryonic effects. Until now, only “*baryon effects on the location of QCD’s critical end point*” are taken into account, see therefore reference [18]. Mesonic back-coupling effects, on the other hand, were only studied in vacuum so far (see for example reference [19] or [20]). But these mesonic effects could be important for the QCD phase diagram. At zero temperature and physical quark masses, the meson back-coupling is dominated by the exchange of the lightest mesons (pions). Consequently, one can estimate the influence of the mesonic back-coupling onto

the phase diagram and the critical end point by calculating the pion back-coupling for finite chemical potential. For this purpose, we calculate the properties of the elementary particles and the pions for the QCD phase diagram, using the Dyson-Schwinger approach. Especially the case of finite chemical potential and vanishing temperature will be important in this work.

We will start this work by introducing the necessary theoretical framework for the calculations in chapter 2. For this purpose, we will separately discuss the elementary particles in section 2.1 and the bound-states in section 2.2. In both chapters, we first will derive the equation of state in the Dyson-Schwinger approach, before we generally discuss the properties of the basic ingredients of these equations. Later on we will mention some details to the observables in section 2.3, including the main symmetries which are important for the QCD phase diagram. The QCD phase diagram itself and the related order parameters of the symmetries will be discussed there, too. Afterwards, two different truncation schemes in chapter 3 and 4 will be studied. In the first one, describing the most elaborated truncation scheme so far, the results for the quark and gluon propagators in section 3.3.1 and 3.3.2 as well as the corresponding results for the order parameter for chiral symmetry in section 3.3.3 and the newest QCD phase diagram in section 3.3.4 will be studied in detail. The second truncation scheme, representing an adequate toy model, includes the QCD phase diagram in chiral limit in section 4.2.3 and the new results for the quark propagator at finite chemical potential and vanishing temperature in section 4.2.2. Additionally we will discuss the new results of the pion at finite chemical potential and vanishing temperature in section 4.4.2 in comparison to the vacuum case in section 4.4.1. Finally, we will conclude in chapter 5. The conventions and numerics used in this work are shown in Appendix A and C. The equations necessary for the calculation of the results for the different truncations, however, are derived and presented in Appendix B.

Chapter 2

Theoretical framework

The most important step of every theoretical physicist is to set a verifiable, comprehensible and reproducible theoretical foundation which describes the desired part of nature correctly and completely and which has predictive capability too. Therefore we will begin this thesis by setting the necessary framework of the theory, which is used throughout this work. As starting point we need an object, which contains all information of the given theory. The desired object - in a quantum-field theory like QCD - is given by the generating functional. So far, every approach to describe the Quantum-chromo-dynamic (QCD) is derived from it and up to a certain point the approaches are equivalent to the generating functional.

As already mentioned before, we will use the functional Dyson-Schwinger approach. In this approach, system-describing equations are derived from the generating functional, whose solutions are the Green-functions of the elementary particles and the N-particle bound-states. The corresponding equations are called the Dyson-Schwinger equations (DSE's) for elementary particles and Bethe-Salpeter equations (BSE's) for two-particle bound-states. These equations are the quantum equations of motion for an n-point function of a given theory and are represented by an infinite tower of coupled integral equations. If they are solved completely and self-consistently, the approach is *ab initio*. But since this is numerically not possible, it further relies on truncations (approximations), which have to be chosen very carefully to conserve all important properties of the theory. Two possible truncation schemes are detailed in the following chapters. Nonetheless, only if the equations of the Dyson-Schwinger approach are solved self-consistently and without truncations, the solutions are equivalent to the generating functional and contain therefore all information to the given theory.

In the following we will at first focus on the description of elementary particles with DSE's, discussing the general properties of the Green-functions. Then we will take a closer look on the bound-states, described by the BSE's and finally we will conclude by considering the symmetries and observables of QCD.

2.1 Elementary particles

In this section we want to explore the elementary particles within the Dyson-Schwinger approach. These elementary particles are the fundamental degrees of freedom of the QCD. Nowadays the components of the nucleon - the quarks and their gauge bosons the gluons - are confirmed as elementary particles of the strong interaction. In the non-Abelian QCD the necessary fixing of the gauge of the gluon is not trivial and introduces a further auxiliary field. This field is called the ghost field. Using the Dyson-Schwinger-equation (DSE) we are not only able to determine the Green-function's of the quark and gluon, but also the Green-function of this field, too. For this purpose, however, we need a connection between the Dyson-Schwinger equations and the generating functional first.

2.1.1 Derivation of Dyson-Schwinger-equations

To derive the Dyson-Schwinger equations for arbitrary actions from first principles, we begin with the generating functional for partially connected Green-function's in vacuum. This generating functional is defined by

$$Z[J] = \mathcal{N} \int \mathcal{D}\varphi e^{i(S[\varphi] - \int_x \varphi(x)J(x))} \quad (2.1)$$

where $S[\varphi] = \int_x \mathcal{L}(\varphi(x), \partial_\mu \varphi(x))$ describes the action of the considered system, \int_x is a shortcut for $\int d^4x$ and φ represents a super-field, which contains all fields of the system. We add an external source term $J(x)$ to the action, so that we are able to derive all Green-function's via functional derivatives of the generating functional $Z[J]$ with respect to the external source $J(x)$ and later setting $J(x) = 0$.

$$\begin{aligned} G_n(x_1 \dots x_n) &= \langle 0 | \hat{T} \{ \hat{\varphi}(x_1) \dots \hat{\varphi}(x_n) \} | 0 \rangle = \frac{\int \mathcal{D}\varphi e^{iS[\varphi]} \varphi(x_1) \dots \varphi(x_n)}{\int \mathcal{D}\varphi e^{iS[\varphi]}} \\ &= \frac{i^n \delta^n}{\delta J(x_1) \dots \delta J(x_n)} \frac{Z[J]}{Z[0]} \Big|_{J=0} \end{aligned} \quad (2.2)$$

The Dyson-Schwinger equations result from the local translation invariance of this generating functional. Since we are integrating over all field configurations, the variation according to the field transformation

$$\varphi(x) \longrightarrow \varphi'(x) = \varphi(x) + \epsilon(x) \quad (2.3)$$

is only a redefinition of the generating functional and therefore the Path-integral is not affected. Because the integral measure $\mathcal{D}\varphi = \prod_i d\varphi(x_i)$ is invariant under the mentioned local translation

transformation, the invariance of the Path-integral $Z'[J] = Z[J]$ yields

$$\begin{aligned} Z'[J] &= \mathcal{N} \int \mathcal{D}\varphi' e^{i(S[\varphi'] - \int_x \varphi'(x)J(x))} = \mathcal{N} \int \mathcal{D}\varphi e^{i(S[\varphi] - \int_x \varphi(x)J(x))} e^{i \int_x \epsilon(x) \left[\frac{\delta S[\varphi]}{\delta \varphi(x)} - J(x) \right]} \\ &= Z[J] \left\langle e^{i \int_x \epsilon(x) \left[\frac{\delta S[\varphi]}{\delta \varphi(x)} - J(x) \right]} \right\rangle_J \stackrel{!}{=} Z[J] \end{aligned} \quad (2.4)$$

where we used the Taylor-expansion $S[\varphi'] = S[\varphi] + \int_x \epsilon(x) \frac{\delta S[\varphi]}{\delta \varphi(x)}$. As result of this translation invariance we get the so-called Master-DSE

$$\left\langle \frac{\delta S[\hat{\varphi}]}{\delta \hat{\varphi}(x)} \right\rangle_J = J(x) \quad (2.5)$$

which describes the quantum-mechanical expectation value of the classical equation of motion for intact dependency from the external source $J(x)$. At this point, it is necessary to clarify the definition of the mentioned vacuum expectation value (VEV) with intact dependency from the external source, to be able to derive the DSE's from the Master-equation. Consequently we will consider the generalization of the VEV to an arbitrary function $f(\varphi)$ of the super-field at different space-time-points. Furthermore the external source J will be set to zero, only after the derivations. In the following we consequently will keep the dependency on the external source J "intact".

$$\langle f(\hat{\varphi}) \rangle_J := \frac{\int \mathcal{D}\varphi e^{i(S[\varphi] - \int_x \varphi(x)J(x))} f(\varphi)}{\int \mathcal{D}\varphi e^{i(S[\varphi] - \int_x \varphi(x)J(x))}} = \frac{1}{Z[J]} f\left(\frac{i\delta}{\delta J}\right) Z[J] \quad (2.6)$$

With this equation it is possible to translate classical relation between fields ($f(\varphi) = 0$) - such as the classical equations of motion or symmetry relations - into quantum-mechanical identities ($\langle f(\hat{\varphi}) \rangle = 0$). The equation states, that we have to interpret the classical fields φ as field operators $\hat{\varphi}$ and take the vacuum expectation value (expectation value over the quantum-fluctuations of the super-field in vacuum) of the classical relation, to get the quantum-mechanical analog. The translation rule of this connection, between the classical equation and the quantum-mechanical analog, depends on the kind of the generating functional that we use. In the upper case, we inserted the generating functional of partially connected Green-functions. If we further consider the connection ($\frac{Z[J]}{Z[0]} = e^{iW[J]}$) between the generating functionals for partially connected ($Z[J]$) and connected Green-function's ($W[J]$) and use the relation $e^{-x} f(\partial) e^x = f(\partial + \partial x)$, we get a simplified equation

$$\langle f(\hat{\varphi}) \rangle_J = e^{-iW[J]} f\left(\frac{i\delta}{\delta J}\right) e^{iW[J]} = f\left(-\frac{\delta W[J]}{\delta J} + \frac{i\delta}{\delta J}\right) \quad (2.7)$$

Consequently, the translation rule for the transformation from a classical relation ($f(\varphi) = 0$) to a quantum-mechanical identity, using the generating functional for connected Green-function's, is to exchange the argument of the classical relation φ by $-\frac{\delta W[J]}{\delta J} + \frac{i\delta}{\delta J}$. As example, we consider

the (connected) two- and four-point Green-function, which are given by

$$\begin{aligned}
 G_2(x_1x_2) &= \langle 0 | \hat{T} \{ \hat{\varphi}(x_1) \hat{\varphi}(x_2) \} | 0 \rangle_{J=0} = -iW_{x_1x_2}[0] = G_2^{con}(x_1x_2) \\
 G_4(x_1x_2x_3x_4) &= \langle 0 | \hat{T} \{ \hat{\varphi}(x_1) \dots \hat{\varphi}(x_4) \} | 0 \rangle_{J=0} = G_2^{con}(x_1x_2)G_2^{con}(x_3x_4) + \\
 &\quad + G_2^{con}(x_1x_3)G_2^{con}(x_2x_4) + G_2^{con}(x_1x_4)G_2^{con}(x_2x_3) + G_4^{con}(x_1x_2x_3x_4) \quad (2.8)
 \end{aligned}$$

In this equation we used the shortcut $W_{x_1\dots x_i\dots x_m}[J]$ for $\frac{\delta^l}{\delta x_1\dots\delta x_i\dots\delta x_m}W[J]$ and the descriptions $G_{con}(x_ix_j) = -iW_{x_ix_j}[0]$ and $G_{con}(x_1x_2x_3x_4) = iW_{x_1x_2x_3x_4}[0]$ for the connected Green-functions. While the generating functional $Z[J]$ generates all partially connected n-point Green-function's and $W[J] = -i \ln \left(\frac{Z[J]}{Z[0]} \right)$ generates all connected n-point Green-function's, which enter into the scattering-matrix, we search for the n-point, one-particle-irreducible (1PI) Green-function's, which represent the irreducible contribution to the n-point interaction vertex without redundancies. It is noteworthy that we can calculate the partially connected Green-function's by the connected ones by the equations above (see equation (2.8)) and the connected ones by the (1PI) Green-function's by summing them. This reduces our problem to the task of calculating all (1PI) Green-function's.

We get the (1PI) Green-function's by functional derivative of the effective action $\Gamma[\tilde{\varphi}]$, which is related to the generating functional of the connected Green-function's via Legendre-transformation.

$$\frac{Z[J]}{Z[0]} = e^{iW[J]} = e^{i(\Gamma[\tilde{\varphi}] - \int_z \tilde{\varphi}(z)J(z))} \quad \Leftrightarrow \quad W[J] = \Gamma[\tilde{\varphi}] - \int_z \tilde{\varphi}(z)J(z) \quad (2.9)$$

The effective action depends on the averaged field $\tilde{\varphi}$, instead of the external source J . Thereby the averaged field $\tilde{\varphi}$ is the vacuum expectation value of the field operator $\hat{\varphi}$ with intact J-dependency.

$$\tilde{\varphi}(x) = -\frac{\delta W[J]}{\delta J(x)} = \frac{i}{Z[J]} \frac{\delta Z[J]}{\delta J(x)} = \langle \hat{\varphi}(x) \rangle_J \quad (2.10)$$

For the physical limit $J \rightarrow 0$, the averaged field vanishes ($J = 0 \Leftrightarrow \tilde{\varphi} = 0$). Generally this is not valid in case of spontaneous symmetry breaking, but a redefinition of the averaged field is possible, so that the vacuum expectation value vanishes again.

We introduced the effective action and the averaged field, but what is their meaning? The averaged field and the effective action are the quantum-mechanical expectation values of a classical field and a classical action. Via the quantum-mechanical expectation value we add and integrate over all Quantum-fluctuations of the system, since we integrate over all possible field configurations.

$$\frac{\int \mathcal{D}\varphi e^{i(S[\varphi] - \int_x \varphi(x)J(x))}}{\int \mathcal{D}\varphi e^{iS[\varphi]}} = e^{i(\Gamma[\tilde{\varphi}] - \int_x \tilde{\varphi}(x)J(x))} \quad (2.11)$$

In the same manner as the classical action $S[\varphi]$ contains all the content of the classical field theory, the generating functionals $Z[J]$, $W[J]$ and $\Gamma[\tilde{\varphi}]$ determine the Quantum-field theory

completely, since all the Green-functions can be derived from them. For further derivations we introduce the shortcuts

$$W_{x_1 \dots x_n}^{(n)}[J] = \frac{\delta^n W[J]}{\delta J(x_1) \dots \delta J(x_n)} \quad \text{and} \quad \Gamma_{x_1 \dots x_n}^{(n)}[\tilde{\varphi}] = \frac{\delta^n \Gamma[J]}{\delta J(x_1) \dots \delta J(x_n)} \quad (2.12)$$

In the following, the task is to translate the equation (2.7) to the effective action, to get a transformation rule from classical relations to 1PI-Identities. Based on the definition of the effective action as Legendre-transformation of the generating functional for connected Green-functions, we know that the sources $J(x)$ and $\tilde{\varphi}(x)$ are ‘‘conjugated sources’’.

$$W'_x[J] = -\tilde{\varphi}(x) \quad \Gamma'_x[\tilde{\varphi}] = J(x) \quad (2.13)$$

Further we claim, that the 1PI two-point function $\Gamma''_{xy}[\tilde{\varphi}]$ is the inverse of the connected two point function $W''_{xy}[J]$ which we can see, considering

$$\int_y W''_{xy}[J] \Gamma''_{yz}[\tilde{\varphi}] = - \int_y \frac{\delta \tilde{\varphi}(x)}{\delta J(y)} \frac{\delta J(y)}{\delta \tilde{\varphi}(z)} = - \frac{\delta \tilde{\varphi}(x)}{\delta \tilde{\varphi}(z)} = -\delta^4(x-z)$$

Consequently the 1PI two-point function is the inverse propagator $\Gamma''_{xy}[\tilde{\varphi}]^{-1} = -W''_{xy}[J] = \Delta_{xy}[\tilde{\varphi}] \xrightarrow[J \rightarrow 0]{\tilde{\varphi} \rightarrow 0} -iG_2(x, y)$ and all higher derivatives are defined as 1PI n-point vertexes $\Gamma_{x \dots z}^{(n)}[0]$.

Utilizing the connection between the conjugated sources

$$\frac{\delta}{\delta J(x)} = \int_y \frac{\delta \tilde{\varphi}(y)}{\delta J(x)} \frac{\delta}{\delta \tilde{\varphi}(y)} = \int_y \Delta_{xy}[\tilde{\varphi}] \frac{\delta}{\delta \tilde{\varphi}(y)} \quad (2.14)$$

we get the remaining piece to express equation (2.7) with the effective action for 1PI-identities.

$$\langle f(\hat{\varphi}) \rangle_J = f \left(\tilde{\varphi} + \int_y \Delta_{xy}[\tilde{\varphi}] \frac{\delta}{\delta \tilde{\varphi}(y)} \right) \quad (2.15)$$

Finally, we find the connection between the generating functional and the DSE's to be the Master-DSE for 1PI n-point functions

$$\Gamma'_x(\tilde{\varphi}) = \frac{\delta S}{\delta \varphi(x)} \left(\tilde{\varphi} + \int_y \Delta_{xy}[\tilde{\varphi}] \frac{i\delta}{\delta \tilde{\varphi}(y)} \right) \quad (2.16)$$

If we, however, consider the other way around, we also can express the generating functional by the sum over all Green-functions

$$Z[J] = Z[0] \sum_{n=0}^{\infty} \frac{i^n}{n!} \int d^4x_1 \dots d^4x_n J(x_1) \dots J(x_n) G_n(x_1 \dots x_n) \quad (2.17)$$

which shows the analogy of the DSE's and the generating functional, too.

QCD action in vacuum

Up to this point, we considered the DSE's for arbitrary actions. But in the following we will apply the DSE algorithm onto the QCD. Therefore, we need at first the QCD action. This action can be deduced in analogy to the QED case, considering that the QCD has a much more complicate gauge group and obeying the postulates of local gauge invariance, Poincaré-invariance, renormalizability and P- or T-invariance. The most elaborated action, which fulfills these conditions, is given by

$$S[A, \bar{\Psi}, \Psi] = \int_x \left\{ \bar{\Psi}_{a,i}^f(x) \left(i[\gamma^\mu]_{ab} D_\mu^{ij}(x) - [\mathbb{1}_D]_{ab} [\mathbb{1}_c]^{ij} m^f \right) \Psi_{b,j}^f(x) - \frac{1}{4} F_{\mu\nu}^g(x) F_g^{\mu\nu}(x) \right\} \quad (2.18)$$

with the Dirac-spinors of the quark and antiquark fields $\Psi_{b,j}^f(x)$ and $\bar{\Psi}_{a,i}^f(x)$ and the field strength tensor $F_{\mu\nu}^{ij}(x) = [D_\mu(x), D_\nu(x)]^{ij}$ as well as the covariant derivative $D_\mu^{ij}(x) = [\mathbb{1}_c]^{ij} \partial_\mu - ig \mathcal{A}_\mu^{ij}(x)$ and the $SU_C(N_c)$ gauge (gluon) fields $\mathcal{A}_\mu^{ij}(x) = A_\mu^g(x) [t_g]^{ij}$, which mediate the strong interaction. The constants g and m^f describe the unrenormalized strong coupling constant and the current quark mass of the flavor f , generated by the Higgs mechanism. While the spinors of the quark fields transform under the $SU_C(N_c)$ gauge transformation as elements of the fundamental representation of $SU_C(N_c)$, the gauge fields are given in the adjoint representation. In both cases, the group generators t_g fulfill the Lie algebra $[t_g, t_h] = if_{ghl} t_l$. The representations for the Dirac-matrices and $SU_C(N_c)$ -generators are given in the Appendix A. While the Dirac-part is described by the Lorentz-indices μ and ν as well as the Dirac-indices a and b , the color-part is represented by the $(N_c^2 - 1)$ -tet color index g and the N_c -tet color indices i and j . N_c describes the number of colors, which is in QCD fixed to three. Using the Lie-algebra mentioned earlier we can write the field-strength tensor as follows

$$\begin{aligned} F_{\mu\nu}^{ij}(x) &= \partial_\mu \mathcal{A}_\nu^{ij}(x) - \partial_\nu \mathcal{A}_\mu^{ij}(x) - ig [\mathcal{A}_\mu(x), \mathcal{A}_\nu(x)]^{ij} \\ &= \left[\partial_\mu A_\nu^g(x) - \partial_\nu A_\mu^g(x) + gf_{ghl} A_\mu^h(x) A_\nu^l(x) \right] [t_g]^{ij} = F_{\mu\nu}^g(x) [t_g]^{ij} \end{aligned} \quad (2.19)$$

where f_{ghl} is the totally antisymmetric and real structure constant. The last term in the first line in particular is the result of the non-Abelian character of $SU_C(N_c)$ and leads to the self-interaction of the gluon. In the Abelian case of QED, it is easy to see that the last term vanishes. This further implies that there is no self-interaction between the gauge bosons (Photons) of the $U(1)$ gauge group of QED. As next step we take a closer look at the given $SU_C(N_c)$ gauge transformation. Due to the local gauge transformation the (anti-) quark and gluon fields transform as following

$$\begin{aligned} \Psi_{b,j}^f(x) &= U_{ji}(x) \Psi_{b,i}^f(x), & \bar{\Psi}_{b,j}^f(x) &= \bar{\Psi}_{b,i}^f(x) U_{ij}^\dagger(x) & \text{and} \\ \mathcal{A}_{ij}^\mu(x) &= U_{il}(x) \left(\mathcal{A}_{lk}^\mu(x) + \frac{i}{g} [\mathbb{1}_c]_{lk} \partial^\mu \right) U_{kj}^\dagger(x) = U_{il}(x) \mathcal{A}_{lk}^\mu(x) U_{kj}^\dagger(x) + \frac{i}{g} U_{il}(x) \left(\partial^\mu U_{lj}^\dagger(x) \right) \end{aligned} \quad (2.20)$$

with the local gauge transformation matrix

$$U_{ji}(x) = \left[e^{i\epsilon(x)} \right]_{ji} = \left[e^{i \sum_g \epsilon_g(x) t_g} \right]_{ji} \quad (2.21)$$

acting on the color part of the (anti-) quark and the gluon. Due to the gauge transformation 2.20 a subset of the gauge fields is connected and has therefore the same physical content. This, however, leads to an over-counting in the generating functional. As a consequence it is necessary to reduce the integration to a subset of the gauge space, where no gauge field configurations can be transformed into each other by gauge transformation. This is done by fixing the gauge. A possible way to do so, was introduced by Faddeev and Poppov. The result of this procedure is the appearance of an additional gauge fixing action term, which depends on two further fields $c_a(x)$ and $\bar{c}_a(x)$. These Grassman fields are the so-called Faddeev-Poppov ghost and antighost fields. In case of the Lorenz gauge fixing condition $f[A] = \partial_\mu A_g^\mu = 0$, the additional action term is given by

$$S_{GF}[A, c, \bar{c}] = - \int_x \frac{(\partial_\mu A_g^\mu)^2}{2\xi} + \int_x \bar{c}_g(x) \partial_\mu D_{gh}^\mu(x) c_h(x) \quad (2.22)$$

with the unrenormalized gauge parameter ξ and the covariant derivative $D_{gh}^\mu(x)$ in the adjoint representation. g and h are therefore $(N_c^2 - 1)$ -tet color indices. Until now the fields and the constants are unrenormalized. But to cancel the appearing infinities, we have to introduce a regulator and renormalization constants. While the regulator removes the infinities by introducing a regulator dependency, the renormalization constants transform this regulator dependence into a renormalization point dependence. After the renormalization procedure the renormalized constants of the theory $(m_R(\mu), g_R(\mu))$ have to be insert as experimental data at a given scale: the renormalization point. In case of the QCD, we have to introduce a renormalization constant for the quark wave-function Z_2 , the quark mass Z_m and the strong coupling constant Z_g as well as for the gluon propagator Z_3 , the ghost propagator \tilde{Z}_3 and the gauge fixing parameter Z_ξ . The connections between the unrenormalized and renormalized quantities are therefore given by

$$\begin{aligned} \Psi(\Lambda) &= Z_2^{1/2}(\Lambda, \mu) \Psi_R(\mu), & A(\Lambda) &= Z_3^{1/2}(\Lambda, \mu) A_R(\mu), & c(\Lambda) &= \tilde{Z}_3^{1/2}(\Lambda, \mu) c_R(\mu), \\ m(\Lambda) &= Z_m(\Lambda, \mu) m_R(\mu), & g(\Lambda) &= Z_g(\Lambda, \mu) g_R(\mu), & \xi(\Lambda) &= Z_\xi^{-1}(\Lambda, \mu) \xi_R(\mu) \end{aligned} \quad (2.23)$$

where Λ represents the regulator and μ the renormalization point. Via the Slavnov-Taylor identities we can transform some of the renormalization constants in the more convenient (vertex) renormalization constants

$$Z_1 = Z_g Z_3^{3/2}, \quad \tilde{Z}_1 = Z_g \tilde{Z}_3 Z_3^{1/2}, \quad Z_{1F} = Z_g Z_2 Z_3^{1/2}, \quad Z_4 = Z_g^2 Z_3^2 \quad (2.24)$$

where the renormalization constant Z_1 describes the three-gluon vertex, \tilde{Z}_1 the ghost-gluon vertex, Z_{1F} the quark-gluon-vertex and Z_4 the four-gluon vertex. Using these renormalization constants, the renormalized Lorenz gauge fixed QCD action in vacuum and in Minkowski space

is given by

$$\begin{aligned}
 S_{QCD}[A, \bar{\Psi}, \Psi, c, \bar{c}] = & \int_x \left[Z_2 \bar{\Psi}_{R,a,i}^f(x) \left(i[\gamma^\mu]_{ab} [\mathbb{1}_C]_{ij} \partial_\mu - Z_m [\mathbb{1}_D]_{ab} [\mathbb{1}_C]_{ij} m_R^f \right) \Psi_{R,b,j}^f(x) + \right. \\
 & + Z_{1F} g_R \bar{\Psi}_{R,a,i}^f(x) [\gamma^\mu]_{ab} [t_g]^{ij} A_{R,\mu}^g(x) \Psi_{R,b,j}^f(x) + Z_3 \frac{1}{2} A_{R,\mu}^g(x) (\square g^{\mu\nu} - \partial^\nu \partial^\mu) A_{R,\nu}^g(x) \\
 & - Z_1 \frac{g_R}{2} f_{ghl} \left[\partial^\mu A_{R,g}^\nu(x) - \partial^\nu A_{R,g}^\mu(x) \right] A_{R,\mu}^h(x) A_{R,\nu}^l(x) + Z_\xi Z_3 \frac{A_{R,g}^\nu(x) \partial_\mu \partial_\nu A_{R,g}^\mu(x)}{2\xi_R} \\
 & - Z_4 \frac{g_R^2}{4} f_{gko} f_{ghl} A_{R,k}^\mu(x) A_{R,o}^\nu(x) A_{R,\mu}^h(x) A_{R,\nu}^l(x) + g_R \tilde{Z}_1 f_{kgh} (\partial_\mu \bar{c}_{R,g}(x)) A_{R,k}^\mu(x) c_{R,h}(x) \\
 & \left. + \tilde{Z}_3 \bar{c}_{R,g}(x) \square c_{R,g}(x) \right] \tag{2.25}
 \end{aligned}$$

QCD Dyson-Schwinger equations in vacuum

To calculate the Dyson-Schwinger equations, it is advisable to transform this action into the Euclidean momentum space and to introduce a graphical notation for the propagators, vertices and operations. The transformation into the Euclidean momentum space is done using the rules shown in Appendix A.1.3 and A.1.4. The introduction of a graphical notation and the derivation of the DSE's is done in reference [21]. As result we get the following set of coupled DSE's for the dressed quark $S_{ab}^{f,ij}(p)$, gluon $D_{\epsilon\nu}^{gh}(k)$ and ghost $G^{gh}(k)$ propagators

$$\begin{aligned}
 [S_{ab}^{f,ij}(p)]^{-1} &= [S_{0,ab}^{f,ij}(p)]^{-1} + \Sigma_{ab}^{f,ij}(p) \\
 [D_{\epsilon\nu}^{gh}(k)]^{-1} &= [D_{0,\epsilon\nu}^{gh}(k)]^{-1} + \Pi_{\epsilon\nu}^{gh}(k) \\
 [G^{gh}(k)]^{-1} &= [G_0^{gh}(k)]^{-1} + \Omega^{gh}(k)
 \end{aligned} \tag{2.26}$$

and the corresponding bare propagators

$$\begin{aligned}
 [S_{0,ab}^{f,ij}(p)]^{-1} &= Z_2^f(\Lambda, \mu) \left[i[\not{p}]_{ab} + [\mathbb{1}]_{ab} Z_m^f(\Lambda, \mu) m_R^f(\mu) \right] \delta_{ij} \\
 [D_{0,\epsilon\nu}^{gh}(k)]^{-1} &= Z_3(\Lambda, \mu') k^2 \left[P_{\epsilon\nu}^{\mathcal{T}}(k) + P_{\epsilon\nu}^{\mathcal{L}}(k) \frac{Z_\xi(\Lambda, \mu')}{\xi} \right] \delta_{gh} \\
 [G_0^{gh}(k)]^{-1} &= \tilde{Z}_3(\Lambda, \mu') k^2 \delta_{gh}
 \end{aligned} \tag{2.27}$$

where the covariant transversal $P_{\epsilon\nu}^{\mathcal{T}}(k)$ and longitudinal $P_{\epsilon\nu}^{\mathcal{L}}(k)$ (four momentum) projectors are defined by

$$\begin{aligned}
 P_{\epsilon\nu}^{\mathcal{T}}(k) &= \left(\delta_{\epsilon\nu} - \frac{k_\epsilon k_\nu}{k^2} \right) \\
 P_{\epsilon\nu}^{\mathcal{L}}(k) &= \frac{k_\epsilon k_\nu}{k^2}
 \end{aligned} \tag{2.28}$$

As one can see, all three bare propagators are diagonal in color space and the gluon and the ghost are furthermore independent of the flavor of the quark. One could also say, that the gluon is flavor blind. It only remains to state the corresponding self-energies of the field. Since the

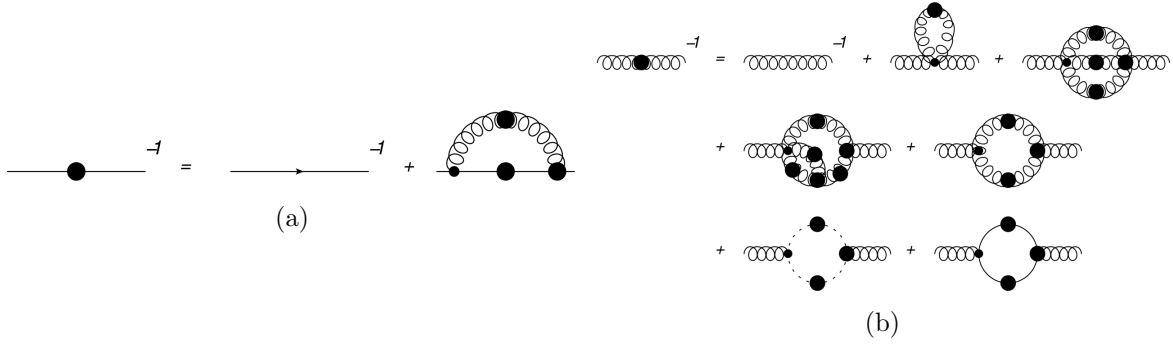


Figure 2.1: In the quark (a) and gluon (b) DSE, the curly lines represent gluon propagators, while the quark propagators are defined by solid lines and ghost propagators by dashed lines. Dressed propagators are marked by a dot. The remaining are bare one. Furthermore, multiple vertices (quark-gluon, ghost-gluon, three-gluon, four-gluon) are included in the equations. The dressed ones are again marked by a big dot, while the bare one are given by small dots. These figures are taken from [22].

ghost propagator will not be the matter of study in this work, it is not necessary to indicate it. The same applies to the Yang-Mills part of the gluon. Therefore we split the gluon self-energy into the (purely gluonic) Yang-Mills part $\Pi_{YM;\epsilon\nu}^{gh}(k)$ and a quark-back-coupling term $\Pi_{QL;\epsilon\nu}^{gh}(k)$. The quark and gluon self-energies are therefore given by

$$\begin{aligned}\Sigma_{ab}^{f,ij}(p) &= - \int_q \left[\Gamma_{0,\epsilon}^{f,g}(p, q, k) \right]_{ad}^{il} S_{de}^{f,lo}(q) \left[\Gamma_{\nu}^{f,h}(p, q, k) \right]_{eb}^{oj} D_{\epsilon\nu}^{gh}(k) \\ \Pi_{\epsilon\nu}^{gh}(k) &= \Pi_{YM;\epsilon\nu}^{gh}(k) + \Pi_{QL;\epsilon\nu}^{gh}(k) \\ \Pi_{QL;\epsilon\nu}^{gh}(k) &= \frac{1}{2} \sum_f^{N_f} \int_q \left[\Gamma_{0,\epsilon}^{f,g}(p, q, k) \right]_{ad}^{il} S_{de}^{f,lo}(q) \left[\Gamma_{\nu}^{f,h}(p, q, k) \right]_{eb}^{oj} S_{ba}^{f,ji}(p)\end{aligned}\quad (2.29)$$

While the expression $\left[\Gamma_{0,\epsilon}^{f,g}(p, q, k) \right]_{ad}^{il} = iZ_{1F}^f g[\gamma_\epsilon]_{ad}[t_g]_{il}$ describes a bare quark-gluon-vertex, $\left[\Gamma_{\nu}^{f,h}(p, q, k) \right]_{eb}^{oj} = ig[t_h]_{oj} \left[\Gamma_{\nu}^f(p, q, k) \right]_{eb}$ is a dressed one. Also noteworthy is the momentum routing of the quark self-energy and the quark back-coupling term, which we will from now on refer to as quark-loop. For the first one we have the momentum routing $k = q - p$ and correspondingly for the quark-loop $p = q - k$. Finally we can conclude by showing the graphical notation of the coupled Dyson-Schwinger equations of the quark and the gluon in figure 2.1. While figure 2.1a represents the quark DSE, figure 2.1b shows the untruncated gluon DSE. In the latter one, the last term defines a sum over the quark-loops of all quark flavors ($\equiv \Pi_{QL;\epsilon\nu}^{gh}(k)$). The remaining terms, however, represent the Yang-Mills part of the gluon ($\equiv \Pi_{YM;\epsilon\nu}^{gh}(k)$).

2.1.2 Introducing the medium

Until now we derived the quark and gluon DSE's for the vacuum case. In this section, however, we want to generalize our description of QCD to finite temperature and finite chemical potential. Consequently it is necessary to find a connection between the already known thermodynamic quantities and quantum field theory. While the quantum-mechanical system in quantum field

theory is completely described by the generating functional, the partition function contains all information to the thermodynamic system for a given set of the natural variables. There are multiple possible ensembles, but the ensembles relevant for our investigation are:

- Microcanonical ensemble: isolated system with fixed energy, volume and particle number, described by the microcanonical partition function $Z_{mc} = \text{tr} [\Pi(E, V, N)]$
- Canonical ensemble: closed system which is in contact to a heat bath, the energy is only known on average, described by the canonical partition function $Z_c = \text{tr} [e^{-\beta H}]$
- Grand canonical ensemble: System which is in contact with a heat bath and possible particle exchange, the energy and the particle number are both only known on average

To introduce the temperature and the chemical potential, we have to consider the last one. The grand canonical ensemble is therefore described by the partition function

$$Z_{gc}(\beta, \mu_q) = \text{tr} \left(e^{-\beta(\hat{H} - \mu_q \hat{N})} \right) = \sum_n e^{-\beta(E_n - \mu_q N_n)} = \int_q \langle q | e^{-\beta(\hat{H} - \mu_q \hat{N})} | q \rangle \quad (2.30)$$

At this point, we remember that we can represent the particle number operator by particle field operators:

$$\hat{N} = \int d^4x \hat{\Psi}^\dagger \hat{\Psi} = \int d^4x \hat{\Psi} \gamma_0 \hat{\Psi} \quad (2.31)$$

Using this property, we can redefine the Hamilton operator \hat{H}' , so that it includes the chemical potential term. But the connection between thermodynamics and QFT is still missing. For this purpose, we consider the generating functional of a system with the action $S(t, t') = \int_t^{t'} d\tilde{t} \int d^3x \mathcal{L}$ in Minkowski-space

$$Z_{gen}(x', t'; x, t) = \langle x'(t') | x(t) \rangle = \mathcal{N} \int_{x(t)}^{x'(t')} \mathcal{D}x(t'') e^{iS(t, t')} \quad (2.32)$$

For the next steps, there are two strategies to follow, the real time and the imaginary time formalism. We will use the latter one, by introducing the Euclidean time

$$\tau = -it \quad (2.33)$$

and translating the generating functional of the vacuum in the Euclidean space. This yields

$$Z_{gen}(x', -i\tau'; x, -i\tau) = \langle x'(-i\tau') | x(-i\tau) \rangle = \langle x' | e^{-\hat{H}(\tau' - \tau)} | x \rangle = \mathcal{N} \int_{x(\tau)}^{x'(\tau')} \mathcal{D}x(\tau'') e^{-S_E(\tau, \tau')} \quad (2.34)$$

with the Euclidean action $S_E(\tau, \tau') = \int_\tau^{\tau'} d\tau'' \int d^3x \mathcal{H}$. If we compare the penultimate step of the latest equation with the partition function of the grand canonical ensemble (2.30), expressed

in the continual basis, we find the desired connection

$$Z_{gc}(\beta, \mu_q) = \int dx Z_{gen}(x, -i\beta; x, 0) = \mathcal{N} \int_{x(0)=x(\beta)} \mathcal{D}x(\tau) e^{-S_E(0,\beta) + \mu_q \int_0^\beta d\tau \int d^3x \hat{\Psi} \gamma_0 \hat{\Psi}} \quad (2.35)$$

and additionally a periodicity condition $x(\tau + \beta) = x(\tau)$. By applying this to higher spin states, instead of scalar particles, we get the boundary conditions

$$\begin{aligned} \Psi(x, \tau) &= -\Psi(x, \tau + \beta) && \text{for fermionic fields and} \\ \Phi(x, \tau) &= +\Phi(x, \tau + \beta) && \text{for bosonic fields.} \end{aligned} \quad (2.36)$$

Finally we have everything at hand to derive the DSE's in medium. The derivation of the DSE's proceed analog to the vacuum case, with the difference that the temporal direction of the action has a finite integration interval and that we have a periodicity condition. Because of those two properties the Fourier transformation

$$f(\tau) = T \sum_{n_q} e^{-i\omega_q^{B/F}(T)\tau} f(\omega_q^{B/F}(T)) \quad , \quad f(\omega_q^{B/F}(T)) = \int_0^\beta d\tau e^{i\omega_q^{B/F}(T)\tau} f(\tau) \quad (2.37)$$

yields, that the fourth momentum component is now discrete and we have to sum over it instead of integrating it. Due to the different periodicity conditions we additionally get two different discret energies: the bosonic $\omega_q^B(T)$ and the fermionic $\omega_q^F(T)$ Matsubara frequencies. Further we introduce a shorthand notation for the medium case

$$\tilde{\omega}_p(T, \mu_q) = \omega_p^F(T) + i\mu_q, \quad \omega_p^F(T) = \pi T (2n_p + 1), \quad \omega_p^B(T) = 2\pi T n_p, \quad (p) = (\vec{p}^2, \omega_p(T); \mu_q) \quad (2.38)$$

At the end we can sum the differences to the vacuum case. Every four-dimensional momentum integral has to be exchanged by $T \sum_{n_q} \int \frac{d^3q}{(2\pi)^3} = \mathcal{F}_q$ and every function depends now separately on the spatial momentum \vec{p} and the corresponding Matsubara frequency ω_p . If we apply this knowledge onto the vacuum quark and gluon DSE's presented in the section before, we get

$$\begin{aligned} \Sigma_{ab}^{f,ij}(p) &= - \mathcal{F}_q \left[\Gamma_{0,\epsilon}^{f,g}(p, q, k) \right]_{ad}^{il} S_{de}^{f,lo}(q) \left[\Gamma_{\nu}^{f,h}(p, q, k) \right]_{eb}^{oj} D_{\epsilon\nu}^{gh}(k) \\ \Pi_{QL;\epsilon\nu}^{gh}(k) &= \frac{1}{2} \mathcal{F}_q \left[\Gamma_{0,\epsilon}^{f,g}(p, q, k) \right]_{ad}^{il} S_{de}^{f,lo}(q) \left[\Gamma_{\nu}^{f,h}(p, q, k) \right]_{eb}^{oj} S_{ba}^{f,ji}(p) \end{aligned} \quad (2.39)$$

for the quark self-energy and the quark-loop. As one can see in the following equations the bare quark and gluon propagator are much more affected:

$$\begin{aligned} \left[S_{0,ab}^{f,ij}(p) \right]^{-1} &= Z_2^{f,vac}(\Lambda, \mu) \left[i\vec{p}[\vec{\gamma}]_{ab} + i\tilde{\omega}_p(T, \mu_q)[\gamma_4]_{ab} + [\mathbf{1}]_{ab} Z_m^{f,vac}(\Lambda, \mu) m_R^f(\mu) \right] \delta_{ij} \\ \left[D_{0,\epsilon\nu}^{gh}(k) \right]^{-1} &= Z_3^{vac}(\Lambda, \mu') k^2 \left[P_{\epsilon\nu}^T(k) + P_{\epsilon\nu}^L(k) + P_{\epsilon\nu}^{\mathcal{L}}(k) \frac{Z_\xi^{vac}(\Lambda, \mu')}{\xi} \right] \delta_{gh} \end{aligned} \quad (2.40)$$

In the tensor-structure of the bare quark and gluon propagator we can observe, that the introduction of a temperature and the resulting Matsubara-formalism is accompanied by an explicit introduction of an assigned direction for the heat-bath, which breaks the O(4)-invariance of the momentum space. In the bare propagators the Euclidean four momentum splits into a spatial part and it's fourth (heat-bath/Matsubara part) component. A separation of the Dirac tensor-structure (γ_4 and $\vec{\gamma}$) in case of the quark and of the Lorenz tensor-structure ($P_{\epsilon\nu}^T(k)$ and $P_{\epsilon\nu}^L(k)$) in case of the gluon is the result. In case of the gluon, projectors transversal $P_{\epsilon\nu}^T(k)$ and longitudinal $P_{\epsilon\nu}^L(k)$ to heat bath (the fourth component of the momentum) have to be defined, which are given by

$$\begin{aligned} P_{\epsilon\nu}^T(k) &= \left(\delta_{\epsilon\nu} - \frac{k_\epsilon k_\nu}{\vec{k}^2} \right) (1 - \delta_{\epsilon 4})(1 - \delta_{\nu 4}) = \left(\delta_{ij} - \frac{k_i k_j}{\vec{k}^2} \right) \delta_{\epsilon i} \delta_{\nu j} \\ P_{\epsilon\nu}^L(k) &= P_{\epsilon\nu}^{\mathcal{J}}(k) - P_{\epsilon\nu}^T(k) \end{aligned} \quad (2.41)$$

If, additionally, the temperature is turned off, the sum over the fourth component of the momentum becomes an integral again, but the fourth component and the spatial momentum of the quark have to be keep separate in the functions, since the chemical potential still breaks O(4)-invariance. For this special case of cold and dense matter, we define the shortcuts

$$\tilde{p}_4(\mu_q) = p_4 + i\mu_q \quad (p) = (\vec{p}^2, p_4; \mu_q) \quad (2.42)$$

While the bare gluon propagator is the same as in the medium case, the bare quark propagator is given by

$$\left[S_{0,ab}^{f,ij}(p) \right]^{-1} = Z_2^{f,vac}(\Lambda, \mu) \left[i\vec{p}[\vec{\gamma}]_{ab} + i\tilde{p}(\mu_q)[\gamma_4]_{ab} + [\mathbf{1}]_{ab} Z_m^{f,vac}(\Lambda, \mu) m_R^f(\mu) \right] \delta_{ij} \quad (2.43)$$

Finally we have a good foundation for the following investigation. We only need to take a closer look at the dressed quark and gluon propagators as well as the dressed quark-gluon-vertex.

2.1.3 Quark and Gluon propagators

To calculate the dressed quark and gluon propagator we have to assume tensor-structures and assign them with dressing functions. The assumption of a tensor-structure is therefore guided by the already known structure of the bare quark and gluon propagators, which are given in equation (2.40). If we take this into consideration, we get the following ansatz for the dressed quark.

$$\begin{aligned} \left[S_{ab}^{f,ij}(p) \right]^{-1} &= \left[i\vec{p}[\vec{\gamma}]_{ab} A^f(\vec{p}^2, \omega_p) + i\tilde{\omega}_p(T)[\gamma_4]_{ab} C^f(\vec{p}^2, \omega_p) + [\mathbf{1}]_{ab} B^f(\vec{p}^2, \omega_p) \right] \delta_{ij} \\ S_{ab}^{f,ij}(p) &= \left[-i\vec{p}[\vec{\gamma}]_{ab} \sigma_A^f(\vec{p}^2, \omega_p) - i\tilde{\omega}_p(T)[\gamma_4]_{ab} \sigma_C^f(\vec{p}^2, \omega_p) + [\mathbf{1}]_{ab} \sigma_B^f(\vec{p}^2, \omega_p) \right] \delta_{ij} \end{aligned} \quad (2.44)$$

In this equation, the lower (upper) equation describes the tensor-structure of the (inverse) dressed quark propagator in Euclidean space-time and for the medium case. The propagator is

therefore described by Dirac (a and b), flavor (f) and N_c -color indices (i and j). For the lower equation we additionally used the shortcut $\sigma_X^f(\vec{p}^2, \omega_p) = \frac{X^f(\vec{p}^2, \omega_p)}{\vec{p}^2 A_f^2(\vec{p}^2, \omega_p) + \tilde{\omega}_p^2(T) C_f^2(\vec{p}^2, \omega_p) + B_f^2(\vec{p}^2, \omega_p)}$ with $X \in \{A, B, C\}$.

For obvious reasons and in analogy to the vacuum case, $A^f(\vec{p}^2, \omega_p)$ and $C^f(\vec{p}^2, \omega_p)$ are called vector dressing functions and $B^f(\vec{p}^2, \omega_p)$ scalar dressing function. Combined they give the renormalization point invariant - but not renormalization group invariant - dynamical quark mass $M^f(\vec{p}^2, \omega_p) = \frac{B^f(\vec{p}^2, \omega_p; \mu)}{A^f(\vec{p}^2, \omega_p; \mu)}$ and the quark wave-function renormalization $Z_F^f(\vec{p}^2, \omega_p; \mu) = \frac{1}{A^f(\vec{p}^2, \omega_p; \mu)}$. In medium there exists a fourth contribution to the quark propagator, which can be represented by $i\tilde{\omega}_p \vec{p} \vec{\gamma} D(\vec{p}^2, \omega_p)$. For this term there exists no counterpart in the bare propagator and its contribution is only present at finite temperatures. Because of this negligible contribution also at higher temperatures and chemical potential, we will not take this term under consideration.

Due to the color structure of the bare quark propagator, the dressed quark propagator is assumed to be color diagonal and because of the separation of the tensor-structure (γ_4 and $\vec{\gamma}$) in the bare propagator, an introduction of a second vector dressing function $C(\vec{p}^2, \omega_p)$ is necessary. Since both vector dressing functions degenerate only in vacuum and for high four momenta, we see that the Matsubara-formalism breaks the O(4)-symmetry of the momentum space. For approaching the vacuum ($T = 0, \mu_q = 0$) the vector dressing functions approach each other and the momentum gets the original O(4)-form $p_\epsilon = (\vec{p}, \tilde{\omega}_p(T)) \xrightarrow[\mu_q=0]{T=0} (\vec{p}, p_4)$ yielding the following tensor-structure.

$$\begin{aligned} \left[S_{ab}^{f,ij}(p; \mu) \right]^{-1} &= \left[i[\not{p}]_{ab} A^f(p^2, \mu) + [\mathbf{1}]_{ab} B^f(p^2, \mu) \right] \delta_{ij} = \frac{\delta_{ij}}{Z_F^f(p^2, \mu)} \left[i[\not{p}]_{ab} + [\mathbf{1}]_{ab} M^f(p^2) \right] \\ S_{ab}^{f,ij}(p, \mu) &= \frac{-i[\not{p}]_{ab} A^f(p^2, \mu) + [\mathbf{1}]_{ab} B^f(p^2, \mu)}{p^2 A_f^2(p^2, \mu) + B_f^2(p^2, \mu)} \delta_{ij} = Z_F^f(p^2, \mu) \frac{-i[\not{p}]_{ab} + [\mathbf{1}]_{ab} M^f(p^2)}{p^2 + M_f^2(p^2)} \delta_{ij} \end{aligned} \quad (2.45)$$

In case of cold dense matter the dressed quark propagator matches with the dressed propagator detailed in equation (2.44), only the discrete fermionic Matsubara frequency $\omega_p(T) = \pi T(2n_p + 1)$ has to be exchanged by the continuous fourth momentum p_4 . Analog to the dressed quark, the ansatz for the dressed gluon in Euclidean space-time and for the in medium case is given by

$$\begin{aligned} D_{\epsilon\nu}^{gh}(k) &= \left(P_{\epsilon\nu}^T(k) \frac{Z_T(\vec{k}^2, \omega_k)}{k^2} + P_{\epsilon\nu}^L(k) \frac{Z_L(\vec{k}^2, \omega_k)}{k^2} + P_{\epsilon\nu}^{\mathcal{L}}(k) \frac{\xi}{k^2} \right) \delta_{gh} \\ \left[D_{\epsilon\nu}^{gh}(k) \right]^{-1} &= \left(P_{\epsilon\nu}^T(k) \frac{k^2}{Z_T(\vec{k}^2, \omega_k)} + P_{\epsilon\nu}^L(k) \frac{k^2}{Z_L(\vec{k}^2, \omega_k)} + P_{\epsilon\nu}^{\mathcal{L}}(k) \frac{k^2}{\xi} \right) \delta_{gh} \end{aligned} \quad (2.46)$$

with the four-momentum $k^2 = \vec{k}^2 + \omega_k^2$, the bosonic Matsubara frequencies $\omega_k(T) = 2\pi T n_k$, the gauge parameter ξ , Lorentz-indices ϵ and ν and the $N_c^2 - 1$ -tet-color indices g and h . Like for the quark, the dressed gluon propagator is assumed to be color diagonal, due to the structure of the bare gluon propagator. In medium, the dressing function for the gluon propagator splits up into

two parts: one longitudinal $Z_L(\vec{k}^2, \omega_k)$ (chromoelectric dressing function) and one transversal $Z_T(\vec{k}^2, \omega_k)$ (chromomagnetic dressing function) to the heat bath. The corresponding projectors are defined in equation (2.41). For approaching the vacuum, both dressing functions degenerate to the same dressing function $Z(k^2; \mu', \xi)$, yielding the following tensor-structure

$$\begin{aligned} D_{\epsilon\nu}^{gh}(k^2; \mu', \xi) &= \left(P_{\epsilon\nu}^{\mathcal{T}}(k) \frac{Z(k^2; \mu', \xi)}{k^2} + P_{\epsilon\nu}^{\mathcal{L}}(k) \frac{\xi}{k^2} \right) \delta_{gh} \\ \left[D_{\epsilon\nu}^{gh}(k^2; \mu', \xi) \right]^{-1} &= \left(P_{\epsilon\nu}^{\mathcal{T}}(k) \frac{k^2}{Z(k^2; \mu', \xi)} + P_{\epsilon\nu}^{\mathcal{L}}(k) \frac{k^2}{\xi} \right) \delta_{gh} \end{aligned} \quad (2.47)$$

In case of cold dense matter, the dressed gluon propagator corresponds to the one of the vacuum, but only if we consider a quenched theory. Considering a unquenched theory, it is given by equation (2.46). Naturally, one has to exchange the discrete Matsubara frequencies ω_k by the fourth momentum component k_4 in equation (2.46). Normally the quark and gluon dressing functions and the propagators further depend implicitly on the renormalization point of the quark μ (and gluon μ'), the temperature T , the quark chemical potential μ_q and the gauge parameter ξ , but in the following we will drop the indication of these dependencies for the sake of simplicity, except for section where it is useful. The Dirac and color indices will be dropped too. For this purpose, we have to take the color-trace of the corresponding DSE or compare the resulting color structure. This procedure will be discussed after the truncation and renormalization in the next chapters.

2.1.4 Quark-Gluon-Vertex

Apart from the quark and gluon propagator there is another important component that has to be investigated: the quark-gluon-vertex. The general form of this vertex is given by

$$[\Gamma_{f,h}^{\nu}(P, k)]_{oj}^{eb} = ig [t_h]_{oj} \otimes \sum_{i=1}^{12} F_i^f(P^2, P \cdot k, k^2) [\tau_i^{\nu}(P, k)]_{eb} \quad (2.48)$$

with the vertex dressing functions $F_i^f(P^2, P \cdot k, k^2)$, Dirac basis elements $\tau_i^{\nu}(P, k)$ and color basis elements t_h . The Dirac structure is characterized by the Lorentz index ν and Dirac indices e and b . Since we consider gluons with N_c color flavors, h is an $(N_c^2 - 1)$ -tet color index and o and j are N_c -tet color indices. The representation of the color basis elements is given in Appendix A. In the following, only the flavor index f and the Dirac structure will be mentioned. Therefore we omit the Dirac indices and factorize out the color basis elements using

$$\Gamma_{\nu}^{f,h}(P, k) = igt_h \Gamma_{\nu}^f(P, k) \quad (2.49)$$

A possible representation of the remaining Dirac basis elements, in this reduced vertex, can be written as

$$\tau_{\nu}^i(P, k) \in \{\gamma_{\nu}, P_{\nu}, k_{\nu}\} \times \{\mathbb{1}, \not{k}, \not{P}, [\not{k}, \not{P}]\} \quad (2.50)$$

with the relative momentum $P_\mu = \frac{q_\mu + p_\mu}{2}$ between the quarks and the incoming gluon momentum $k_\mu = q_\mu - p_\mu$. q and p are therefore the outgoing and incoming quark momenta. Induced from the color current conservation, a vector Slavnov-Taylor identity constrains the longitudinal part ($\sim k_\nu$) of the vertex, by relating it to the quark and ghost propagators:

$$k^\nu \Gamma_\nu^f(p, q, k) = G(k^2) \left[\bar{H}(p, q) S_f^{-1}(q) - S_f^{-1}(p) H(p, q) \right] \quad (2.51)$$

with the ghost dressing function G and the quark-ghost scattering kernel H and its conjugate \bar{H} . This identity is not solved in QCD, but by assuming $H(p, q) = \bar{H}(p, q) \approx \tilde{H}(k^2)$, we get a relation, which resembles an Abelian Ward-Takahashi-Identity in Euclidean space-time multiplied with a $G\tilde{H}$ -factor.

$$\begin{aligned} \Gamma_\nu^f(p, q, k) &= G(k^2) \tilde{H}(k^2) \tilde{\Gamma}_\nu^f(p, q, k) \\ k^\nu \tilde{\Gamma}_\nu^f(p, q, k) &= \left[S_f^{-1}(q) - S_f^{-1}(p) \right] \end{aligned} \quad (2.52)$$

This Abelian Ward-Takahashi-Identity then serves to express parts of the vertex dressing function in terms of quark dressing functions. For finite temperature the Ward-Takahashi-Identity can be transformed into the following equation, by inserting the quark dressing functions

$$\begin{aligned} k_\nu \Gamma_\nu^{f,BC}(P, k) &= k_\nu \left[i \Sigma_A \gamma_i \delta_{i\nu} + i \Sigma_C \gamma_4 \delta_{4\nu} + 2 \left[(\vec{P})_i \delta_{i\nu} + \omega_P \delta_{4\nu} \right] \cdot \right. \\ &\quad \left. \cdot \left(i \Delta_A \vec{P} \vec{\gamma} + i \Delta_C \tilde{\omega}_P \gamma_4 + \Delta_B \right) \right] \end{aligned} \quad (2.53)$$

with the abbreviations

$$\Sigma_X := \frac{X^f(\vec{q}^2, \omega_q) + X^f(\vec{p}^2, \omega_p)}{2}, \quad \Delta_X := \frac{X^f(\vec{q}^2, \omega_q) - X^f(\vec{p}^2, \omega_p)}{q^2 - p^2} \quad (2.54)$$

and $X^f(\vec{q}^2, \omega_q)$ representing the quark dressing functions. If we consider the differential Ward-Takahashi-identity for $k^2 \rightarrow 0$, to ensure the analyticity of the vertex, we get

$$\begin{aligned} \Gamma_\nu^{f,BC}(P, 0) &= \frac{dS_f^{-1}(P)}{dP^\nu} = i A^f(P^2, \omega_P) \gamma_i \delta_{i\nu} + i C^f(P^2, \omega_P) \gamma_4 \delta_{4\nu} + 2 \left[(\vec{P})_i \delta_{i\nu} + \omega_P \delta_{4\nu} \right] \cdot \\ &\quad \cdot \left(i A'_f(P^2, \omega_P) \vec{P} \vec{\gamma} + i C'_f(P^2, \omega_P) \tilde{\omega}_P \gamma_4 + B'_f(P^2, \omega_P) \right) \end{aligned} \quad (2.55)$$

which is the same equation as we get by setting $k^2 \rightarrow 0$ in equation (2.53), yielding $\Sigma_X \rightarrow X^f(P^2, \omega_P)$ and $\Delta_X \rightarrow X'_f(P^2, \omega_P)$. Considering both equations the most general expression for the quark-gluon-vertex under the assumption above (2.52) and for finite temperature in Euclidean space-time, is given by

$$\begin{aligned} \Gamma_\nu^f(p, q, k) &= G(k^2) \tilde{H}(k^2) \left[i \Sigma_A \gamma_i \delta_{i\nu} + i \Sigma_C \gamma_4 \delta_{4\nu} + [(\vec{p} + \vec{q})_i \delta_{i\nu} + (\omega_p + \omega_q) \delta_{4\nu}] \cdot \right. \\ &\quad \left. \cdot \left(\frac{i}{2} \Delta_A (\vec{p} + \vec{q}) \vec{\gamma} + \frac{i}{2} \Delta_C (\tilde{\omega}_p + \tilde{\omega}_q) \gamma_4 + \Delta_B \right) \right] + P_{\nu\lambda}^{\mathcal{Z}}(k) \Gamma_\lambda^{f,T}(p, q, k) \end{aligned} \quad (2.56)$$

The first part is the already mentioned Ball-Chiu vertex, multiplied with a $G\tilde{H}$ -factor and the second term is a transversal contribution. This transversal contribution can be constructed from the eight basis elements $\sim \vec{\gamma}, \gamma_4, \vec{P}, \omega_P$ (correspondingly for the vacuum γ_μ, P_μ) and has to satisfy $\Gamma_\nu^T(P, 0) = 0$, to obey the Ward-Takahashi-identity. A transverse part is possible too, since it is not restricted by the Slavnov-Taylor-Identity or the Ward-Takahashi-Identity. Furthermore it is unknown, if the exact solution of the Slavnov-Taylor-identity leads to the same Ball-Chiu structure. The vacuum version of this quark-gluon-vertex is given by

$$\Gamma_\nu^f(p, q, k) = G(k^2)\tilde{H}(k^2) \left[i\Sigma_A \gamma_\nu + (p+q)_\nu \left(\frac{i}{2} \Delta_A (\not{p} + \not{q}) + \Delta_B \right) \right] + P_{\nu\lambda}^{\mathcal{J}}(k) \Gamma_\lambda^{f,T}(p, q, k) \quad (2.57)$$

For cold dense matter we have once more to set the discrete fermionic Matsubara frequency $\omega_p(T) = \pi T(2n_p + 1)$ to the continuous fourth momentum p_4 .

2.1.5 Quark renormalization

In this section we want to cancel the appearing divergences of the quark propagator by fixing the quark wave-function renormalization constant $Z_2^{f,vac}(\mu, \Lambda)$ and quark mass renormalization constant $Z_m^{f,vac}(\mu, \Lambda)$, given in the bare quark propagator (2.27). But before we are able to introduce and fix the renormalization constants, we have to introduce a regulator and regularization scheme to classify and separate the divergences. Since, numerically, we are only able to integrate a finite interval, the upper ultraviolet O(4)-cutoff Λ serves as regulator and separates the appearing divergences in vacuum and medium. For this purpose, we are restricted to use a MOM regularization scheme. To cancel the divergence, appearing with this regulator, we impose a renormalization condition in vacuum and transfer the regulator-dependency (in this case the UV-cutoff Λ) into a dependency of the quark renormalization point μ and some external input given at this point. This external input is the running current quark mass $m_R^f(\mu)$ at the quark renormalization point μ , which is fixed by experimental data. In case of confined quarks and gluons we are not able to insert experimental data for the quark mass itself, but we fix the quark mass by the Gell-Mann-Oakes-Renner (GMOR) relation via the experimental pion m_π or kaon mass m_K .

Before we can derive equations for the renormalization constants, we have to mention the scaling behavior of the renormalization constants. The renormalization constants $Z_2^{f,vac}(\mu, \Lambda)$ and $Z_m^{f,vac}(\mu, \Lambda)$ connect the bare quark mass $m_0^f(\Lambda)$ with the renormalized quark mass $m_R^f(\mu)$ and the unrenormalised $A_0^f(p, \Lambda)$ with the renormalized $A^f(p, \mu)$ vector dressing function (similar for the scalar dressing function $B^f(p, \mu)$):

$$\begin{aligned} m_0^f(\Lambda) &= Z_m^{f,vac}(\mu, \Lambda) m_R^f(\mu) \\ A_0^f(p, \Lambda) &= \left[Z_2^{f,vac}(\mu, \Lambda) \right]^{-1} A^f(p, \mu) \\ B_0^f(p, \Lambda) &= \left[Z_2^{f,vac}(\mu, \Lambda) \right]^{-1} B^f(p, \mu) \end{aligned} \quad (2.58)$$

As result we get the following connection between the renormalized $S^f(p, \mu; m_R)$ and the unrenormalized $S_B^f(p, \Lambda; m_0)$ quark propagator.

$$\begin{aligned} S^f(p, \mu; m_R) &= \frac{-i[\not{p}]A^f(p, \mu) + [\mathbf{1}]B^f(p, \mu)}{p^2 A_f^2(p, \mu) + B_f^2(p, \mu)} = Z_2^{f,vac}(\Lambda, \mu) \frac{-i[\not{p}]A_0^f(p, \Lambda) + [\mathbf{1}]B_0^f(p, \Lambda)}{p^2 A_{0,f}^2(p, \Lambda) + B_{0,f}^2(p, \Lambda)} \\ &= Z_2^{f,vac}(\Lambda, \mu) S_B^f(p, \mu; m_0) \end{aligned} \quad (2.59)$$

This scaling behavior with the quark wave-function renormalization constants is a consequence from the multiplicative renormalizability and implies, that we are able to factorize the quark wave-function renormalization constant out of the self-energy. Consequently we can define a new self-energy $\Sigma = Z_2^{f,vac}(\Lambda, \mu)\tilde{\Sigma}$. For the discussion of the renormalization we have to project onto the quark tensor-structure. To do so, we calculate the quark dressing functions by taking the Dirac trace (see therefore Appendix A.1.2)

$$X(p) = \text{tr}_D (T_X S^{-1}(p)) \quad (2.60)$$

and using projectors defined by

$$T_A(p) = \frac{-i\not{p}}{4p^2} \quad , \quad T_B(p) = \frac{\mathbf{1}}{4} \quad (2.61)$$

in vacuum and

$$T_A(p) = \frac{-i\vec{p}\vec{\gamma}}{4p^2} \quad , \quad T_B(p) = \frac{\mathbf{1}}{4} \quad , \quad T_C(p) = \frac{-i\gamma_4}{4\tilde{\omega}_p} \quad \text{or} \quad T_C(p) = \frac{-i\gamma_4}{4\tilde{p}_4} \quad (2.62)$$

in medium. Further on, we need to project the self-energy onto the quark tensor-structure, defining

$$\Sigma_X(p) = \text{tr}_D (T_X \tilde{\Sigma}(p)) \quad (2.63)$$

Vacuum renormalization

With this in mind, we will fix the renormalization constants, by imposing a renormalization condition of the form

$$S_f^{-1}(\mu) = i\not{\mu} + \mathbf{1}m_R^f(\mu) \quad (2.64)$$

or equally expressed with dressing functions by

$$A(\mu, \mu) = 1 \quad \text{and} \quad B(\mu, \mu) = m_R^f(\mu) \quad (2.65)$$

We then can compute the renormalization constants from the quark DSE, given in equation (2.26). This is done by projecting onto the quark tensor-structures using the relation (2.61) and the trace rules given in the Appendix A.1.2. Expressed with the projected self-energies (2.63),

the renormalization constants are given by

$$\begin{aligned} Z_2^{f,vac}(\Lambda, \mu) &= \frac{1}{1 + \Sigma_A(\mu, \Lambda)} \\ Z_2^{f,vac}(\Lambda, \mu) Z_m^{f,vac}(\Lambda, \mu) &= 1 - \frac{\Sigma_B(\mu, \Lambda)}{m_R^f(\mu) (1 + \Sigma_A(\mu, \Lambda))} \end{aligned} \quad (2.66)$$

As result we get the following equations for the quark dressing functions in vacuum

$$\begin{aligned} A(p, \mu) &= \frac{1 + \Sigma_A(p, \Lambda)}{1 + \Sigma_A(\mu, \Lambda)} \\ B(p, \mu) &= \begin{cases} m_R^f(\mu) + \frac{\Sigma_B(p, \Lambda) - \Sigma_B(\mu, \Lambda)}{1 + \Sigma_A(\mu, \Lambda)} & \text{if } m_R^f(\mu) \neq 0 \\ \frac{\Sigma_B(p, \Lambda)}{1 + \Sigma_A(\mu, \Lambda)} & \text{if } m_R^f(\mu) = 0 \end{cases} \end{aligned} \quad (2.67)$$

In-medium renormalization

In medium we restrict ourselves to the same $O(4)$ -UV-cutoff regulator Λ . For the case of finite temperature, we therefore will limit the three momentum to $\vec{q}^2 < \Lambda^2 - \omega_q^2(T)$, while we sum over all Matsubara frequencies, obeying the condition $|\omega_q(T)| < \Lambda$. In case of cold dense matter, however, the limit of the three momentum is $\vec{q}^2 < \Lambda^2 - q_4^2$ and we integrate separately over the spatial \vec{q} and the fourth momentum component q_4 . The latter is integrated in the interval $[-\Lambda, \Lambda]$. For more numerical details see Appendix C.1. Further, we know that finite temperature and chemical potential does not introduce new divergences [23]. Consequently, we use the renormalization constants from the vacuum case, with the same parameters (cutoffs, renormalization points and renormalized quark mass value), to calculate the dressing functions.

$$\begin{aligned} A(\vec{p}^2, \omega_p; \mu) &= Z_2^{f,vac}(\Lambda, \mu) (1 + \Sigma_A(p; \Lambda)) \\ B(\vec{p}^2, \omega_p; \mu) &= Z_2^{f,vac}(\Lambda, \mu) \left(Z_m^{f,vac}(\Lambda, \mu) m_R^f(\mu) + \Sigma_B(p; \Lambda) \right) \\ C(\vec{p}^2, \omega_p; \mu) &= Z_2^{f,vac}(\Lambda, \mu) (1 + \Sigma_C(p; \Lambda)) \end{aligned} \quad (2.68)$$

Problems of the renormalization

Using this renormalization method, problems appear if too small values for the renormalized quark mass $m_R^f(\mu)$ are inserted, since a strong decrease in the mass renormalization constant $Z_m^{f,vac}(\mu, \Lambda)$ is the result. Physically the mass renormalization constant should not depend on the renormalized input mass, but as one can see in figure 2.2 there is a dependency on the input mass at small mass values.

Among other things, this behavior of the mass renormalization constant leads to negative values for the regularized quark condensate at higher temperatures, which is only corrected if one sets $Z_m^{heavy,vac}(\mu, \Lambda)$ to $Z_m^{light,vac}(\mu, \Lambda)$ (or the other way around, which is possibly the better choice). The question is now, where does this problem in our renormalization method comes from? The origin of this problem is that, for small renormalization points or small renormalized quark masses, dynamical effects (dynamical mass generation) become more important and falsify the

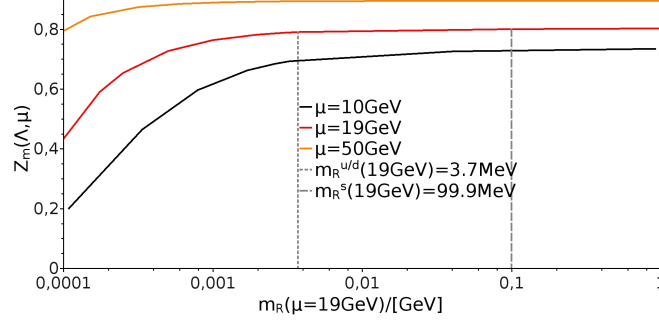


Figure 2.2: Mass dependency of the mass renormalization constant $Z_m^{f,vac}(\Lambda, \mu)$ for different renormalization points μ in vacuum. Noticeable is the renormalization point dependency of the decrease at small mass values. In fact for higher renormalization points, the decrease turns out to be lesser. In this plot a Maris-Tandy ansatz (4.6), with parameters from the related section 4.1 and the mass values and renormalization points shown in the figure, is employed. Furthermore the mass values for all renormalization points have to be translated to one renormalization point ($m_R(\mu') \rightarrow m_R(\mu)$).

results for too small values of the renormalized quark mass. A diagrammatic clarification for this can be seen in the following figure 2.3.

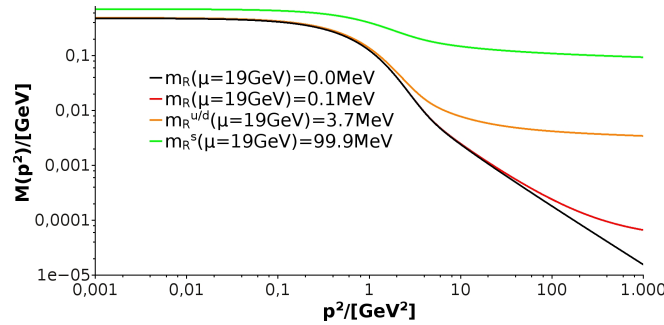


Figure 2.3: Dynamical mass for different mass values including the chiral limit. Noticeable is that the irregular asymptotic form (colored lines, at higher momenta) is strongly overshadowed by the regular asymptotic form (black line, at higher momenta), if the renormalization points μ or the renormalized quark mass values $m_R^f(\mu)$ are decreased. In this plot a Maris-Tandy ansatz given in equation (4.6) is employed. This is done in vacuum, with parameters from the section 4.1 and the mass and renormalization points given in the figure.

The regular

$$M^f(p^2) \propto \frac{2\pi^2\gamma_m}{3} \frac{-\langle \bar{\Psi}\Psi \rangle_{cl}^f}{p^2 \left(\frac{1}{2} \ln \left(\frac{p^2}{\Lambda_{QCD}^2} \right) \right)^{1-\gamma_m}} \quad (2.69)$$

and irregular

$$M^f(p^2) \propto M^f(\mu^2) \left[\omega \log \left(\frac{p^2}{\mu^2} \right) + 1 \right]^{-\gamma_m} \quad (2.70)$$

asymptotic form presented in the last figure 2.3 are the solutions to the ultraviolet limit of the quark DSE

$$M^f(p^2) = Z_m^{f,vac}(\mu, \Lambda) m_R^f(\mu) + \frac{1}{\pi} \frac{\alpha(p^2)}{p^2} \int_{p_0^2}^{p^2} dq^2 M^f(q^2) + \frac{1}{\pi} \int_{p^2}^{\Lambda^2} dq^2 \frac{\alpha(q^2)}{q^2} M^f(q^2) \quad (2.71)$$

where a Maris-Tandy ansatz and the Rainbow-ladder approximation are employed for the chiral limit as well as for non-vanishing bare quark masses. In the regular asymptotic form, $\langle \bar{\Psi} \Psi \rangle_{cl}^f$ describes the renormalization point independent quark condensate in chiral limit (chiral condensate), $\gamma_m = \frac{12}{11N_c - 2N_f}$ is the anomalous dimension of the quark mass function and Λ_{QCD} is a scaling variable. For more information see reference [24]. The interpretation of figure 2.3 is that we cannot use renormalized quark masses values and renormalization points, where the dynamical mass generation is not negligible any more. To avoid problems and errors one should use the mass renormalization constant at high renormalization points or high renormalized quark masses. This means we should use $Z_m^{light,vac}(\mu, \Lambda) = Z_m^{heavy,vac}(\mu, \Lambda)$.

2.2 Bound-states

The fundamental degrees of freedom of the QCD, discussed in the last section, are the foundation of more complex structures, but due to their own color and the color confinement, they do not exist as free particles. Only color neutral hadrons, as bound-states of quarks and gluons, appear as observable particles. We can describe many properties of these strongly interacting hadrons by the constituent quark model, proposed by Gell-Mann and Zweig. Due to this model, we have a classification scheme for the composite states of QCD according to their flavor content. By considering the Noether currents $j_\alpha^\mu(x)$ and their related charges $Q_\alpha(t) = \int d^3x j_\alpha^0(x)$, corresponding to the global flavor transformations $U_V(1) \times SU_V(N_f) \times SU_A(N_f) \times U_A(1)$, we get the flavor (isospin, hypercharge/strangeness) and baryon number as well as the charge of the state as conserved quantum numbers. With these quantum numbers, the fact that observable hadrons are color singlet states and information to further symmetries of QCD, like the spin and parity transformation properties, we are able to divide the hadrons into classes of bound-state particles (mesons, baryons, glueballs, tetraquarks,...) and spin states ($J^{PC} = 0^{-+}, 1^{--}, \dots$). For more information to this model see references [21] and [25]. The problem with this quark model, however, is the missing connection to the QCD. In the more elaborated theory of QCD, non-perturbative phenomena like color confinement and dynamical chiral symmetry breaking are taken into account, to describe correctly the hadron spectrum. In quantum field theory, bound-states appear as poles in Green-functions and therefore in the scattering amplitudes and the cross sections, too. To describe an n-particle bound-state, one has to investigate the 2n-point Green-function

$$G_{\alpha_1 \dots \alpha_{2n}}(x_1 \dots x_{2n}) = \langle 0 | \hat{T} \{ \Psi_{\alpha_1}(x_1) \bar{\Psi}_{\alpha_2}(x_2) \dots \Psi_{\alpha_{2n-1}}(x_{2n-1}) \bar{\Psi}_{\alpha_{2n}}(x_{2n}) \} | 0 \rangle, \quad (2.72)$$

and its properties at the poles, where the total momentum squared of the Green-function equates a bound-state mass. This can be seen, considering the Källén-Lehmann spectral representation for the propagator and the completeness relation of QCD:

$$\mathbb{1} = \sum_{\lambda} \frac{1}{(2\pi)^3} \int d^4p \theta(p^0) \delta(p^2 - m_{\lambda}^2) |\lambda\rangle \langle\lambda| = \sum_{\lambda} \frac{1}{(2\pi)^3} \int \frac{d^3p}{2E_p} |\lambda\rangle \langle\lambda| \quad (2.73)$$

In this equation the Lorentz-invariant weight implements the condition, that every hadron is on its mass shell ($p^2 = m_{\lambda}^2 \Leftrightarrow E_p^2 = \vec{p}^2 + m_{\lambda}^2$). The state space of the QCD, which is defined by the complete set of orthogonal eigenstates $|\lambda\rangle$ of the self-adjoint Hamiltonian, contains colorless bound-states but also (unphysical) colored states are possible. While the unphysical colored states have to be neglected, the colorless bound-states carry momenta as well as further Quantum numbers, that reflect symmetries of the QCD (angular momentum, parity, flavor). Inserting the completeness relation above into the two field operators, which appear in the time ordered vacuum expectation value of the propagator (2-Green-function), yields a single particle pole at $p^2 = m_{\lambda}^2$. The typical multi-particle continuum of the Källén-Lehmann spectral representation, with branch cuts above $p^2 = 4m_{\lambda}^2$, does not exist, since these states would carry color. The absence of this continuum consequently is a further sign for the color confinement.

As bound-states, we can consider quark-antiquark bound-states (mesons), three quark bound-states (baryons) or multiple other particle types, but in the following we restrict ourselves to the quark-antiquark bound-states. For this purpose, we have to consider four-point Green-functions. Until now, we study mesons with arbitrary spin and flavor. But there exist invariant subspaces of mesons, which each have a certain flavor content and fixed spin quantum numbers (J^{PC}). If we want to take only one of these meson types into account, we have to project, from the enormous state-space mentioned earlier, to states which coincide with the fixed spin quantum numbers (J^{PC}) and flavor content of this meson. This is done by setting $x_1 = x_2 = x$ and $x_3 = x_4 = y$ and contracting the resulting quark pairs in the four-point Green-function with Dirac and flavor matrices $r_a \Gamma_{\beta\alpha} \Gamma'_{\delta\gamma} r_b$. As result we can express the Green-function by current correlator's of the form $\langle 0 | \hat{T} \{ W_{\alpha}(x) W'_{\beta}(y) \} | 0 \rangle$. The quantity $W_{\alpha}^{(\prime)}(x)$, however, describes the vector $V_{(e)}^{\mu}(x)$, axialvector $A_{(e)}^{\mu}(x)$, scalar $S_{(e)}(x)$ or pseudoscalar $P_{(e)}(x)$ Noether current ($j_e^{\Gamma}(x) := \bar{\Psi}(x) \Gamma r_e \Psi(x)$ or $j^{\Gamma}(x) := \bar{\Psi}(x) \Gamma \Psi(x)$) with the corresponding Dirac-matrices $\Gamma \in \{\gamma^{\mu}, \gamma^{\mu} \gamma_5, \mathbb{1}, i\gamma_5\}$. For $W = W'$, the resulting Green-function can be seen as effective meson propagators of the form $\langle 0 | \hat{T} \{ W_{\alpha}(x) W_{\beta}(y) \} | 0 \rangle = \sum_{\lambda} D_F(z, m_{\lambda}) \omega_{\alpha\beta}$, since it represents a two-point-function of the composite fields $S_e(x), P_e(x), V_e^{\mu}(x), A_e^{\mu}(x)$ with the fixed quantum number (J^{PC}). In this equation, $D_F(z, m_{\lambda}) = \int \frac{d^4p}{(2\pi)^4} e^{-ipz} \frac{i\Lambda(p)}{p^2 - m_{\lambda}^2 + i\epsilon}$ with $z = x - y$ defines the Feynman propagator of a particle with mass m_{λ} and some other quantum numbers. To prove the validity of this representation, we have to consider the transition element between the vacuum and a hadron with total momentum P and relative momentum p between the two constituents:

$$\chi_{\alpha\beta}^l(x_1, x_2, P, p) := \langle 0 | T \Psi_{\alpha}(x_1) \bar{\Psi}_{\beta}(x_2) | \lambda_l(P, p) \rangle \quad (2.74)$$

This hadron bound-state (or Bethe-Salpeter) wave-function can be seen as the transition probability of a quark-antiquark-system $|\Psi\bar{\Psi}\rangle$ to become an on-shell ($P^2 = m_\lambda^2$) meson bound-state $|\lambda_l(P, p)\rangle$ with fixed momenta P and p and other quantum numbers l . By considering the translation invariance, we see that the bound-state wave-function mainly depends on the relative coordinate $z = x_1 - x_2$ and from the total position $x = \frac{x_1+x_2}{2}$ only through a phase:

$$\chi_{\alpha\beta}^l(x_1, x_2, P, p) = \langle 0 | T \Psi_\alpha(-\frac{z}{2}) \bar{\Psi}_\beta(\frac{z}{2}) | \lambda_l(P, p) \rangle e^{-iPx} = \chi_{\alpha\beta}^l(z, P, p) e^{-iPx} \quad (2.75)$$

We can prove this dependency, inserting $x_1 = x + \frac{z}{2}$ and $x_2 = x - \frac{z}{2}$ as well as the behavior of field operators and one-particle states under Poincaré-transformation $U(\Lambda, a)$:

$$U(\Lambda, a) \Psi_\alpha(x) U^{-1}(\Lambda, a) = \Lambda \Psi_\alpha(\Lambda x + a), \quad U(\Lambda, a) | \lambda_l(P) \rangle = e^{iPa} | \lambda_l(\Lambda P) \rangle \quad (2.76)$$

Additionally, the vacuum is invariant under Poincaré transformation $U(\Lambda, a) | 0 \rangle = | 0 \rangle$. By inserting the completeness relation (2.73) into the Green-function and using the definition of the time ordering operator $\langle 0 | \hat{T} \{ W_\alpha(x) W'_\beta(y) \} | 0 \rangle = \Theta(z^0) \langle 0 | W_\alpha(x) W'_\beta(y) | 0 \rangle + \Theta(-z^0) \langle 0 | W'_\beta(y) W_\alpha(x) | 0 \rangle$ as well as the behavior (2.75), we get the alternative representation of the Feynman propagator $D_F(z, m_\lambda) = \int \frac{d^3p}{2E_p} \frac{\Theta(z^0) e^{-ipz} + \Theta(-z^0) e^{ipz}}{(2\pi)^3} \Lambda(p)$ and therefore the first indication that hadrons produce poles in their propagators. The next step is to find a functional Dyson-Schwinger description, originating from the generating functional.

2.2.1 Bethe-Salpeter-equations

In this section we want to derive bound-state equations for quark-antiquark composite particles. In the Dyson-Schwinger approach, these bound-state equations for quark-antiquark systems are called Bethe-Salpeter equations (BSE). Since we are calculating composite particles, we need the Green-function's of the constituents as input. Analog to the elementary particles, we can derive the BSE's from the generating functional. But for this purpose, we have to use the two-particle irreducibility (2PI) instead of one-particle irreducibility. In a diagrammatic description, one particle irreducibility (1PI) means that the corresponding diagrams are constructed such that cutting one internal line does not disconnect them. Analogously, cutting two internal lines does not disconnect two particle irreducible diagrams. For a further discussion and examples of two particle irreducibility consider references [26] and [27]. The following derivation of the BSE's using two particle irreducibility, will be oriented along the lines of reference [28].

In case of the elementary particles, we introduced a source term $J_\alpha(x)$ at the space-time point x . The related quantum numbers were summed in the multi-index α . These sources were inserted into the generating functional, to generate all Green-functions by functional derivatives of the generating functional with respect to the respective source (to remember see (2.2)). In case of quark-antiquark bound-states, we have to introduce bilocal sources $J_{\alpha\beta}(x, y)$, which depend on two spacetime points x and y and are able to connect to two fields. This is indicated by the two multi-indices α and β . Consequently, we can write the generating functional of the QCD in

Euclidean space as follows

$$Z[J] = \mathcal{N} \int \mathcal{D}\varphi \exp \left[-S_{QCD}[\varphi] + \int_x \varphi_\alpha(x) J_\alpha(x) + \int_x \int_y \varphi_\alpha(x) J_{\alpha\beta}(x, y) \varphi_\beta(y) \right] \quad (2.77)$$

For simplicity we will set $J_\alpha(x) = 0$ in the following. In analogy to equation (2.9), we can define the connected and irreducible bound-state Green-functions based on the bound-state generating functional for connected (two-particle) Green-functions $W_{[2]}[J]$ and the two-particle irreducible (2PI) effective action $\Gamma_{[2]}[B]$:

$$\begin{aligned} W_{[2]}[J] &= -\log(Z[J]) \\ \Gamma_{[2]}[B] &= W_{[2]}[J] + \int d^4x d^4y B_{\alpha\beta}(x, y) J_{\beta\alpha}(y, x) \end{aligned} \quad (2.78)$$

where $B_{\beta\alpha}(x, y)$ denotes a bilocal field, which corresponds to the source $J_{\alpha\beta}(y, x)$. We see that $J_{\alpha\beta}(y, x) = \frac{\delta\Gamma_{[2]}[B]}{\delta B_{\beta\alpha}(x, y)}$ and $B_{\alpha\beta}(x, y) = \frac{\delta W_{[2]}[J]}{\delta J_{\beta\alpha}(y, x)}$ are again conjugated sources and we can calculate all (2PI) Green-functions as functional derivatives of the (2PI) effective action. In this case, however, the derivatives of $W_{[2]}[J]$ do not produce connected Green-functions, but bi-locally connected ones. The related bi-locally connected two point Green-function $\left(G_{[2]}^{(2)}\right)_{\vec{\alpha}\vec{\beta}} = \left. \frac{\delta^2 W_{[2]}}{\delta J_{\alpha_1\alpha_2} \delta J_{\beta_1\beta_2}} \right|_{J=0}$ represents the propagator of a particle pair and is, in analogy to the (1PI) case, the inverse of the (2PI) Green-function for vanishing sources fields $J = 0$:

$$\left(\Gamma_{[2]}^{(2)}[B]\right)^{-1} \xrightarrow{B \rightarrow S} \left(G_{[2]}^{(2)}\right)_{\vec{\alpha}\vec{\beta}} \xleftarrow{0 \leftarrow J} W_{[2]}^{(2)}[J] \quad (2.79)$$

Here we indicated the second derivative of the respective generating function by the upper index (2) . In the equation we furthermore stated that the bilocal field $B_{\beta\alpha}$ corresponds to the exact quark Propagator $S_{\beta\alpha}$, if the source field $J_{\alpha\beta}$ vanishes:

$$B_{\beta\alpha}(x, y) \xrightarrow{J_{\alpha\beta}(y, x)=0} S_{\beta\alpha}(x, y) \quad (2.80)$$

To be able to obtain bound-state equations, we have to separate the "interacting" and the "non-interacting" parts of the (2PI) effective action. If we consider references [26] and [29], the (2PI) effective action can be written as

$$\Gamma_{[2]}[B] = \text{tr} [S_0^{-1} B] - \text{tr} [\log[B]] + \tilde{\Gamma}[B] \quad (2.81)$$

where $\tilde{\Gamma}[B]$ represents the interacting part. The trace given in this equation is in a functional sense as well as in the Dirac-, flavor- and color-space. This means, that we sum over the Dirac, flavor and color part and integrate over the continuous momentum space. This functional notation and the omission of the discrete indices will be used throughout the rest of the bound-state derivation. Using this representation for the (2PI) effective action, we get the following

expression for the inverse two-particle propagator

$$\left(G_{[2]}^{(2)}\right)^{-1} = \frac{\delta^2\Gamma_{[2]}[B]}{\delta B\delta B}\Bigg|_{B=S} = S^{-1}S^{-1} + \frac{\delta^2\tilde{\Gamma}_{[2]}[S]}{\delta S\delta S} \quad (2.82)$$

Reshuffling the terms and introducing the kernel

$$K := -\frac{\delta^2\tilde{\Gamma}_{[2]}[S]}{\delta S\delta S} \quad (2.83)$$

yields the bound-state equation

$$G_{[2]}^{(2)} = SS + SSKG_{[2]}^{(2)} \quad (2.84)$$

which is known as the inhomogeneous Bethe-Salpeter equation (BSE) for the quark-antiquark system. In strict sense this equation is only valid if the quark and antiquark have the same flavor, but an extension to the general case is possible. To be able to establish this equation for the bound-states, we have to clarify a missing piece: the definition of the kernel or the interacting part of the (2PI) effective action in terms of the quark propagator S . It transpires, that there exists a connection between the quark self-energy Σ and the quark-antiquark interaction kernel K of the bound-state equation. This connection can be seen in two possible ways: at first by considering the axialvector-Ward-Takahashi identity (AVWTI) (taken from reference [30])

$$\{\gamma^5\Sigma(-p_-) + \Sigma(p_+)\gamma^5\}_{\alpha\beta} = -\int_q K_{\alpha\gamma,\delta\beta}(p, q, P) \{\gamma^5 S(-p_-) + S(p_+)\gamma^5\}_{\gamma\delta} \quad (2.85)$$

which is the central identity that ensures the correct implementation of chiral symmetry and its dynamical breaking in the bound-state approach. The second possibility can be explained, if we consider the first derivative of the (2PI) effective action:

$$0 = J|_{B=S} = \frac{\delta\Gamma_{[2]}[B]}{\delta B}\Bigg|_{B=S} = \left(S_0^{-1} - B^{-1} + \frac{\delta\tilde{\Gamma}_{[2]}[B]}{\delta B}\right)\Bigg|_{B=S} \Leftrightarrow S^{-1} = S_0^{-1} + \underbrace{\frac{\delta\tilde{\Gamma}_{[2]}[S]}{\delta S}}_{=\Sigma} \quad (2.86)$$

We see that the self-energy Σ and the quark-antiquark interaction kernel K are the first and second functional derivatives of the interacting part of the (2PI) effective action $\tilde{\Gamma}[S]$ with respect to the quark propagator S . This opens the possibility to find a consistent and numerically feasible truncation of both equations. The interacting part of the (2PI) effective action is chosen to be in accordance with symmetries of the QCD. Consequently, the solutions of the DSE and the BSE inherit these symmetries, which is especially of importance for the applications of QCD to light hadrons, where chiral symmetry is essential.

Rainbow-ladder truncation

The simplest setup, that preserves the AVWTI independent from the interaction and therefore ensures that the pion, as Goldstone boson, is massless in chiral limit, is the Rainbow-ladder truncation. The diagrammatic representation of the (2PI) effective action $\tilde{\Gamma}$ related to this truncation is given in figure 2.4.

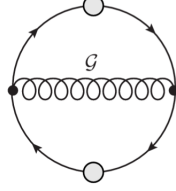


Figure 2.4: (2PI) effective action corresponding to a Rainbow ladder truncation with effective interaction \mathcal{G} . The second quark-gluon-vertex is represented as bare vertex, since it only contains the vector part γ^μ .

The corresponding quark-antiquark kernel is expressed by a gluon ladder exchange, including a gluon propagator a bare and a "dressed" quark-gluon-vertex. To preserve the AVWTI, the dressed vertex should consist out of Dirac basis elements with an odd number of gamma matrices only. Additionally the structures should only depend on the gluon momentum k . This leaves the vector part γ^μ with a purely k^2 -dependent vertex, the only choice for the DSE and the BSE. With this information we can write down the quark-antiquark kernel in Rainbow-ladder truncation as

$$K_{\alpha\gamma,\delta\beta}(p, q, P) = Z_2^2 \frac{4\pi\alpha(k^2)}{k^2} (t^a)_{AC} (t^a)_{BD} (i\gamma^\mu)_{\alpha'\gamma'} P_{\mu\nu}^{\mathcal{F}}(k) (i\gamma^\nu)_{\beta'\delta'} \delta_{ac}\delta_{db} \quad (2.87)$$

with the color basis elements t_a and the Dirac-matrices γ^μ defined in the Appendix A as well as the transversal Projector $P_{\mu\nu}^{\mathcal{F}}(k)$ defined in equation (2.28). Furthermore $\alpha(k^2)$ describes the strong coupling, resulting from the gluon and Vertex dressing functions and Z_2 is the quark wave-function renormalization constant. The diagonal flavor part is represented by the last two Kronecker delta's and the gluon momentum by $k = q - p$ with the quark momenta p and q .

Homogeneous BSE

The inhomogeneous BSE (2.84) for the two-particle propagator $G_{[2]}^{(2)}$ has poles at the energies, where the system exhibits a bound-state. Consequently we can express the propagator $G_{[2]}^{(2)}$ in terms of pole contributions and a regular term $R(p, q, P)$:

$$G_{[2]}^{(2)}(p, q, P) = \sum_i \frac{\chi(p, P_i)\bar{\chi}(q, -P_i)}{P^2 - P_i^2} + R(p, q, P) \quad (2.88)$$

The related on-shell condition is given by $P_i^2 = -M_i^2$, where i labels the bound-states. Except from the regular part, we can get a similar equation by inserting the QCD completeness relation (2.73) into a four-point Green-function, which we express by the bound-state wave-function

shown in equation (2.74). In case of mesons, we can also write this bound-state wave-function as

$$\chi(p, P_i) = S_{\alpha\beta}(p_+) \Gamma_{\beta\gamma}(p, P_i) S_{\gamma\delta}(-p_-) \quad (2.89)$$

with dressed (anti-) quark propagators $S_{\alpha\beta}(p)$ and the Bethe-Salpeter amplitude (BSA) $\Gamma_{\beta\gamma}(p, P_i)$. The charge conjugated bound-state wave-function $\bar{\chi}(p, P)$, appearing in the pole contribution, is related to the normal bound-state wave-function $\chi(p, P)$ by

$$\bar{\chi}(p, P_i) = [C\chi(-p, P_i)C^{-1}]^T \quad (2.90)$$

where $C = \gamma_2\gamma_4$ is the charge-conjugation matrix and the superscript T denotes a matrix transpose. Inserting the last three equation in the inhomogeneous BSE (2.84) and equating the residues at the bound-states poles $P^2 = P_j^2$, yields the following homogeneous Bethe-Salpeter equation (BSE) for the on-shell Bethe-Salpeter amplitude (BSA) $\Gamma_{\alpha\beta}(p, P)$, which is only valid at the pole $P_j^2 = -M_j^2$:

$$\Gamma_{\alpha\beta}(p, P) = \int_q K_{\alpha\gamma,\delta\beta}(p, q, P) \{S(q_+)\Gamma_{\alpha\beta}(q, P)S(-q_-)\}_{\gamma\delta} \quad (2.91)$$

Here the greek indices represent a super-index, which includes indices for the flavor, color and Dirac part. Furthermore we can express this homogeneous BSE graphically by figure 2.5, using the Rainbow-ladder truncation for the kernel (2.87):

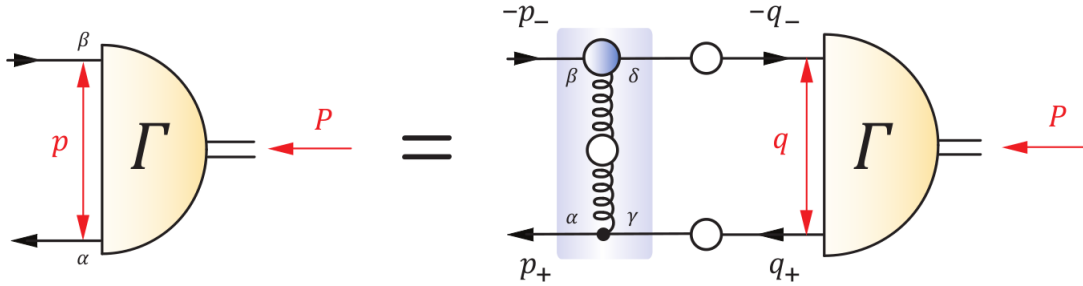


Figure 2.5: Graphical notation of the homogeneous Bethe-Salpeter equation in Rainbow-ladder truncation. The figure is taken from reference [30].

If we further apply the functional notation, suppressing the indices and the integral and integrating the quark and antiquark propagators into a new kernel \tilde{K} , we can write the BSE as eigenvalue equation:

$$\lambda(P^2)\Gamma(P^2) = \tilde{K}(P^2)\Gamma(P^2) \quad (2.92)$$

We have to introduce an eigenvalue $\lambda(P^2)$, since the homogeneous BSE is only valid for the on-shell condition $P^2 = -M_j^2$. Consequently we search for the total momentum $P^2 = -M_j^2$, which produce an eigenvalue of $\lambda(P^2) = 1$. This is done by calculating the homogeneous BSE for

multiple total momenta and plotting the eigenvalue spectrum $\lambda(P^2)$ against the squared total momentum P^2 . In this section the uppercase Latin letters (P, P_i) represent the total momentum of the quark-antiquark system, while the lowercase Latin letters (p, q, k) demonstrate relative momenta between the quark and antiquark. An index i stands for an on-shell momentum. Finally the lowercase Latin letters with subscript \pm ($\pm p_{\pm}, \pm q_{\pm}$) show the momenta of the quarks and antiquarks themselves. Thereby the momenta of the quarks and antiquarks are given by $\pm q_{\pm} = q \pm \eta_{\pm} P$ with the partitioning parameters η_{\pm} , which fulfill the condition $\eta_+ + \eta_- = 1$. For equal quark and antiquark masses, $\eta_{\pm} = \frac{1}{2}$ maximizes the calculable meson mass and simplifies the bound-state Amplitude. Furthermore the (anti-) quark momenta q_{\pm} are complex for time-like total momenta $P^2 < 0$. Therefore we need the (anti-) quark propagator for complex momenta.

Inhomogeneous BSE

While the on-shell quark-antiquark meson vertex is represented by the homogeneous BSE, we can get off-shell information by the inhomogeneous BSE. To omit the task of solving the full inhomogeneous BSE to get the desired information, we define a general vertex, that connects quarks and antiquarks to a color singlet current. The resulting quantity inherits the pole structure of $G_{[2]}^{(2)}$ (2.88) and is restricted to one mesonic channel. A BSE for this vertex can be derived by multiplying the inhomogeneous BSE (2.84) with a renormalized current Γ_0 and defining the inhomogeneous Bethe-Salpeter amplitude

$$\tilde{\Gamma} = S^{-1} S^{-1} G_{[2]}^{(2)} \Gamma_0 \quad (2.93)$$

This procedure then yields the inhomogeneous Bethe-Salpeter equation (BSE) for the off-shell Bethe-Salpeter amplitude (BSA) $\tilde{\Gamma}$

$$\tilde{\Gamma} = \Gamma_0 + K S S \tilde{\Gamma} \quad (2.94)$$

in functional notation and

$$\tilde{\Gamma}_{\alpha\beta}(p, P) = \Gamma_{\alpha\beta}^0(p, P) + \int_q K_{\alpha\gamma, \delta\beta}(p, q, P) \left\{ S(q_+) \tilde{\Gamma}_{\alpha\beta}(q, P) S(-q_-) \right\}_{\gamma\delta} \quad (2.95)$$

in full glory.

2.2.2 Normalization

Due to the structure of the equation, the homogeneous BSE (2.91) determines the BSA only up to a constant factor. Consequently an additional normalization condition is necessary. For this purpose we use a canonical norm, which follows from the (2PI) propagator by demanding that the residue at the bound-state pole equals one. This condition is necessary for the decomposition (2.88) to hold. In the neighborhood of a certain pole, we can approximate the two-particle

propagator $G_{[2]}^{(2)}$ by one pole term with arbitrary residue r_i

$$G_{[2]}^{(2)} \approx r_i \frac{\chi(p, P_i) \bar{\chi}(q, -P_i)}{P^2 - P_i^2} = \frac{r_i}{P_\mu + (P_i)_\mu} \frac{\chi(p, P_i) \bar{\chi}(q, -P_i)}{P_\mu - (P_i)_\mu} \quad (2.96)$$

and a simple pole in the variable P_μ . If a function $f(z) = \frac{g(z)}{h(z)}$ has a simple pole in z , the residue of $f(z)$ at the pole z_0 is given by $Res(f, z_0) = \frac{g(z_0)}{h'(z_0)}$. As result we can extract an equation for the residue by applying this property onto (2.96) and $G_{[2]}^{(2)} = (S^{-1}S^{-1} - K)^{-1}$. This yields

$$\left[\frac{\partial}{\partial P_\mu} \left(S_{\alpha\gamma}^{-1}(q_+) S_{\delta\beta}^{-1}(-q_-) \delta(p - q) - K_{\alpha\gamma, \delta\beta}(p, q, P) \right) \right]_{P=P_i}^{-1} = \frac{r_i}{2(P_i)_\mu} \chi(p, P_i) \bar{\chi}(q, -P_i) \quad (2.97)$$

By reshuffling the terms, taking the Dirac, flavor and color trace as well as the functional trace and expressing the bound-state wave-function in terms of the BSA and the (anti-) quark propagator, we get the normalization condition:

$$\begin{aligned} \mathcal{N}^2 = \frac{1}{r_i} = & - \frac{(P_i)_\mu}{2P_i^2} \frac{\partial}{\partial P_\mu} tr_{DCF} \left[\int_q S(q_+) \bar{\Gamma}(q, -P_i) S(-q_-) \Gamma(q, P_i) + \right. \\ & \left. + \int_q \int_p S(q_+) \bar{\Gamma}(q, -P_i) S(-q_-) K(p, q, P) S(p_+) \Gamma(p, P_i) S(-p_-) \right]_{P=P_i} \end{aligned} \quad (2.98)$$

With this normalization constant we can define a normalized BSA $\Gamma_{\alpha\beta} = \frac{\Gamma_{\alpha\beta}^N}{\mathcal{N}}$. It is further noteworthy that the lowercase Latin letters with subscript \pm and superscript i represent the momenta of the quark propagator itself for the on-shell condition $P^2 = P_i^2$. The notation with index i additionally is supposed to illustrate, that the derivative in the first term acts only on the quark propagators and in the second term only on the kernel. If we use the Rainbow-ladder truncation, mentioned earlier, the kernel K becomes independent from the total momentum ($K(p, q, P) \rightarrow K(p, q)$) and the second term vanishes. Another renormalization, where we use the spectral representation of the BSE to derive the normalization constant \mathcal{N} , is possible too. The corresponding derivation of the norm can be found in reference [28] and the norm itself is given by

$$\mathcal{N}^2 = -\lambda'_i(P_i^2) \quad (2.99)$$

2.2.3 Meson amplitudes

The quark-antiquark bound-state amplitude $\Gamma_{\alpha\beta}(p, P)$ is the solution of the homogeneous BSE (2.91) and depends on the relative momentum p and the total momentum P , which corresponds to the mass of the meson bound-state $P^2 = -M^2$. Furthermore there are different possible representations of the quark-antiquark bound-state, corresponding to the continuous and discrete transformation properties of the Lorentz group. This means there are different representations, belonging to the considered spin and parity state (J^{PC}). In the following, we only will consider two possible meson states: The pseudoscalar (0^{-+}) and the vector meson (1^{--}). For this purpose

we consider the BSA as vertex between a two-particle bound-state, a quark and an antiquark. While a general fermion-scalar vertex, which depends on the momenta p and P , has four basis elements

$$\tau_k^S(P, p) \in \{\mathbb{1}, \not{P}, \not{p}, [\not{P}, \not{p}]\}, \quad (2.100)$$

a fermion-vector vertex includes 12 structures

$$\tau_k^{V,\mu}(P, p) \in \{\gamma^\mu, p^\mu, P^\mu\} \times \{\mathbb{1}, \not{P}, \not{p}, [\not{P}, \not{p}]\}. \quad (2.101)$$

Due to the negative parity requirement for the parity transformation of the pseudoscalar and vector meson amplitudes

$$\begin{aligned} \Gamma_P(p, P) &= -\gamma^4 \Gamma_P(\Lambda p, \Lambda P) \gamma^4, & \Gamma_V^\mu(p, P) &= \gamma^4 \Lambda_\nu^\mu \Gamma_V^\nu(\Lambda p, \Lambda P) \gamma^4 \\ \text{with} & & \Lambda &= \text{diag}(-1, -1, -1, 1) \end{aligned} \quad (2.102)$$

we have to include a γ^5 -matrix into the scalar basis elements, to define the following four structures for the pseudoscalar vertex.

$$\tau_k^P(P, p) \in \{\gamma^5, \gamma^5 \not{P}, \gamma^5 \not{p}, \gamma^5 [\not{P}, \not{p}]\} \quad (2.103)$$

Using these Dirac basis elements, the BSA of the pseudoscalar $\left[\Gamma_{P,\lambda}^e(P, p)\right]_{\alpha\beta}$ and vector meson $\left[\Gamma_{V,\lambda}^{\mu e}(P, p)\right]_{\alpha\beta}$ can be decomposed into Lorentz-covariant parts $\tau_k^{(\mu)}(P, p)$ and Lorentz invariant parts $f_k(P, p)$ as well as a flavor part r^e and a color part:

$$\begin{aligned} \left[\Gamma_{P,\lambda}^e(P, p)\right]_{\alpha\beta} &= \sum_k^4 f_k^P(P, p) \left\{i\tau_k^P(P, p)\right\}_{\alpha'\beta'} \otimes \delta_{AB} \otimes r_{ab}^e \\ \left[\Gamma_{V,\lambda}^{\mu e}(P, p)\right]_{\alpha\beta} &= \sum_k^{12} f_k^V(P, p) \left\{i\tau_k^{V,\mu}(P, p)\right\}_{\alpha'\beta'} \otimes \delta_{AB} \otimes r_{ab}^e \end{aligned} \quad (2.104)$$

In this decomposition of the BSA, the Lorentz invariant parts $f_k^P(P, p)$ and $f_k^V(P, p)$ are called the dressing functions of the particular meson and they include the important momentum dependence. The transformation properties under the Lorentz-group are determined by the Dirac-structures, this means by the Lorentz covariants parts $\tau_k^{(\mu)}(P, p)$. While the color part is diagonal, the flavor part is represented by the flavor basis elements given in Appendix A.2. The greek super-indices on the lhs therefore sum the indices for the Dirac (α', β'), flavor (a, b) and color (A, B) part. Finally, the index λ represents the particle type.

Chebyshev expansion

We mentioned, that the meson amplitude depends on the relative p and total P momentum of the bound-state. This dependency can be formulated in terms of the three Lorentz invariants:

P^2 , p^2 and $\hat{P} \cdot \hat{p} = \frac{P \cdot p}{|P||p|} = \cos(\theta_p) = z_p$. It transpires that the (BSE) calculation is simplified, if the dependence on the angular variable z_p is expanded in Chebyshev polynomials. For the calculation and the final results we will therefore expand the dressing functions $f_k(P^2, p^2, z_p)$ in Chebyshev polynomials of first kind $T_n(z_p) = \cos(n\theta_p) = \cos(n \arccos(z_p))$ with $z_p \in [-1, 1]$:

$$f_k(P^2, p^2, z_p) \approx \sum'_{j=0}^{\tilde{N}} f_k^j(P^2, p^2) T_j(z_p) (i)^j \quad (2.105)$$

where \sum' indicates, that the first term has to be halved. This problem can be circumvented, by defining modified Chebyshev polynomials $\tilde{T}_j(z_p) = \left(\frac{1}{\sqrt{2}} \delta_{j,0} + (1 - \delta_{j,0}) \right) T_0(z_p)$ and corresponding Chebyshev coefficients $\tilde{f}_k^j(P^2, p^2) = \left(\frac{1}{\sqrt{2}} \delta_{j,0} + (1 - \delta_{j,0}) \right) f_k^j(P^2, p^2)$ or if we take Chebyshev polynomials of second kind. Furthermore we can mention, that the (modified) Chebyshev polynomials fulfill the discrete orthogonality relation

$$\frac{2}{N} \sum_{n=0}^{N-1} \tilde{T}_i(z_n^p) \tilde{T}_j(z_n^p) = \delta_{ij} \quad (2.106)$$

where $z_n^p = \cos\left(\frac{2n+1}{2N}\pi\right)$ defines the N zeros of the N^{th} Chebyshev polynomial T_N . If we consequently apply $\frac{2}{N} \sum_{n=0}^{N-1} \tilde{T}_j(z_n^p) (i)^{-j}$ onto the k^{th} meson dressing function $f_k(P^2, p^2, z_p)$, we can extract the j^{th} Chebyshev coefficient of this dressing function $f_k^j(P^2, p^2)$. To conclude this discussion, we can mention that the Chebyshev polynomials are numerically calculated by the recursive formula $T_j(z_p) = 2z_p T_{j-1}(z_p) - T_{j-2}(z_p)$ and the first polynomials $T_0(z_p) = 1$ and $T_1(z_p) = z_p$.

Charge conjugation

The Charge conjugation C describes one of the three discrete Lorentz-transformations, besides parity P and time-reversal T . Thereby, the charge conjugation exchanges particles with their corresponding antiparticles and creates a physical system, where everything would be the same, except that the quantum numbers (electromagnetic charge, flavor number, baryon number), mentioned at the beginning of this section, would be reversed. For constituents of equal flavor the homogeneous Bethe-Salpeter amplitude is an eigenstate of the operation of charge conjugation, yielding the C-parity eigenvalue C to be an additional multiplicative quantum number $C = \pm 1$ - additional to the spin J and the parity P . We can define the charge-conjugated BSA of the pseudoscalar and vector meson by

$$\bar{\Gamma}_P(P, p) = [C \Gamma_P(P, -p) C^{-1}]^T \quad \bar{\Gamma}_V^\mu(P, p) = - [C \Gamma_V^\mu(P, -p) C^{-1}]^T \quad (2.107)$$

where $C = \gamma_2 \gamma_4$ describes the charge-conjugation matrix and T indicates a matrix transpose. In the following, we will consider only general eigenstates of the C-Parity

$$\bar{\Gamma}(P, p) = \eta_c \Gamma(P, p) \quad \text{with the eigenvalues} \quad \eta_c = \pm 1 \quad (2.108)$$

If we consider the decomposition (2.104), the Lorentz covariants transform according to $\bar{\tau}_k(P, p) = [C\tau_k(P, -p)C^{-1}]^T = \xi_k\tau_k(P, p)$ and the C-parity manifest itself in the symmetry of the meson dressing functions with respect to z_p :

$$\begin{aligned} \bar{f}_k(P^2, p^2, z_p) &= f_k(P^2, p^2, -z_p) \approx \sum_{j=0}^{\tilde{N}} \tilde{f}_k^j(P^2, p^2) \tilde{T}_j(-z_p) (i)^j \\ &= \sum_{j=0}^{\tilde{N}/2} \tilde{f}_k^{2j}(P^2, p^2) \tilde{T}_{2j}(z_p) (-1)^j - i \sum_{j=0}^{\tilde{N}/2-1} \tilde{f}_k^{2j+1}(P^2, p^2) \tilde{T}_{2j+1}(z_p) (-1)^j \\ &\stackrel{!}{=} \tilde{\xi}_k f_k(P^2, p^2, z_p) \quad \text{for eigenstates} \end{aligned} \quad (2.109)$$

The C-parity eigenvalue is therefore given by $\eta_c = \xi_k \tilde{\xi}_k$ and defines a C-parity eigenstate only if it is constant for all k . Consequently we have for each meson dressing function either even or odd Chebyshev polynomials, if we consider eigenstates of the C-parity. In particular for the pseudoscalar meson ($J^{PC} = 0^{+-}$), build by two constituents with equal flavor, this yields that the odd Chebyshev coefficients vanish.

In the following we only will consider pseudoscalar mesons with two light quarks. To calculate these so-called pions we use the decomposition (2.104) as well as the Chebyshev expansion (2.105) to derive BSE's for the Chebyshev coefficients of the individual dressing functions. This rather technical task is done in Appendix B.2 including the final bound-state equations used for the results.

2.2.4 Pion decay constant

Next we reconsider the inhomogeneous Bethe-Salpeter equation (2.95) for the special case of the isovector axialvector vertex

$$\left[\tilde{\Gamma}_A^{\mu,e}(p, P) \right]_{\alpha\beta} = \left[\tilde{\Gamma}_{A,0}^{\mu,e} \right]_{\alpha\beta} + \int_q K_{\alpha\gamma,\delta\beta}(p, q, P) \left\{ S(q_+) \tilde{\Gamma}_A^{\mu,e}(q, P) S(-q_-) \right\}_{\gamma\delta} \quad (2.110)$$

with the bare vertex $\tilde{\Gamma}_{A,0}^{\mu,e} = Z_A \gamma_5 \gamma^\mu \otimes \frac{r^e}{2} \otimes \mathbb{1}_c$ and the dressed one given by

$$\tilde{\Gamma}_A^{\mu,e}(p, P) = \sum_k^{N_A} f_{R,k}^A(P, p) i\tau_k^{A,\mu}(P, p) \otimes \frac{r^e}{2} \otimes \mathbb{1}_c + \hat{\Gamma}_A^{\mu,e}(p, P) + \frac{P^\mu f_\lambda}{P^2 + m_\lambda^2} \Gamma_{P,\lambda}^e(P, p) \quad (2.111)$$

In this representation of the vertex, we follow the lines of [31] and separate the regular terms $f_{R,k}^A(P, p)$ and $\hat{\Gamma}_A^{\mu,e}(p, P)$ from the pole-structure with the on-shell condition $P^2 = -m_\lambda^2$. $\Gamma_{P,\lambda}^e(P, p)$ is therefore the pseudoscalar homogeneous Bethe-Salpeter amplitude (2.104) of the pseudoscalar meson bound-state with the mass m_λ . By separating the pole-structure also in the BSE kernel, we can rewrite the inhomogeneous BSE for the isovector axialvector vertex by

$$\frac{1}{Z_A} \left[\tilde{\Gamma}_A^{\mu,e}(p, P) \right]_{\alpha\beta} = \frac{1}{Z_A} \left[\tilde{\Gamma}_{A,0}^{\mu,e} \right]_{\alpha\beta} + \int_q M_{\alpha\gamma,\delta\beta}(p, q, P) \left\{ S(q_+) \tilde{\Gamma}_{A,0}^{\mu,e}(q, P) S(-q_-) \right\}_{\gamma\delta} \quad (2.112)$$

where M is the renormalised, fully-amputated quark-antiquark scattering amplitude: $M = K + K(SS)K + \dots$, which can be decomposed as

$$M_{\alpha\gamma,\delta\beta}(p, q, P) = \left[\tilde{\Gamma}_{P,\lambda}^l(-P, q) \right]_{\gamma\delta} \frac{1}{P^2 + m_\lambda^2} \left[\Gamma_{P,\lambda}^l(P, p) \right]_{\alpha\beta} + R_{\alpha\gamma,\delta\beta}(p, q, P) \quad (2.113)$$

where R is regular for $P^2 \rightarrow -m_\lambda^2$. We have a unit residue in this equation due to the canonical normalization presented in section 2.2.2. By substituting M and the isovector axialvector vertex (2.111) into (2.112) and equating the residue at the bound-state pole, we obtain

$$\delta_{el} f_\lambda P^\mu = Z_2 \int_q tr_{DCF} \left[\Gamma_{A,0}^{\mu,e} S(q_+) \Gamma_{P,\lambda}^l(q, P) S(-q_-) \right] \quad (2.114)$$

where we were free to chose $Z_2(\mu, \Lambda) = Z_A(\mu, \Lambda)$, since their ratio is a finite, renormalization-group-invariant quantity. In the derivation, f_λ appeared as the residue of the isovector axialvector vertex $\left[\tilde{\Gamma}_A^{\mu e} \right]_{\alpha\beta}(x, x_1, x_2) = \langle 0 | T A_e^\mu(x) \Psi_\alpha(x_1) \bar{\Psi}_\beta(x_2) | 0 \rangle$, but it further is connected to the transition from a pseudoscalar meson to an axialvector current. This can be seen, if we reconsider equation (2.75) and add some Dirac-flavor structure Γr^e . As result we can extract gauge-invariant quantities from the bound-state wave-function by setting $z = x_1 - x_2 = 0$:

$$\begin{aligned} \langle 0 | j_e^\Gamma(x) | \lambda_l(P, p) \rangle &= \langle 0 | j_e^\Gamma(0) | \lambda_l(P, p) \rangle e^{-iPx} = -\Gamma_{\beta\alpha} r^e \chi_{\alpha\beta}^l(x, x, P, p) \\ &= - \int_p tr_{DCF} \left[\Gamma r^e \chi^l(p, P) \right] e^{-iPx} \end{aligned} \quad (2.115)$$

This represents the vacuum-to-hadron transition element of the corresponding current. If we use the Dirac structure $\Gamma = \gamma^\mu \gamma_5$, which produces axialvector currents, $|\lambda_l(P, p)\rangle$ is restricted to pseudoscalar and axialvector mesons. In the following, however, we only will consider pseudoscalar mesons. For this case we get

$$\langle 0 | A_e^\mu(x) | \lambda_l(P, p) \rangle = \delta_{el} i P^\mu f_\lambda e^{-iPx} \quad (2.116)$$

where the total momentum is fixed to $P^2 = m_\lambda^2$. Since the pion ($\lambda = \pi$) decays weakly into leptons ($\pi^\pm \rightarrow W^\pm \rightarrow \mu^\pm + \nu_\mu/\bar{\nu}_\mu$), f_π defines the pion's electroweak decay constant. Further on, if we consider the medium, this means the finite temperature or cold dense matter case, the pion decay constant f_π split up into two quantities: one spatial f_π^s and one temporal f_π^t decay constant. The corresponding defining equation for the pion decay constants is then given by

$$\delta_{el} \left(f_\pi^t P_{\mu\nu}^{\mathcal{L}}(v) + f_\pi^s P_{\mu\nu}^{\mathcal{J}}(v) \right) P^\nu = Z_2 \int_q tr_{DCF} \left[\tilde{\Gamma}_{A,0}^{\mu,e} S(q_+) \Gamma_{P,\pi}^l(q, P) S(-q_-) \right] \quad (2.117)$$

with the four momentum projectors $P_{\mu\nu}^{\mathcal{L}/\mathcal{J}}(v)$ given by (2.28) and the unity vector v defined by $v = (\vec{0}, 1)$. Consequently the decay constants f_π^t and f_π^s are longitudinal and transversal to the fourth momentum component (heat bath in case of finite temperature). Following the lines of reference [14], we additionally can define a velocity of the pion by the ratio of the two decay

constants:

$$u^2 = \left(\frac{f_\pi^s}{f_\pi^t} \right)^2 \quad (2.118)$$

Only in vacuum ($T = 0$ and $\mu_q = 0$) the two decay constant are equal $f_\pi^t = f_\pi^s = f_\pi$, yielding the pion velocity to be $u = 1$. Furthermore we can find a pion dispersion relation in the symmetry broken phase. Its real part is given by

$$\omega^2 = u^2 (\vec{p}^2 + m_\pi^2) \quad (2.119)$$

At $\vec{p} = 0$, the energy of the pion $E_\pi = um_\pi$ is called the pion pole mass. Finally we can state the in-medium pion propagator. This propagator results from the vacuum pion propagator in momentum and Euclidean space $D_\pi(p) = \frac{1}{p^2 + m_\pi^2}$, mentioned at the beginning of this section, by inserting the dispersion relation:

$$D_\pi(p) = \frac{1}{p_4^2 + u^2 (\vec{p}^2 + m_\pi^2)} \quad (2.120)$$

where p_4 equals a bosonic Matsubara frequency ω_p in case of finite temperature.

2.2.5 Gell-Mann-Oakes-Renner-relation

If we use $\Gamma = i\gamma_5$ instead of $\Gamma = \gamma^\mu\gamma_5$ in equation (2.115), we produce pseudoscalar currents and get the following transition from a pseudoscalar meson to a pseudoscalar current

$$\langle 0 | P_e(x) | \lambda_l(P, p) \rangle = \delta_{el} r_\lambda e^{-iPx} \quad (2.121)$$

In the beginning of this section, we discussed the conserved quantum numbers of the vectorial groups of the global flavor transformations $U_V(1) \otimes SU_V(N_f) \otimes SU_A(N_f) \otimes U_A(1)$. The discussion of the axial groups $U_A(1)$ and $SU_A(N_f)$, although, was skipped. Both groups are only conserved, if the masses of all flavors vanish in the mass matrix. Additionally the groups are broken by two phenomena: anomalous symmetry breaking and the spontaneous mass generation, connected to the spontaneous chiral symmetry breaking. Although the symmetries are explicitly and dynamically broken, there still exist a Noether current. In case of the $SU_A(N_f)$ -symmetry-group the conservation of the Noether current $A_e^\mu = \bar{\Psi} \gamma^\mu \gamma_5 r_e \Psi$, is explicitly hampered by a mass term, which one can see, considering

$$\partial_\mu A_e^\mu = i \bar{\Psi} \{M, r_e\} \gamma_5 \Psi \stackrel{M=m_q \mathbf{1}}{=} 2m_q \bar{\Psi} i \gamma_5 r_e \Psi = 2m_q P_e \quad (2.122)$$

This relation represents the partially conserved axialvector current (PCAC) relation and connects the divergence of the axialvector current with a pseudoscalar density. If we include this relation, for equal quark masses, into a vacuum-to-hadron transition element and consider the

momentum space, we find the relation

$$f_\lambda m_\lambda^2 = 2m_q r_\lambda \quad (2.123)$$

which is valid for all flavor non-singlet pseudoscalar mesons. In this case the quantity r_λ is not directly measurable, but can be connected to other useful quantities. As derived in reference [31], we are able to derive an inhomogeneous BSE (2.112) for an isovector, pseudoscalar vertex, analogue to the discussion of the previous paragraph. The corresponding bare and dressed vertex are therefore given by $\tilde{\Gamma}_{P,0}^e = Z_P \gamma_5 \otimes \frac{r^e}{2} \otimes \mathbb{1}_c$ and

$$\tilde{\Gamma}_P^e(p, P) = \sum_{k=0}^4 f_{R,k}^P(P, p) i\tau_k^P(P, p) \otimes \frac{r^e}{2} \otimes \mathbb{1}_c + \frac{r_\lambda}{P^2 + m_\lambda^2} \Gamma_{P,\lambda}^e(P, p) \quad (2.124)$$

where the terms $f_{R,k}^P(P, p)$ are again regular for $P^2 \rightarrow -m_\lambda^2$ and the isovector, pseudoscalar vertex also receives a contribution from the bound-state pole at the meson mass m_λ . Since the ratio $\frac{Z_4}{Z_P}$ is a renormalisation-group-invariant quantity, we are again free to chose $Z_4(\mu, \Lambda) = Z_2(\mu, \Lambda)Z_m(\mu, \Lambda) = Z_P(\mu, \Lambda)$. The result of equating the residue at the bound-state pole on both sides of the inhomogeneous BSE then yields

$$i\delta_{el}r_\lambda = Z_2 Z_m \int_q tr_{DCF} \left[\tilde{\Gamma}_{P,0}^e S(q_+) \Gamma_l^P(q, P) S(-q_-) \right] \quad (2.125)$$

If we further consider the steps of reference [31] the following relation for the pion can be deduced in chiral limit:

$$r_\pi = \frac{\langle \bar{\Psi} \Psi \rangle_\mu^0}{f_\pi} \quad (2.126)$$

where $\langle \bar{\Psi} \Psi \rangle_\mu^0$ represents the chiral condensate, which will be discussed later on. Inserting this relation into the equation (2.123), gives us the known Gell-Mann-Oakes-Renner (GMOR) relation

$$f_\pi^2 m_\pi^2 = 2m_q \langle \bar{\Psi} \Psi \rangle_\mu^0 \quad (2.127)$$

2.3 Observables

As mentioned earlier the first aim of this work is to study the QCD phase diagram. Until now we discussed the properties of the DSE and BSE components. Henceforth we will look for the background of the QCD phase diagram, beginning with the introduction of some basis elements related to the phase diagram.

2.3.1 Symmetries and order parameters

At first we have to define the meaning of a phase and its connection to thermodynamical observables. In thermodynamics a phase is defined as a possible state of a macroscopic system given by a localized homogeneous region, which has different thermodynamic properties than other phases. With thermodynamic properties, physical and chemical properties such as polarization, magnetization, deformation, structure of a Crystal and so on are meant. In this idealized definition effects like crystal defects or surface effects are neglected. Furthermore, the stability of these phases is connected with the (analytical) behavior of the thermodynamical potential or the corresponding partition function, which describes the system. This thermodynamic potential is continuous for all values of the external parameters, but not analytical. The analyticity therefore is defined by the continuity and the continuous differentiability of the corresponding function. If the thermodynamic potential is analytical for a set of external parameters, the corresponding phase is stable. But if one of the derivatives of the thermodynamic potential exhibits singularities or discontinuities for a certain set of external parameters, the thermodynamic potential is not analytical and we observe a phase transition and the coexistence of multiple phases. The order of the related phase transition between the coexisting phases therefore is given by the number of derivatives, which have to be applied on the thermodynamic potential until discontinuities or singularities appear in the resulting derivative. Since the difference between the coexisting phases become physically unimportant for increasing orders, we rather use a newer classification, which describes the first order phase transition as discontinuous phase transition and all higher phase transition as continuous phase transitions. The discontinuous phase transition therefore results from passing a metastable phase, while evolving from one phase to the other, by changing a certain external parameter. Such a metastable phase is for example the wet steam region in case of fluids, where the fluid and the gaseous phase coexist but locally separated. To be able to separate different phases, we need observables, which serve as indicator for the corresponding phase. For this purpose, the observables have to be related to properties of the system, which change when passing from one phase to another. At this point the Landau order parameters are brought in.

Landau theory

Phase transitions can always be described by an external parameter t , which becomes critical $t \rightarrow t_c$ at the point where the phase transition between the coexisting phases takes place. In this context, the Landau theory describes the behavior of observables and the partition function itself near this critical point. The theory, however, is only applicable on phases which properties are related to a certain symmetry. Furthermore, the phase transitions have to be marked by the loss of this symmetry, with the result that the transition of any physical system between two different states of symmetry (\equiv phase) is denoted as phase transition. The Landau order parameter, mentioned earlier, is a quantity related to the symmetry, which changes its value when passing from one phase to another. Usually the order parameter is finite in one phase

and vanishes in the other one. Consequently the order parameter serves as indicator of the phase transition. Since the order parameter further measures the realization of a phase (how strongly is a symmetry broken), we have quantitative values of the properties, too. For example these order parameters can be physical quantities like densities, magnetizations or the dynamical quark mass, where the last one is produced spontaneously only in one phase, if the chiral limit is considered. In an area close to the point where the phase transition takes place, the order parameter additionally can be described by a power law of the external parameter t , mentioned above. Note that this is only true if we consider continuous phase transitions (should not be mistaken with a crossover). Consequently we get the following general scaling law for order parameters

$$\begin{aligned} X &= b \cdot (-t)^\beta & \text{for } t < 0 \\ X &= 0 & \text{for } t > 0 \end{aligned} \tag{2.128}$$

with the critical exponent $\beta \in \mathbb{R}^+$ and the proportionality constant $b \in \mathbb{R}^+$. In this case the external parameter t represents the reduced temperature $t = \frac{T-T_c}{T_c}$, but other external parameters like the reduced chemical potential are possible too, if we consider another scaling law. Furthermore, we note that also other physical quantities behave according to a certain scaling law near the point of the phase transition. For example the response function R , which is defined as the second derivative of the thermodynamical potential, fulfills the general scaling law

$$\begin{aligned} R &= c \cdot (t)^{-\gamma} & \text{for } t > 0 \\ R &= c' \cdot (-t)^{-\gamma'} & \text{for } t < 0 \end{aligned} \tag{2.129}$$

with γ and γ' being two different critical exponents for the area above and below the point of the phase transition. Apart from this quantity, there are further scaling laws for the correlation-length, the correlation-function, the state variable and others. All these scaling laws have in common, that they are universal, which means, that the phase separation and the fact that there is critical behavior are identical for different systems, if the critical temperature T_c is used as normalization. As result the scaling law is valid for all respective quantities of all systems, dimensions, sizes and theories. The only things that change are the related critical exponents and proportionality factors as well as the values of the critical temperature T_c . Systems, which have the same critical exponents, are part of the same universality class. Furthermore, the positive defined critical exponents (β for the order parameter, γ for the response-function, δ for the state variable) as well as the scaling function are universal quantities. This entails that the critical exponents only depend on the dimension and the approximation method, but not on the coupling strength. Since the critical exponents are always positively defined, the sign in the exponent of the scaling law indicates if the observable trends towards zero or if it diverges. The further purpose of the Landau theory is to expand the thermodynamic potential A in powers of

the order parameter X near the critical point of the phase transition. This can be represented by

$$\begin{aligned} A(X, T) &\sim A_0(T) + A_2(T) \cdot X^2 + A_4(T) \cdot X^4 + \dots \\ A_n(T) &\sim A_{n,0} + A_{n,0} \cdot t + \dots \end{aligned} \quad (2.130)$$

where we used symmetry arguments to cancel the odd powers of the order parameter. Before we can use our knowledge about the temperature and chemical potential behavior of the order parameter to discuss the phase diagram, we have to mention that the first order phase transition has a discontinuity in the order parameter at the point where the phase transition takes place, in contrast to the continuous phase transition. Furthermore we have to mention two symmetries, which are important for the strong interaction.

Chiral symmetry

Chiral symmetry and its breaking is one of the most important non-perturbative phenomenon of the QCD. Thereby, the chirality is the property of left- and right-handed quarks to transform separately under the chiral symmetry group $SU_R(N_f) \times SU_L(N_f)$. Due to this transformation property the left- and right-handed quarks decouple from each other. While the right-handed quark transforms under the fundamental representation of the right-handed group $SU_R(N_f)$, the left-handed quark transforms as singlet and vice versa for the left-handed group $SU_L(N_f)$. If we consider the chiral limit, which is defined as the limit of vanishing quark masses, the chiral symmetry group results from the enlarged flavor symmetry group $SU_V(N_f) \times SU_A(N_f)$. In fact, any mass term breaks the $SU_A(N_f)$ -group and therefore the chiral-symmetry, no matter whether the mass term is dynamically generated or explicitly given in the QCD-action. To investigate this property, we will use the right-handed (Ψ_+) and left-handed (Ψ_-) quarks (also called Weyl-spinors), which are defined in equation (A.16). The Dirac-spinor thereby is a superposition of these two representations $\Psi = \begin{pmatrix} \Psi_+ \\ \Psi_- \end{pmatrix}$ and can be projected onto the Weyl-spinors utilizing the chiral projectors P_{\pm} defined in equation (A.15). With these projectors we are able to express the QCD-action by left- and right-handed quarks, to figure out which tensor-structures break the chiral symmetry. There are two possible cases how Dirac matrices transform under chiral symmetry:

$$\begin{aligned} \Gamma = \gamma^\mu, \gamma^\mu \gamma_5 &\rightarrow \begin{aligned} P_\omega \Gamma P_\omega &= 0 \\ \bar{\Psi}_{-\omega} \Gamma \Psi_\omega &= 0 \end{aligned} \rightarrow \bar{\Psi} \Gamma \Psi = \sum_\omega \bar{\Psi}_\omega \Gamma \Psi_\omega, \\ \Gamma = \mathbf{1}, \gamma_5, \sigma^{\mu\nu} &\rightarrow \begin{aligned} P_{-\omega} \Gamma P_\omega &= 0 \\ \bar{\Psi}_\omega \Gamma \Psi_\omega &= 0 \end{aligned} \rightarrow \bar{\Psi} \Gamma \Psi = \sum_\omega \bar{\Psi}_{-\omega} \Gamma \Psi_\omega \end{aligned} \quad (2.131)$$

The Dirac tensor-structure elements, shown in the first line, are chiral symmetric terms of the QCD-action, which we can see, if we consider the transformation $\Psi'_\omega = U_\omega \Psi_\omega$ with the trans-

formation matrix $U_\omega = e^{i\sum_a \epsilon_a^\omega \tau_a}$ in the following. In this transformation, τ_a represent the hermitian, traceless generators of the $SU_{R/L}(N_f)$ -groups and ϵ_a^\pm are the corresponding independent group parameters. Applying the mentioned transformation onto the tensor-structures, given in the first line of the last equation, yields

$$\sum_\omega \bar{\Psi}'_\omega \Gamma \Psi'_\omega = \sum_\omega \bar{\Psi}_\omega U_\omega^\dagger \Gamma U_\omega \Psi_\omega = \sum_\omega \bar{\Psi}_\omega \Gamma \Psi_\omega \quad (2.132)$$

The tensor-structures of the second line, however, break chiral symmetry, since $U_{-\omega}^\dagger U_\omega \neq \mathbf{1}$. As result we see, that an explicit mass term in the QCD-action breaks chiral symmetry. Another indication for this property is that the $2 \times (N_f^2 - 1)$ Noether currents $j_{a,\omega}^\mu = \bar{\Psi}_\omega \gamma^\mu \tau_a \Psi_\omega$ and their related charges $Q_{a,\omega} = \int d^3x \Psi_\omega^\dagger \tau_a \Psi_\omega$ are only conserved, if the mass matrix, defined in the Appendix A.1.2, vanish:

$$\partial_\mu j_{a,\omega}^\mu = i (\bar{\Psi}_{-\omega} M \tau_a \Psi_\omega - \bar{\Psi}_\omega \tau_a M \Psi_{-\omega}) \quad (2.133)$$

The best way to observe the implications of an introduction of a mass term is to consider the charge, which corresponds to the $U_A(1)$ Noether current without the anomalous contribution $j^\mu = \bar{\Psi} \gamma^\mu \gamma_5 \Psi$. This charge is given by

$$Q^A(t) = \int d^3x \bar{\Psi} \gamma_0 \gamma_5 \Psi = \int d^3x \Psi^\dagger \gamma_5 \Psi \quad (2.134)$$

If we further insert $\gamma_5 = P_+ - P_-$ into the charge, we can split the contribution of the right- and left-handed quarks:

$$Q^A(t) = \int d^3x (\Psi_+^\dagger \Psi_+ - \Psi_-^\dagger \Psi_-) = \int d^3x (n_+ - n_-) = N_+ - N_- \quad (2.135)$$

Since the charge is no longer a constant of motion, if we insert a mass term, the ratio between left- and right-handed quarks $\frac{N_+}{N_-}$ can vary with time. As result, the introduction of a mass is connected to a possible transfer between right- and left-handed quarks and therefore to the breaking of chiral symmetry. To understand this property physically, we consider the helicity $h = \frac{\vec{s} \cdot \vec{p}}{|\vec{s}| |\vec{p}|}$, which describes the projection of the spin \vec{s} onto the direction of motion \vec{p} . If the spin points in the same direction as the momentum the particle is called left-handed and for the case that it points in the opposite direction, it is called right-handed. For massive particles, it is always possible to find an inertial system by Lorentz-boost, which is faster than the particle, since a massive particle cannot move at the speed of light. The result is that the direction of motion and therefore the sign of the helicity switches. Consequently the helicity is only a conserved quantum-number for massless particles.

Until now we discussed the chiral symmetry breaking by an explicit mass term. But one of the key features of QCD is the spontaneous chiral symmetry breaking (S χ SB), which is connected to the purely non-perturbative phenomenon of dynamical quark mass generation. Against the expectation, the dominant contribution to the physical quark mass does not result from the

Higgs-mechanism, but from $S\chi SB$ and the $U_A(1)$ -anomaly instead. This is true in chiral limit as well as for physical quark masses. While the explicit breaking of chiral symmetry, which is due to the current quark mass term (generated from Higgs-mechanism), is independent from external parameters like temperature and chemical potential, the dynamical mass generation and therefore the $S\chi SB$ strongly depends on these parameters. As result, it is possible that the dynamical part of the chiral symmetry is restored under certain conditions of the external parameters.

In the following, we want to find an order parameter for the chiral symmetry. Since the explicit chiral symmetry breaking is always present independent from the external parameters, we only observe an actual phase transition between the chiral broken and the chiral symmetric phase in case of the chiral limit. If, however, we consider the physical case with non-vanishing current quark masses, we are only able to study the dynamical part of the chiral symmetry breaking. In this case, we will denote the phase where the dynamical part of the chiral symmetry breaking almost vanishes and mainly the explicit one remains, as chiral symmetric phase.

Connected to the experience that a mass term breaks chiral symmetry, the obvious first choice for an order parameter is the dynamical quark mass $M_f(p) = \frac{B_f(p)}{A_f(p)}$. Another common possibility is the quark condensate $\langle \bar{\Psi}\Psi \rangle_\mu^f$, which is the derivative of the generating functional w.r.t. the current quark mass. The quark condensate is a possible choice, since it describes the transition probability for left-handed quarks to become right-handed ones and vice versa. This property can be seen by inserting the chiral representation (see A.1.2) of the Dirac-Matrices in the quark condensate $\langle \bar{\Psi}\Psi \rangle_\mu^f = \langle \Psi_L^\dagger \Psi_R \rangle_\mu^f + \langle \Psi_R^\dagger \Psi_L \rangle_\mu^f$. The connection to chiral symmetry is automatically given if we compare with (2.135). Only if the transition probability is zero the ratio between the right-handed and left-handed quarks is constant. To calculate the quark condensate, we use the expression

$$\langle \bar{\Psi}\Psi \rangle_\mu^f = -Z_m^{f,vac}(\Lambda, \mu) Z_2^{f,vac}(\Lambda, \mu) \sum_q^f tr_{DC} [S^f(p, \mu)] \quad (2.136)$$

resulting from (2.15) and yielding

$$\langle \bar{\Psi}\Psi \rangle_\mu^f = -\frac{Z_m^f Z_2^f N_c}{\pi^2} \begin{cases} \frac{1}{2} \int_{R,q}^\Lambda \frac{B_f(q^2)}{q^2 A_f^2(q^2) + B_f^2(q^2)} & \text{in vacuum,} \\ 2 \int_{R,q}^\Lambda \frac{B_f(\vec{q}^2, \omega_q)}{\vec{q}^2 A_f^2(\vec{q}^2, \omega_q) + \tilde{\omega}_q^2 C_f^2(\vec{q}^2, \omega_q) + B_f^2(\vec{q}^2, \omega_q)} & \text{for finite temperature,} \\ \frac{1}{\pi} \int_{R,q}^\Lambda \int_{-1}^1 dz \frac{\sqrt{1-z^2} B_f(q^2, z)}{\vec{q}^2 A_f^2(q^2, z) + \tilde{\omega}_q^2 C_f^2(q^2, z) + B_f^2(q^2, z)} & \text{for cold dense matter,} \end{cases} \quad (2.137)$$

if we insert the already known quark propagator. In the upper equations Z_2 and Z_m are the quark wave-function and the quark mass renormalization constants. The trace tr_{DC} includes the Dirac and the color trace and the shortcuts for the integrals are defined in Appendix C.1. N_c is the number of color flavors and $z = \cos(\theta)$ represents the angle between the four internal momentum q and the fourth component of the same. The index μ further implies, that the

quark condensate depends on the quark renormalization point. At a certain point, however, we need to remove this dependency by multiplying the quark condensate by a factor, which defines the renormalization point invariant quark condensate

$$\langle \bar{\Psi}\Psi \rangle^f = \left(\frac{1}{2} \log \left(\frac{\mu^2}{\Lambda_{QCD}^2} \right) \right)^{\gamma_m} \cdot \langle \bar{\Psi}\Psi \rangle_{\mu}^f \quad (2.138)$$

While the chiral condensate, which is defined as the quark condensate in chiral limit, vanishes above a certain critical external parameter value, the quark condensate converges to a fixed value in case of physical quark masses. This value is proportional to the bare quark mass and shows a quadratically divergent behavior. Furthermore the asymptotic value represents the static contribution of the quark condensate, resulting from the current quark mass in the quark propagator. If we use the fact that the dynamical contribution of the quark propagator becomes negligible for high quark masses, we can regularize the quark condensate by subtracting the primarily static quark condensate of a heavy quark, weighted with the corresponding mass ratio:

$$\Delta_{f'f}^{(\mu)} = \langle \bar{\Psi}\Psi \rangle_{(\mu)}^{f'} - \frac{Z_m^{f'} m_R^{f'}(\mu)}{Z_m^f m_R^f(\mu)} \langle \bar{\Psi}\Psi \rangle_{(\mu)}^f \quad (2.139)$$

In this regularized quark condensate no divergences appear anymore. Note that we do not sum over the index f . Additionally the high quark does not necessarily have to be back coupled to the system. The observation that the quark condensate in the physical quark mass case trends towards zero but never vanishes, is attributed to the fact, that the explicit mass term breaks chiral symmetry independent from the thermodynamic circumstances. As result the quark condensate does not indicate a proper phase transition for non-vanishing quark masses. Although, this order parameter will be used throughout this work, we can mention another order parameter: The chiral susceptibility, which is given by $\chi_f(p) = \frac{\partial \langle \bar{\Psi}\Psi \rangle_{\mu}^f}{\partial m_R^f(\mu)}$.

Confinement

The confinement is a not fully understood non-perturbative phenomenon of QCD, which can be described with two related points of view. On one hand the confinement is connected to the complete absence of (free) colored particles from particle state space, while it is, on the other hand, connected to the fact that it is impossible to separate individual quarks completely. The first statement is known as color confinement and the latter one is called the quark confinement. To discuss the quark confinement, we have to introduce the potential between two quarks, which is given by $V(r) = \frac{\alpha}{r} + \sigma r$, where σ defines the string tension in the linear rising component. The direct implication of this linear rising potential is, that an infinite amount of energy is necessary to separate two quarks completely. But for a rising distance between the two quarks the stored potential energy increases, due to the separation of the quarks. At a certain point it becomes eventually large enough to create a quark-antiquark-pair. Due to this case of string

breaking, the potential mentioned above has to be varied in the sense that it becomes constant at a certain distance between the two quarks. The quarks consequently can be separated up to a given distance, but it is impossible to separate them completely. Since the resulting quark-antiquark pairs of the string breaking are color neutral, the color confinement is always fulfilled. Connected to the scenario with linear rising potential, we can define the Polyakov-loop, which is obtained by taking the color trace of the Wilson loop in direction of the imaginary time τ :

$$L[A] := \frac{1}{N_c} \text{tr}_C \left(\mathcal{P} e^{i \int dr A_4(\vec{x}, \tau)} \right) \quad (2.140)$$

In this equation, \mathcal{P} defines the path-ordering operator. If we further take the expectation value of the Polyakov loop $\langle L[A] \rangle$, we find that the resulting quantity is connected to the free energy of a static quark F_q :

$$\langle L[A] \rangle \propto e^{-\frac{F_q}{T}} = \begin{cases} 0 & \text{if } F_q = \infty \\ \text{finite} & \text{if } F_q < \infty \end{cases} \quad (2.141)$$

This mirrors the implications of the linear rising potential. As result, we have found an order parameter for the confinement-deconfinement phase transition. It only remains to define how the expectation value of the Polyakov-loop is calculated. In fact a DSE for the background field $\langle A_0 \rangle$ is derived and calculated, which yields upon integration the potential of the background field. The DSE for this background field was introduced in [32] and is diagrammatically given by 2.6. Utilizing this background field we can define an upper bound for the expectation value

$$\frac{\delta(\Gamma - S)}{\delta A_0} = \frac{1}{2} \left[\text{diagram 1} - \text{diagram 2} - \text{diagram 3} - \frac{1}{6} \text{diagram 4} + \text{diagram 5} \right]$$

Figure 2.6: DSE for the background field $\langle A_0 \rangle$. The curly propagators at the bottom of each diagram represent the background field. It couples to a gluon-, a ghost- and a quark-loop as well as to a pair of two-loop diagrams involving gluon and ghost propagators.

of the Polyakov-loop:

$$L[\langle A_0 \rangle] \geq \langle L[A_0] \rangle, \quad L[\langle A_0 \rangle] = 0 \Leftrightarrow \langle L[A_0] \rangle = 0 \quad (2.142)$$

The confinement phase diagram was studied in previous works [10], but will not be discussed in this work. In future works, however, it is possible to study the confinement in case of the cold dense matter case.

2.3.2 QCD phase diagram

Until now we discussed the basis elements of a phase diagram and mentioned, that all information to the thermodynamic properties of a given system are summed in its phase diagram. An

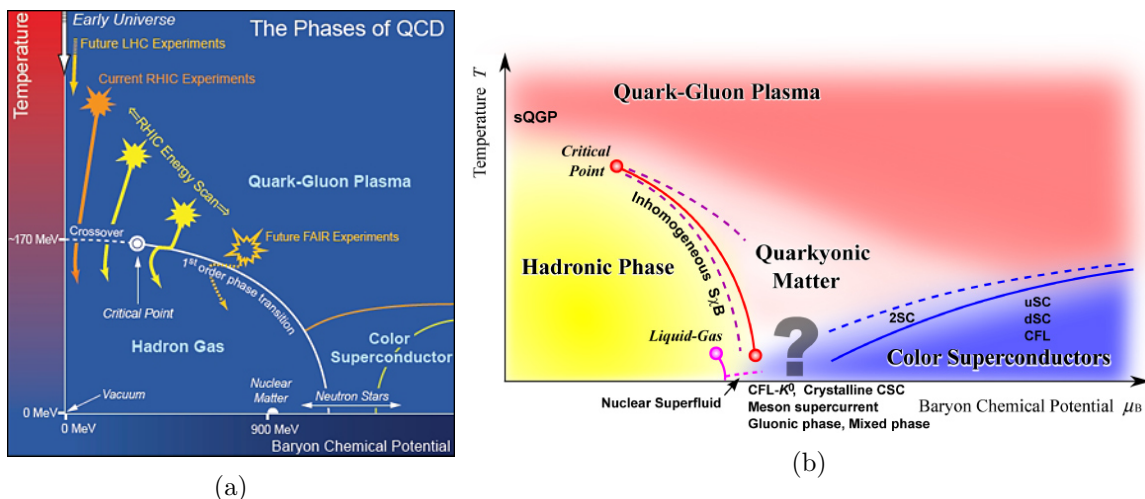


Figure 2.7: Sketches for the QCD phase diagram with special attention to different areas.

arbitrary phase diagram therefore is determined by an equation of state $f(T, \mu_q)$. Depending on the behavior of this state-equation and the related properties of the system at a given set of external parameters (T, μ_q) , certain areas are defined as phases. Different phases are separated by lines, which can be parameterized by the critical external parameters $(T_c(\mu_q), \mu_q)$. Thereby these so-called coexistence lines/ areas/ hyperareas indicate a phase transition between multiple coexisting phases. Furthermore, we distinguish between different kinds of phase transitions by presenting different kinds of lines in the phase diagram. Additionally there is a critical end point, which represents the point, where the kind of phase transition of the coexistence line changes. The state-equation usually depends on many external parameters but can be projected onto pairs of two of these parameters.

The QCD phase diagram contains information of the two symmetries, which we discussed in the paragraph before. The corresponding state-equations are the order parameters of the respective symmetry. They depend on the external parameters of temperature T and quark μ_q or baryon μ_B chemical potential. According to these symmetries and the related properties, we distinguish phases corresponding to different kinds of strongly interacting matter. Two possible sketches of the QCD phase diagram are shown in figure 2.7.

The phases, in these QCD phase diagrams, are shown for the external parameters of temperature on the vertical axes and the baryon chemical potential on the horizontal axes. As one can see, there is a rich structure and various effects. We can distinguish between three main areas: the quark-gluon-Plasma (QGP), the color-superconductors and the hadronic phase. The latter phase, at small temperatures and chemical potentials (correspond to small densities), is therefore defined by a realized color confinement and a spontaneously broken chiral symmetry, due to the formation of a quark condensate. The physical degrees of freedom in this phase are the only free particles for the related conditions: the strongly interacting hadrons. The most popular hadrons are the protons and the neutrons, which form nuclei and atoms and therefore all higher structures that appear in nature. Figure 2.7a shows the corresponding position of such nuclear matter. It further defines the vacuum as the point of zero temperature and chemical potential

or density. In the second phase - the quark-gluon-plasma at high temperatures and chemical potentials - the quarks and gluons are the degrees of freedom, since there is no longer a color confinement in this phase. Additionally, the chiral symmetry is (approximately) restored in this phase. At the hot and dense conditions of the QGP-phase the quarks can consequently move as free particles. Finally it remains only to mention the last phase: the superconducting phase(s) at high chemical potential (high densities) and low temperatures. These superconducting phase(s) exist in great variety, due to different kinds of quark flavors, and are assumed to be present in neutron stars. An important phenomenon at very high densities (chemical potentials) of the strange quark matter is the appearance of a so-called color-flavor-locking (CFL) phase, in which quarks form Cooper pairs only in certain combinations of color and flavor. The CFL phase is the most symmetric realization of a color-superconducting phase, where all three quark flavors symmetrically participate in forming Cooper pairs. In this phase left-handed quarks are paired with each other, as well as right-handed ones. The chiral symmetry is broken, but not due to the formation of a quark condensate, but rather by the pairing of the left- and right-handed quarks. Furthermore the differences due to the quark masses can be neglected, which distinguish the CFL phase from the non-CFL phases. The most important non-CFL phase is the 2SC phase, where two light flavors form Cooper pairs, while the strange quark remains unpaired as residual color-charge. A study to the different superconducting phases can be found in reference [33].

While the existence of the phases are largely accepted, the coexistence lines are still a matter of intense studies in experimental and theoretical groups, as one can see in figure 2.7a, where different experiments are mentioned. The following statements can summarize the present status. The hadronic phase and the QGP are separated by different transition regions. For vanishing chemical potential as well as for small chemical potentials we find a crossover, which indicates a continuous change between the phases. For increasing chemical potential this crossover ends up in a second order critical end point (CEP), which separates the crossover region from the sharp (first order) phase transitions, expected for higher chemical potentials. Previous works [2] showed a gap between the crossover of the confinement and the crossover of the chiral symmetry, but the chiral and the confinement-deconfinement coexistence lines have the same CEP. Additionally, no differences in the area of the sharp phase transitions were found. Furthermore we observed in previous works, as well as in this work, an additional phase in the area of the sharp phase transition. Our investigations to the QCD phase diagram showed that the crossover turns at the critical end point into an area defined by the upper and lower spinodal. The upper and lower spinodal are therefore two possible solutions for the first order phase transition. We already mentioned, that a discontinuous phase transition results from passing a metastable phase, while evolving from the symmetric to the non-symmetric phase. The mentioned area between the two spinodal is such a metastable phase, where both phases the QGP and the hadronic phase coexist but locally separated.

We have to mention that the crossover as continuous transition between the two phases is not an actual phase transition and does not have a properly defined critical temperature. Therefore, we define a pseudo-critical temperature to resolve this issue. There are two possible ways to define

such a pseudo-critical temperature, which work for the discontinuous phase transition too. First of all we can use the inflection point method, where we utilize the point of maximal change in the curve of the order parameter w.r.t. the temperature. This yields for the chiral symmetry, with the quark condensate as order parameter:

$$\left| \frac{\partial \langle \bar{\Psi} \Psi \rangle_\mu^f}{\partial T} \right|_{T=T_c^{infl.}} = \max_{\forall T} \left| \frac{\partial \langle \bar{\Psi} \Psi \rangle_\mu^f}{\partial T} \right| \quad (2.143)$$

Secondly, we can define the pseudo critical temperature by the maximum of the response function of the respective symmetry. In case of the chiral symmetry the response function is given by the chiral susceptibility. Consequently the pseudo critical temperature is defined by

$$\left| \frac{\partial \langle \bar{\Psi} \Psi \rangle_\mu^f}{\partial m_R^f(\mu)} \right|_{T=T_c^{infl.}} = \max_{\forall T} \left| \frac{\partial \langle \bar{\Psi} \Psi \rangle_\mu^f}{\partial m_R^f(\mu)} \right| \quad (2.144)$$

The latter definition measures the reaction of the system to small changes in the quark mass. Both methods give different results in the crossover region but coincide in the discontinuous phase transition region and the CEP.

2.3.3 Silverblaze property

The Silverblaze property is a property of the cold dense matter case. It states that, in a relativistic theory at zero temperature, the partition function and observables do not depend on the chemical potential, if the latter stays below the mass gap of the system. If the chemical potential exceeds the mass gap, states can be excited and observables change. The mass gap depends on the observed particles. In case of baryons the mass gap is equal to $\frac{m_B}{3}$, with m_B being the baryon mass of the lightest baryon. The Silverblaze region is therefore below $\mu < \frac{m_B}{3}$. If we consider mesons, the mass gap is given by $\frac{m_M}{2}$, with m_M being the meson mass of the lightest meson. Although the Lagrangian of the theory shows an explicit chemical potential dependence, observables like the masses of physical particles must stay constant, which requires a cancellation of the internal chemical potential dependencies of the Lagrangian. The Silverblaze property only holds at zero temperature, since thermal excitations also change observables. Additionally we have to be attentive in choosing the truncation, since the latter one can easily violate the Silverblaze property. In the following, we will follow the traces of reference [33] to discuss the Silverblaze property.

For simplicity, we now assume a quark propagator (2.44) with the physical mass Δ , which has a pole on the imaginary p_4 -axis and fulfills

$$D(\vec{p}^2 = 0, p_4 = i\Delta) = -\Delta^2 C^2(\vec{p}^2 = 0, p_4 = i\Delta) + B^2(\vec{p}^2 = 0, p_4 = i\Delta) = 0 \quad (2.145)$$

Simultaneously, Δ should be the lowest singularity of the system, which means the mass gap of the system. If we consider the figure 2.8 and the residue theorem, we can use the substitution

$q_4 \rightarrow q_4 + i\mu_q$ as long as the singularity at $\Im(q_4) = \Delta$ is not included in the closed path γ , this means as long as the chemical potential μ_q is smaller as the pole Δ .

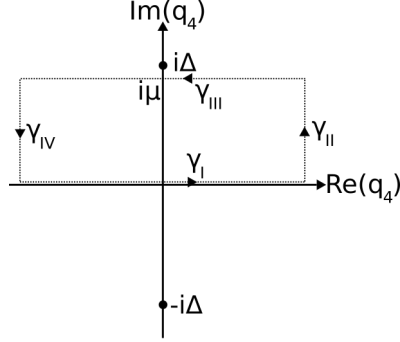


Figure 2.8: Change in the integration contour for finite chemical potential μ_q below the mass gap Δ , using the residue theorem. The dots represent the poles of the propagator in the complex q_4 plane.

If we apply the substitution mentioned above to the quark self-energy Σ , the quark-loop Π and the quark condensate $\langle \bar{\Psi}\Psi \rangle$ for chemical potentials below the mass gap $\mu_q < \Delta$, we get the following connections to the vacuum analogues:

$$\begin{aligned}
 \Sigma(\vec{p}, p_4 + i\mu_q) &\sim \int_q S(\vec{q}, q_4 + i\mu_q) K(\vec{p}, p_4 + i\mu_q, \vec{q}, q_4 + i\mu_q) \\
 &\stackrel{q_4 \rightarrow q_4 + i\mu_q}{\equiv} \int_q S(\vec{q}, q_4) K(\vec{p}, p_4 + i\mu_q, \vec{q}, q_4) \sim \Sigma_{vac}(\vec{p}, p_4 + i\mu_q) \\
 \Pi(\vec{k}, k_4) &\sim \int_q S(\vec{q}, q_4 + i\mu_q) S(\vec{p}, p_4 + i\mu_q) \tilde{K}(\vec{p}, p_4 + i\mu_q, \vec{q}, q_4 + i\mu_q) \\
 &\stackrel{q_4 \rightarrow q_4 + i\mu_q}{\underset{p=q-k}{\equiv}} \int_q S(\vec{q}, q_4) S(\vec{p}, p_4) \tilde{K}(\vec{p}, p_4, \vec{q}, q_4) \sim \Pi_{vac}(\vec{k}, k_4) \\
 \langle \bar{\Psi}\Psi \rangle &\sim \int_q S(\vec{q}, q_4 + i\mu_q) \stackrel{q_4 \rightarrow q_4 + i\mu_q}{\equiv} \int_q S(\vec{q}, q_4) \sim \langle \bar{\Psi}\Psi \rangle_{vac}
 \end{aligned} \tag{2.146}$$

The quark condensate, as observable, stays constant below the mass gap and therefore reflects the Silverblaze property. The other two equations show, that the quark self-energy and the quark loop at finite chemical potential can be calculated by the analog expressions in vacuum, if we consider the vacuum expressions at a certain point of the complex plane. For the validity of the last two equations, it is important to choose a kernel with a consistent dependence on the chemical potential: $K(p_4 + i\mu_q, q_4 + i\mu_q)$. For this purpose, we have to consider the vertex, included in the kernel. In the quark DSE we use a vertex $\Gamma(p, q) = \Gamma(k = p - q)$, whose chemical potential dependence drops out. Consequently the truncation scheme of the quark DSE does not violate the relation mentioned above. For the gluon DSE, in contrast, we have to use a vertex of the form $\Gamma(p, q) = \Gamma(p^2 + q^2 = \vec{p}^2 + p_4^2 + \vec{q}^2 + q_4^2)$, since $\Gamma(p, q) = \Gamma(k = p - q)$ spoils the multiplicative renormalizability. But this vertex violates the Silverblaze property, since a consistent implementation of the chemical potential would require a dependence on $(p_4 + i\mu_q)^2$ and $(q_4 + i\mu_q)^2$. This violation, however, is only weak. As result, we will accept this violation in our calculations.

Chapter 3

QCD phase diagram

The goal of this chapter is to calculate the QCD phase diagram, using the most elaborate truncation with adequate input and as few approximations as possible. For this purpose, we investigate at first the quark and gluon propagators, then we pass to the order parameters including the thermal mass of the gluon, which is only calculable due to the unquenching effects included in this truncation and finally we reach the QCD phase diagram. But first we have to present the properties and specifications of the truncation scheme and to discuss the related gluon renormalization. The truncation thereby is adopted from previous works (see for example [22] and [2]), where the impact of additional quark flavors on the QCD phase diagram were studied. Additionally, we can compare with FRG results [34], [35], which use the Polyakov extended quark-meson model.

3.1 Truncation scheme

In this section we introduce the approximations, which are necessary to make the system of coupled Dyson-Schwinger equations numerically calculable. As already mentioned before, the Dyson-Schwinger equations are the foundation of an infinite tower of coupled integral-equations. Since it is too complicated to solve them self-consistently, the main difficulty in the DSE-framework is to find a truncation scheme that correctly describes the relevant physics, while cutting the infinite tower of integral equations. Especially in the case of QCD-thermodynamics, we have to be very attentive. In this case the infinite tower of Dyson-Schwinger equations has to be cut-off such that the temperature and density dependence of the n-point functions, that are not determined self-consistently, are carefully approximated.

To truncate the system, input from other sources - such as symmetries, constraints or other calculation methods - are necessary. Therefore, in this work, the truncation scheme has two key points: An approximation in the gluon DSE and an approximation for the full quark-gluon vertex. Since studies to the full gluon DSE are very difficult and mostly restricted to large and infinite temperatures, the gluon is truncated by separating the quark back-coupling (quark-loop for each flavor) and the pure gluonic Yang-Mills part. While the Yang-Mills part is replaced by

temperature dependent quenched lattice fit data - neglecting second order unquenching effects¹ in Yang-Mills diagrams - the quark back-coupling term introduces an implicit chemical potential dependence and ensures that important temperature effects of the unquenched gluon are taken into account. By splitting these two terms and calculating them separately no interactions between diagrams contained in Yang-Mills part and back-coupling terms are involved. But as comparisons with unquenched lattice data [10] for the vacuum and the finite temperature and vanishing chemical potential case shows, this approximation is valid within an error of a few percent (below five percent). Due to this truncation the gluon DSE (2.26) boils down to the following equation

$$D_{\epsilon\nu}^{-1}(k) = \left[D_{\epsilon\nu}^{\text{lat. que}}(k) \right]^{-1} + \Pi_{\epsilon\nu}^{QL}(k) \quad (3.1)$$

where we omitted color indices. The corresponding quark-loop is given by

$$\Pi_{\epsilon\nu}^{QL}(k) = -\frac{g^2}{2} \sum_f^{N_f} Z_{1F}^f \not{\int}_q \text{tr}_D \left[\gamma_\epsilon S^f(p) \Gamma_\nu(p, q, k) S^f(q) \right] \quad (3.2)$$

and the quenched gluon propagator $D_{\epsilon\nu}^{\text{lat. que}}(k)$ is determined by temperature dependent quenched lattice fits for the transversal ($Z_T^{\text{lat. que}}$) and the longitudinal ($Z_L^{\text{lat. que}}$) gluon dressing functions [36], which are given by the equation

$$Z_{T,L}^{\text{lat. que}}(k^2) = \frac{x}{(x+1)^2} \left[\left(\frac{\hat{c}}{x + a_{T,L}(T)} \right)^{b_{T,L}(T)} + x \left(\frac{\beta_0 \alpha}{4\pi} \ln(1+x) \right)^\gamma \right] \quad (3.3)$$

Here we use the shorthand $x = k^2/\Lambda^2$, with k being the four momentum of the gluon. $\hat{c} = 5.87$ and $\Lambda = 1.4$ GeV are temperature-independent parameters. The logarithmic term leads to the perturbative running with the anomalous dimension $\gamma = \frac{-13N_c + 4N_f}{22N_c + 4N_f}$ in the ultraviolet momentum area. At this point, we have to bear in mind that the fit function represents the quenched gluon dressing functions. Consequently N_f has to be equal to 0 in the anomalous dimension of this fit-function. Furthermore $a_{T,L}(T)$, $b_{T,L}(T)$ describe temperature dependent fit parameters. With a transition temperature of $T_c = 277$ MeV for the quenched SU(3) theory, these temperature-dependent fit parameters are given by

$$a_L(t) = \begin{cases} 0.595 - 0.9025 \cdot t + 0.4005 \cdot t^2 & \text{if } t < 1 \\ 3.6199 \cdot t - 3.4835 & \text{if } t > 1 \end{cases},$$

$$a_T(t) = \begin{cases} 0.595 + 1.1010 \cdot t^2 & \text{if } t < 1 \\ 0.8505 \cdot t - 0.2965 & \text{if } t > 1 \end{cases},$$

¹Unquenching effects describe effects resulting from quark (matter sector in general) back-coupling onto the Yang-Mills part. In the quenched case the gluon is decoupled from the quark and can be calculated without the knowledge of the quark, but the quark itself depend further on the gluon (Yang-Mills part).

$$\begin{aligned}
 b_L(t) &= \begin{cases} 1.355 - 0.5741 \cdot t + 0.3287 \cdot t^2 & \text{if } t < 1 \\ 0.1131 \cdot t + 0.9319 & \text{if } t > 1 \end{cases}, \\
 b_T(t) &= \begin{cases} 1.355 + 0.5548 \cdot t^2 & \text{if } t < 1 \\ 0.4296 \cdot t + 0.7103 & \text{if } t > 1 \end{cases}
 \end{aligned} \tag{3.4}$$

with the reduced temperature $t := T/T_c$. Adding the same tensor-structure as above (see equation (2.46)), the quenched gluon propagator for finite temperature and the cold dense matter case is given by

$$D_{\epsilon\nu}^{\text{lat que}}(k) = P_{\epsilon\nu}^T(k) \frac{Z_T^{\text{lat que}}(k^2)}{k^2} + P_{\epsilon\nu}^L(k) \frac{Z_L^{\text{lat que}}(k^2)}{k^2} + P_{\epsilon\nu}^{\mathcal{L}}(k)\xi \tag{3.5}$$

or in the vacuum case by

$$D_{\epsilon\nu}^{\text{lat que}}(k) = P_{\epsilon\nu}^{\mathcal{J}}(k) \frac{Z_{T/L}^{\text{lat que}}(k^2; T=0)}{k^2} + P_{\epsilon\nu}^{\mathcal{L}}(k)\xi \tag{3.6}$$

It is notable that the quenched gluon is independent of chemical potential, which enters the gluon DSE only through the quark-loop. Furthermore, the Landau-gauge ($\xi = 0$) is employed throughout this work.

Since the behavior of the vertex at finite temperature and density is unknown, constraints and symmetries have to be used to achieve an appropriate form of the quark-gluon interaction. Therefore, information from lattice or the functional form of the vertex has to be used. At this point, the information to the functional form combines information from the well-known perturbative behavior at large momenta and the approximate form from the Slavnov-Taylor-Identity at small momenta. At large momenta, temperature and density effects are exponentially suppressed, so that the interaction relies entirely on the vacuum structure of the vertex. Furthermore the vertex dressing function combined with the gluon dressing function fulfills the perturbative renormalization-group running of the coupling in ultraviolet. As already mentioned (see also section 2.1.4), the longitudinal part of the vertex is fixed by the Slavnov-Taylor-Identity (STI), but since it is unknown if the exact solution of the Slavnov-Taylor identity has the same Ball-Chiu structure, it is questionable if the full vertex structure, presented in (2.56) (or correspondingly in (2.57)), is a good approximation. Consequently we only will use the first Ball-Chiu term in the following. This means that we only take the leading γ_μ -tensor-structure of the Abelian Ball-Chiu construction into account, which is multiplied with a factorized infrared enhanced function $\Gamma(x)$, that accounts for the non-Abelian dressing effects and the correct ultraviolet running of the vertex. Finally we get for finite temperatures the following vertex

$$\begin{aligned}
 \Gamma_\nu^f(p, q, k) &= \gamma_\nu \Gamma(x) \left(\delta_{\nu,s} \frac{A^f(\vec{p}^2, \omega_p) + A^f(\vec{q}^2, \omega_q)}{2} + \delta_{\nu,4} \frac{C^f(\vec{p}^2, \omega_p) + C^f(\vec{q}^2, \omega_q)}{2} \right) \\
 \Gamma(x) &= \frac{d1}{d2 + k^2} + \frac{x}{1+x} \left(\frac{\beta_0 \alpha(\mu'') \ln[x+1]}{4\pi} \right)^{2\delta}
 \end{aligned} \tag{3.7}$$

with the flavor dependence f and the squared momentum variable x , which is in the case of the quark DSE the gluon momentum squared ($x = \frac{k^2}{\Lambda^2}$) and in case of the quark-loop calculation a sum over the quark momenta ($x = \frac{p^2+q^2}{\Lambda^2}$) due to multiplicative renormalizability. In the cold dense matter case, we use the same ansatz but we have to exchange the discrete Matsubara frequencies by the fourth momentum component. The factorized function $\Gamma(x)$ represents the universal momentum behavior of the leading dressing function of the vertex. It is determined by the qualitative accordance with explicit results for the vertex DSE at zero temperature (see [37] and references therein). The infrared part in $\Gamma(x)$ is fixed by the constant $\Lambda = 1.4\text{GeV}$, the fit parameter $d_2 = 0.5\text{GeV}^2$ and the effective infrared strength of the vertex²

$$d_1 = \begin{cases} 4.6 & \text{in case of quenched theory} \\ 8.05 & \text{in case of unquenched theory with } N_f = 2 + 1 \end{cases} \quad (3.8)$$

While d_2 is fixed to match the transition scale from the infrared to the ultraviolet of the gluon sector, the infrared strength of the vertex d_1 is adjusted to match the temperature behavior (especially the critical temperature) of the condensate in lattice calculations [22]. Information related to the vertex dressing function $\Gamma(x)$ and in particular for the infrared part are encoded in the $G\tilde{H}$ -factor of the approximated Slavnov-Taylor identity (2.52). Studies to the behavior of the ghost dressing function $G(k^2)$ and the ghost-quark scattering kernel $H(k^2)$ can be found in reference [7], [38], [39] and [24].

Concerning the perturbative behavior, the running coupling $\alpha(\mu'')$ at a chosen scale μ'' , the beta-function β_0 and the anomalous dimension of the vertex in this ansatz 2δ are given by

$$\alpha(\mu'') = \frac{g^2}{4\pi} = 0.3, \quad \beta_0 = \frac{11N_c - 2N_f}{3}, \quad \delta = \frac{-9N_c}{44N_c - 8N_f} \quad (3.9)$$

We can emphasize that this vertex ansatz shows some important properties. In the ultraviolet area, where the leading γ_μ -part dominates, the presented ansatz has the correct running of the one-loop resummed perturbation theory. It fulfills charge conjugation symmetry, required for the full vertex. It also contains potential temperature and chemical potential dependencies. Another advantage is that the ghost DSE does not have to be solved simultaneously in this truncation. In vacuum we have to use $\frac{A^f(p^2)+A^f(q^2)}{2}$ instead of $\left(\delta_{\mu,s} \frac{A^f(\vec{p}^2, \omega_p)+A^f(\vec{q}^2, \omega_q)}{2} + \delta_{\mu,4} \frac{C^f(\vec{p}^2, \omega_p)+C^f(\vec{q}^2, \omega_q)}{2}\right)$ in the presented ansatz.

3.2 Gluon renormalization

Now that we introduced a truncation scheme that includes unquenching effects of the gluon and couples different quark flavors via the quark-loop, we have to focus on the renormalization of this gluon. Therefore, we will separate the vacuum and the in-medium cases to highlight different aspects of the renormalization. As in the case of the quark renormalization (see section

²Actually the ratio $\frac{d_1}{d_2}$ is the infrared strength of the vertex, but we will further on refer d_1 as infrared strength.

2.1.5), we first have to introduce a regulator and a regularization scheme. Since we have the same numerical situation as for the quark, the $O(4)$ -UV cutoff plays the role of the regulator. Due to this hard cutoff regulator, spurious quadratic divergences appear in the gluon self-energy, which break translational and gauge invariance. In medium these quadratic divergences are further accompanied by thermal mass like quantities, that we have to be aware of when we later regularize the gluon. Aside of the superconducting phase - where a thermal mass appears, which is transversal to the heat bath ($P_{\epsilon\nu}^T(k)$) - the thermal mass like terms appear only in the $P_{\epsilon\nu}^L(k)$ part of the gluon. The $P_{\epsilon\nu}^L(k)$ part of the gluon, as well as the $P_{\epsilon\nu}^T(k)$ one, is in fact transversal to the gluon four momentum ($P_{\epsilon\nu}^{\mathcal{J}}(k)$) and fulfills

$$\Pi_L(k^2)k^2|_{k^2 \rightarrow 0} = \underbrace{a\Lambda^2}_{\text{quadratic divergence}} + \underbrace{bT^2 + c\mu_q^2}_{\text{thermal mass like}} \quad (3.10)$$

with some constants a , b and c and the hard $O(4)$ -cutoff Λ . Only the first term has to be removed carefully without spoiling the thermal mass like terms. Furthermore, there is an unphysical, quadratically divergent component longitudinal to the gluon four-momentum, which result from the hard cutoff, too. This longitudinal component has to vanish in Landau-gauge. Due to the unphysical longitudinal component, the vacuum self-energy receives the following form

$$\Pi_{\epsilon\nu}(k) = \Pi^{\mathcal{L}}(k)P_{\epsilon\nu}^{\mathcal{L}}(k) + \Pi^{\mathcal{J}}(k)P_{\epsilon\nu}^{\mathcal{J}}(k) \quad (3.11)$$

with the transversal $P_{\epsilon\nu}^{\mathcal{J}}(k)$ and longitudinal $P_{\epsilon\nu}^{\mathcal{L}}(k)$ projectors w.r.t. the four momentum of the gluon - defined in equation (2.28) - and the projected gluon self-energies

$$\begin{aligned} \Pi^{\mathcal{J}}(k) &= \frac{\Pi_{\epsilon\nu}(k)P_{\epsilon\nu}^{\mathcal{J}}(k)}{3} \\ \Pi^{\mathcal{L}}(k) &= \Pi_{\epsilon\nu}(k)P_{\epsilon\nu}^{\mathcal{L}}(k) \end{aligned} \quad (3.12)$$

obtained using the gluon projector rules presented in Appendix A.1.1. The task is now to find a regularization that removes the unphysical components longitudinal to the gluon four momentum and the spurious quadratic divergences (3.10), without spoiling the thermal mass like terms. It transpires that the following projector removes both. Consequently we can define the regularized self-energy by

$$\begin{aligned} \Pi_{\epsilon\nu}^{reg}(k) &= \left[\delta_{\epsilon\alpha}\delta_{\nu\beta} - \delta_{\epsilon\nu}P_{\alpha\beta}^{\mathcal{L}}(k) \right] \Pi_{\alpha\beta}(k) \\ &= P_{\epsilon\nu}^{\mathcal{J}}(k) \left(\Pi^{\mathcal{J}}(k) - \Pi^{\mathcal{L}}(k) \right) \end{aligned} \quad (3.13)$$

This is the same as using the Brown-Pennington projector $P_{\epsilon\nu}^{BP}(k) = \delta_{\epsilon\nu} - 4\frac{k_\epsilon k_\nu}{k^2}$ on $\Pi_{\epsilon\nu}$ directly. The quadratic divergences from the $P_{\epsilon\nu}^{\mathcal{J}}(k)$ and $P_{\epsilon\nu}^{\mathcal{L}}(k)$ gluon parts cancel, leaving only a logarithmic divergent term in the direction longitudinal to heat bath.

Vacuum case

This logarithmic divergence is removed by fixing the renormalization in vacuum. For this purpose we should fix the gluon renormalization constant \tilde{Z}_3 , but due to our truncation scheme we rather replace the gluon renormalization constant by the subtraction of the gluon self-energy at a given gluon renormalization point μ'

$$\Pi_{\epsilon\nu}^{ren}(k) = \Pi_{\epsilon\nu}^{reg}(k) - \Pi_{\epsilon\nu}^{reg}(\mu') \quad (3.14)$$

Therefore this subtraction obeys the renormalization condition

$$\Pi_{\epsilon\nu}^{ren}(\mu') = 0 \quad (3.15)$$

With this in mind, we can project the truncated and renormalized gluon DSE (compare with equation (3.1)) onto the gluon tensor-structure, using the projector rules presented in Appendix A.1.1 and the definitions (2.47) for the dressed gluon and (3.6) for the quenched gluon. Consequently this yields the following DSE for the gluon dressing function in vacuum:

$$[Z(k^2)]^{-1} = \left[Z_{T/L}^{que\ lat}(k^2; T \rightarrow 0) \right]^{-1} + \Pi_{vac}^{ren}(k) \quad (3.16)$$

The corresponding renormalized and regularized gluon self-energies, projected onto the physical gluon tensor-structure, are given by

$$\begin{aligned} \Pi_{vac}^{ren}(k) &= \Pi_{vac}^{reg}(k) - \Pi_{vac}^{reg}(\mu') \\ \Pi_{vac}^{reg}(k) &= \frac{1}{3k^2} \sum_f^{N_f} \Pi_{\epsilon\nu}^{f,reg}(k) P_{\epsilon\nu}^{\mathcal{F}}(k) \end{aligned} \quad (3.17)$$

The regularized gluon self-energy with tensor-structure $\Pi_{\epsilon\nu}^{f,reg}(k)$ is therefore calculated by equation (3.13) and (3.2) without \tilde{Z}_3 .

Medium cases

The regularization method already was constructed such that medium effects - like the appearance of a thermal mass like term - are taken into account when subtracting the divergences. Consequently we only have to study the renormalization. Since the introduction of temperature and chemical potential does not introduce new divergences, we use the vacuum self-energy $\Pi_{vac}^{reg}(\mu')$ at the gluon renormalization point μ' to calculate the renormalized transversal_{hb} $\Pi_{T/L}^{ren}(k)$ and longitudinal_{hb} $\Pi_L^{ren}(k)$ self-energies

$$\Pi_{T/L}^{ren}(k) = \Pi_{T/L}^{reg}(k) - \Pi_{vac}^{reg}(\mu') \quad (3.18)$$

where the regularized transversal (w.r.t. heat bath) $\Pi_T^{reg}(k)$ and longitudinal (w.r.t. heat bath) $\Pi_L^{reg}(k)$ gluon self-energies are defined by

$$\begin{aligned}\Pi_T^{reg}(k) &= \frac{1}{2k^2} \sum_f^{N_f} \Pi_{\epsilon\nu}^{f,reg}(k) P_{\epsilon\nu}^T(k) \\ \Pi_L^{reg}(k) &= \frac{1}{k^2} \sum_f^{N_f} \Pi_{\epsilon\nu}^{f,reg}(k) P_{\epsilon\nu}^L(k)\end{aligned}\quad (3.19)$$

with the longitudinal $P_{\epsilon\nu}^L(k)$ and transversal $P_{\epsilon\nu}^T(k)$ projectors presented in equation (2.41). Like in vacuum the regularized gluon self-energy with tensor-structure is calculated by equation (3.13) and (3.2) without \tilde{Z}_3 . By using the gluon projector rules from Appendix A.1.1 we can project the gluon DSE onto the longitudinal (w.r.t. heat bath) and transversal (w.r.t. heat bath) tensor-structure of the gluon in medium, with the following resulting DSE's for the gluon dressing functions

$$\left[Z_{T/L}(\vec{k}^2, \omega_k) \right]^{-1} = \left[Z_{T/L}^{\text{que lat}}(k^2) \right]^{-1} + \Pi_{T/L}^{ren}(k). \quad (3.20)$$

In addition to these calculations we have to bear in mind, that the gluon self-energy contributes to the thermal mass of the gluon, which is the dominant thermal effect. We already mentioned that the gluon self-energy now is free of quadratic divergences, which are related to the finite cutoff, but still contains infrared divergences due to thermal mass. As a consequence we split the gluon self-energy into a divergence free part (regular part) $\Pi_{T/L}^{regular}(k)$ and a thermal mass $m_{T/L}^{th}(T, \mu_q)$

$$\Pi_{T/L}^{reg}(k) = \frac{\Pi_{T/L}^{reg}(k) \vec{k}^2 \Big|_{\omega_k=0, \vec{k}^2 \rightarrow 0}}{k^2} + \Pi_{T/L}^{regular}(k), \quad (3.21)$$

where the thermal mass is defined by

$$\left[m_{T/L}^{th}(T, \mu_q) \right]^2 := \frac{1}{2} \Pi_{T/L}^{reg}(k) \vec{k}^2 \Big|_{\omega_k=0, \vec{k}^2 \rightarrow 0}, \quad (3.22)$$

and the regular part by

$$\Pi_{T/L}^{regular}(k) = \Pi_{T/L}^{reg}(k) - \frac{2 \left[m_{T/L}^{th}(T, \mu_q) \right]^2}{k^2}. \quad (3.23)$$

This separation is noteworthy since we will calculate the thermal mass with higher accuracy as the regular part and therefore the regular part has to be split up. For more details see C.3. The electric screening mass $m_L^{th}(T, \mu_q)$ is also known as the Debye mass and is always present in the medium. In contrast to that, the magnetic screening mass $m_L^{th}(T, \mu_q)$ only appears in the color-superconducting phase and is also known as Meissner mass.

3.3 Results

In this section we will at first present the results for the quark and gluon propagators for the truncation shown in this chapter for various temperatures T and chemical potentials μ_q , then we will continue with the order parameters - for chiral symmetry breaking - resulting from these propagators. At the end we will conclude with the related QCD phase diagram. The numerical background is detailed in Appendix C and the used model parameters will be mentioned with the related results. To investigate the quark and gluon propagators, we have to decompose them into their tensor-structures. This rather technical task is done in Appendix B.1, including the final equations used for the results that follow.

3.3.1 Quark propagator

At first, we will include the temperature in our investigations of the quark propagator, keeping the chemical potential fixed at $\mu_q = 0$ and demonstrate the effect that the temperature has on the (real) quark dressing functions. For this purpose, we use a light quark mass of $m_{u/d} = 0.8$ MeV for the up and down quark and the experimentally known factor of 27 between the strange quark mass and the light quark mass to fix the strange quark mass ($m_s = 27 \cdot m_{u/d} = 21.6$ MeV). Therefore, we fixed these values, obtained from the GMOR relation, by renormalization conditions at the quark renormalization point $\mu = 80$ GeV. Since previous works [2] showed that QCD with $N_f = 2 + 1$ quark flavor and QCD with $N_f = 2 + 1 + 1$ quark flavor provide almost the same results, we will only discuss the case of $N_f = 2 + 1$ quark flavors. In this case, the related parameters have already been presented in section 3.1.

As one can see in figure 3.1, the starting point of the finite temperature curves increases for increasing temperatures. The reason for this behavior is the fact, that the zeroth ($n_p = 0$) quark (fermionic) Matsubara frequency $\omega_p = \pi T(2n_p + 1)$ does not vanish and we plot against the four momentum $p^2 = \vec{p}^2 + \omega_p^2$ instead of the three momentum \vec{p}^2 . For small temperatures below $T \approx 110$ MeV, there are only small variations in the momentum behavior of all dressing functions and one can readily see that the vacuum limit is fulfilled. Because of the good agreement with the vacuum result of the scalar dressing function one can further speak of a degeneration of the scalar dressing function behavior below this temperature. Additionally, it is important to mention that we can observe the desired degeneration of the two vector dressing functions if we approach the vacuum. The best demonstration for this property is shown in figure 3.1d. For temperatures equal and above $T \approx 110$ MeV we can observe a significant change in the infrared behavior of all dressing functions. In particular, for the scalar dressing function and the related dynamical quark mass this is meaningful. For increasing temperatures, the infrared value of the dynamical quark mass decreases. Since the dynamical quark mass is an order parameter for chiral symmetry, we therefore observe the restoration of chiral symmetry. In the ultraviolet part of the dressing functions, there are no temperature effects visible for momenta bigger than $p^2 \approx 50$ GeV². A test of the precision of the isotropic extrapolation (defined by equation (C.17)), by comparing the results for two sequential Matsubara frequencies for finite temperature, but

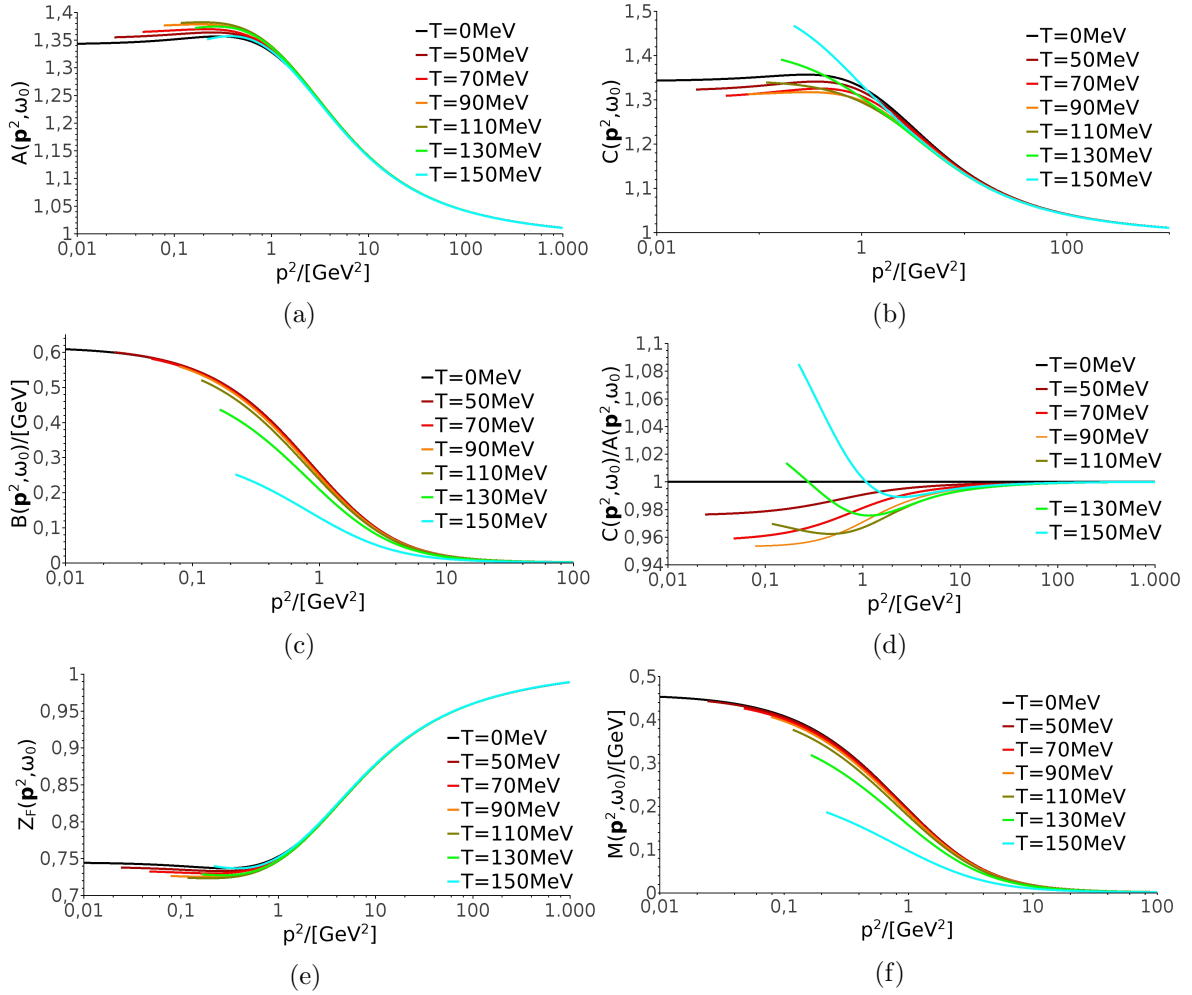


Figure 3.1: Collection of results for the light quark dressing functions for vanishing chemical potential. The figures (a)-(c) display the first $A(\vec{p}^2, \omega_0)$ and second $C(\vec{p}^2, \omega_0)$ vector and the scalar $B(\vec{p}^2, \omega_0)$ dressing function for the zeroth Matsubara frequency ω_0 plotted against the four momentum $p^2 = \vec{p}^2 + \omega_p^2$ for the vacuum (black line) and various other temperatures but vanishing chemical potential. Figure (d) represents the ratio between the two vector dressing functions and (e) and (f) are the corresponding quark wave-function renormalization $Z_F(\vec{p}^2, \omega_0)$ and the dynamical quark mass $M(\vec{p}^2, \omega_0)$.

vanishing chemical potential was already made in a previous work [2]. The problem is that the precision was only tested for vanishing chemical potential, whose inclusion is known to break O(4)-invariance. Consequently we will discuss the equivalent version for non-vanishing chemical potential later on.

The second step is to include the quark chemical potential of the up and down quark in our investigation. The corresponding results are given by 3.2. Thus the strange quark chemical potential is kept zero $\mu_q^s = 0$ MeV. The main effect of this inclusion is that the quark dressing functions are no longer real valued. This means that the quark dressing functions obtain an imaginary component, which has to be investigated. As one can see in figure 3.2 the absolute scale of this imaginary part is at least one order of magnitude smaller than the real part. Further we can observe that the starting point of all curves lies at one specific four momentum, which is equal to the zeroth Matsubara frequency. As one can see in figure 3.2a to 3.2c, the impact of the chemical potential on the real part of all quark dressing functions is small below a chemical potential of about $\mu_q \approx 200$ MeV. Above this critical value the momentum dependence of the vector dressing functions is more influenced and one can observe a strong decrease in the scalar dressing function, which corresponds to a restoration of chiral symmetry. Further, it is noteworthy that increasing chemical potential leads to different UV limits for the Matsubara frequencies of the second vector dressing function. This is a sign that the chemical potential breaks O(4)-symmetry and that the isotropic extrapolation method used in this work - employed to compare with previous works - and described in Appendix C, fails. In figure 3.2d we have a closer look to this topic. We defined a relative difference between the real parts of two second vector dressing functions with sequential Matsubara frequencies:

$$\Delta_n(\vec{p}^2) = \frac{\Re[C(\vec{p}^2, \omega_n)] - \Re[C(\vec{p}^2, \omega_{n+1})]}{\frac{1}{2} (\Re[C(\vec{p}^2, \omega_n)] + \Re[C(\vec{p}^2, \omega_{n+1})])} \quad (3.24)$$

This definition coincides with the definition for vanishing chemical potential, introduced in reference [2]. The relative difference, in this reference, was shown for all quark dressing functions for finite temperature but vanishing chemical potential. In case of non-vanishing chemical potential, we only have to discuss the second vector dressing function, since the scalar and first vector dressing function show the same behavior as stated in the mentioned reference. The relative difference $\Delta_0(\vec{p}^2)$ of the two second vector dressing functions, which corresponds to the difference between the dressing functions of the first two Matsubara frequencies ($C(\vec{p}^2, \omega_0)$ and $C(\vec{p}^2, \omega_1)$), has a non-vanishing relative difference, which additionally increase with the chemical potential. In contrast, the relative difference for higher Matsubara frequencies vanishes for all presented chemical potentials. The other way around, it is obvious that the O(4)-invariance is restored for decreasing chemical potential. Therefore the zero chemical potential limit is naturally fulfilled. To continue we consider the imaginary part of all quark dressing functions. The first observation is the symmetry of the quark dressing functions with respect to the Matsubara frequencies,

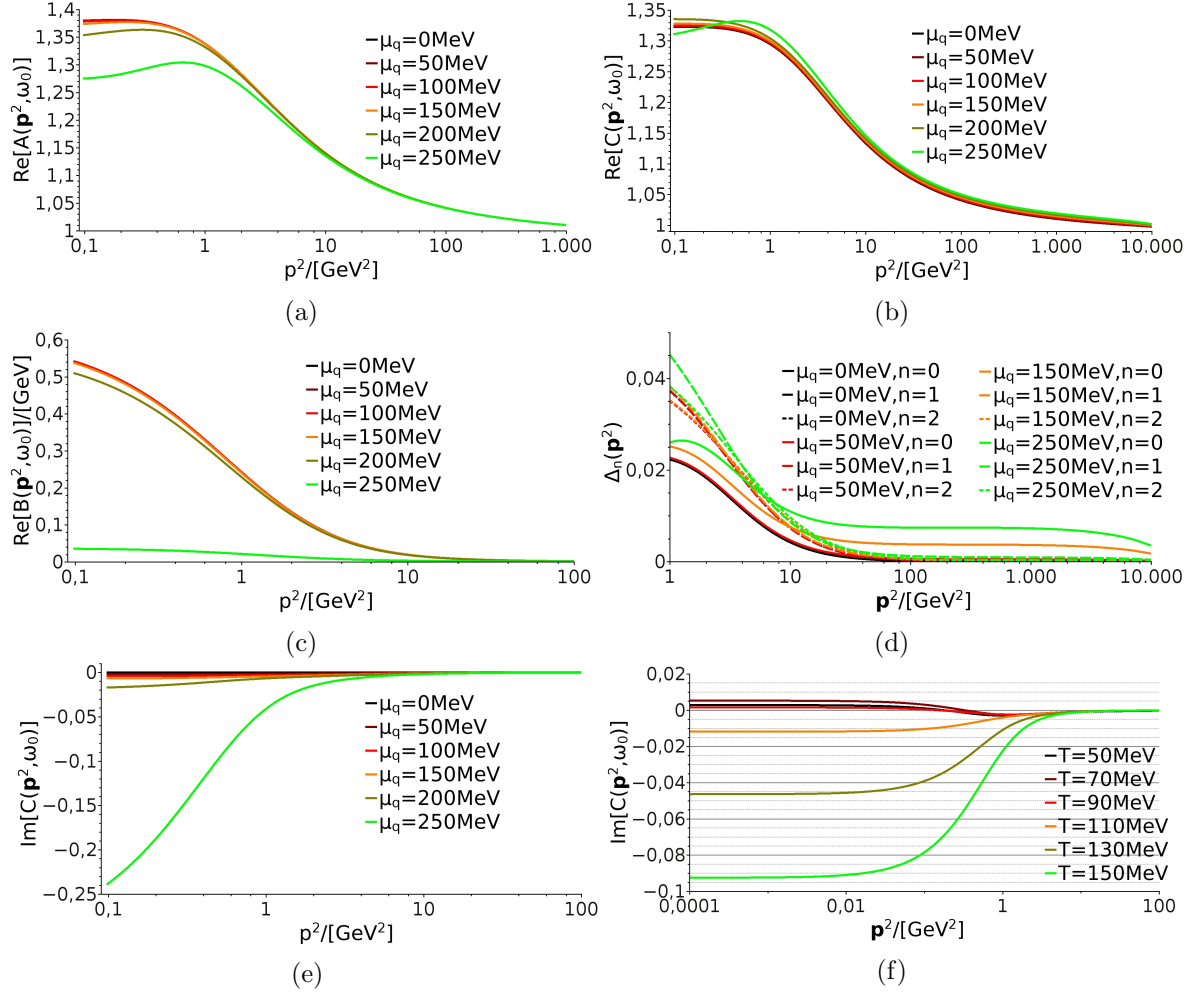


Figure 3.2: Collection of results for the light quark dressing functions for various temperatures and chemical potentials. The figures (a)-(c) show the real part of the first $A(\vec{p}^2, \omega_p)$ and second $C(\vec{p}^2, \omega_p)$ vector and the scalar $B(\vec{p}^2, \omega_p)$ dressing function for the zeroth Matsubara frequency ω_0 plotted against the four momentum $p^2 = \vec{p}^2 + \omega_p^2$ for a fixed temperature of $T = 100$ MeV and various chemical potentials. In figure (d) the difference between the second vector dressing function for two sequent Matsubara frequencies is plotted against the three momentum \vec{p}^2 . Therefore only the UV limit is presented for a fixed temperature of $T = 100$ MeV and various chemical potentials. (e) and (f) demonstrate the imaginary part of the second vector dressing function once for a fixed temperature of $T = 100$ MeV and various chemical potentials and once for a fixed chemical potential of $\mu_q = 100$ MeV and various temperatures. Therefore only the zeroth Matsubara frequency is shown and while (e) is plotted against the four momentum p^2 , (f) is plotted against the three momentum \vec{p}^2 .

which can be displayed by the equation

$$D(\vec{p}^2, \omega_n) = D^*(\vec{p}^2, \omega_{-(n+1)}) \quad (3.25)$$

with $\omega_{-(n+1)} = -\omega_n$ and $D \in \{A, B, C\}$. All quark dressing functions show the same behavior for increasing chemical potential and fixed temperature, therefore we demonstrate only the second vector dressing function in figure 3.2e. Generally we can say, that the imaginary part of the quark dressing functions slowly rise up to a chemical potential of $\mu_q = 200$ MeV. Above this value there is a strong increase in the imaginary part of the dressing functions. If we redo this investigation for fixed chemical potential and increasing temperatures, we observe a rise of the imaginary part of all dressing functions, but striking is the change of sign in the IR area for the vector dressing functions. In the UV area we further can see an improvement to the results of reference [2]. Due to the variation detailed in Appendix C.4 we were able to fix the problem of a non-vanishing imaginary part in the UV limit. Further investigations to the quark propagator can be found in reference [2].

3.3.2 Gluon propagator

After discussing the quark propagator, we have to consider the other fundamental degree of freedom of the QCD. Consequently, this section will be about the influence of temperature and chemical potential onto the gluon propagator, which we will study again by considering the dressing functions. To start, we show the results for the longitudinal and transversal gluon dressing functions in figure 3.3. For different temperatures, the qualitative behavior is not changed significantly, but quantitatively we can observe a difference. While the transverse gluon dressing function is almost temperature independent, the longitudinal gluon dressing function has a visible change in the maximum and the scale, where the dressing function rises. The reason for this behavior is the thermal mass. The main impact of the back-coupling from the matter sector onto the gluon at finite chemical potential and finite temperature results in the thermal mass. Since the Meissner mass vanishes in contrast to the Debye mass, the longitudinal gluon dressing function is affected much more. If we consider the chemical potential dependency, the gluon dressing functions behave similar. To estimate the influence of changes in the thermal mass on the gluon dressing function, it is of interest to investigate the thermal mass and the regular part of the quark-loop separately. Additionally, to get an idea of the difference between the longitudinal and transversal part and the difference between the effects of increasing the temperature in opposite to the effect of increasing the chemical potential, we define

$$\Delta_{\Pi_T, \Pi_L}(\vec{k}^2, 0) = \frac{\Pi_T^{regular}(\vec{k}^2, 0) - \Pi_L^{regular}(\vec{k}^2, 0)}{\frac{1}{2} \left(\Pi_T^{regular}(\vec{k}^2, 0) + \Pi_L^{regular}(\vec{k}^2, 0) \right)} \quad (3.26)$$

and show the corresponding result in figure 3.4. The new defined quantity is not influenced by the thermal mass, since it only depends on the regular part of the gluon. Therefore we can

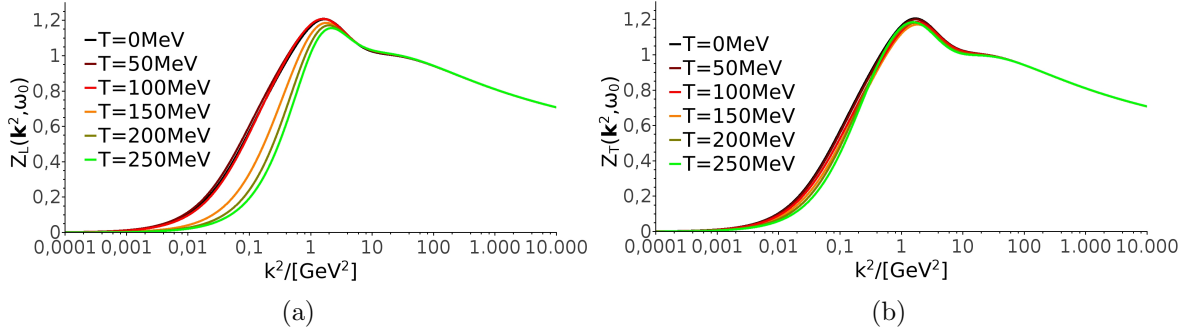


Figure 3.3: Unquenched longitudinal (a) and transversal (b) gluon dressing function for $N_f = 2+1$ quark flavors and for various temperatures and vanishing chemical potential, plotted against the four momentum of the gluon.

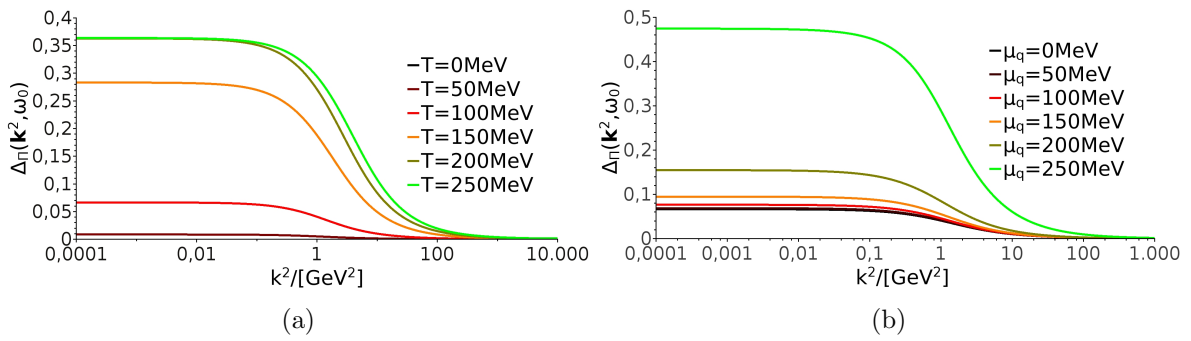


Figure 3.4: Relative difference between the regular parts of the longitudinal and transversal quark-loop for fixed chemical potential and various temperatures in figure (a) and for fixed temperatures and various chemical potentials in figure (b). The relative difference is therefore plotted against the four momentum of the gluon.

investigate the influence of the temperature and the chemical potential on the gluon dressing function, without the changes which are due to the thermal mass.

While the increase of temperature influences the relative difference between the transversal and longitudinal regular part predominantly for small temperatures below $T \approx 200$ MeV and it is almost temperature independent above this critical temperature - except for a small change in the scale of the decrease. An increase of the chemical potential has the opposite effect. This means that the relative difference between the regular parts only changes slightly for chemical potentials below $\mu_q \approx 200$ MeV, but increases strongly above this value. This behavior reflects the chemical potential dependency of the quark dressing functions, shown in figure 3.2. For vanishing temperature and chemical potential the relative difference between the two regular parts should vanish, because of the degeneration of the transversal and longitudinal dressing function in vacuum. This vacuum limit can be seen in figure 3.4a.

Next we will investigate the behavior of the thermal mass resulting from the quark-loop calculation for different temperatures and chemical potentials. The results are shown in figure 3.5. In this figure, we show the thermal mass against the temperature for various chemical potentials and classify the results depending on the type of the “phase” transition for the observed chemical potential. While the thermal mass shows a continuous behavior for chemical potentials

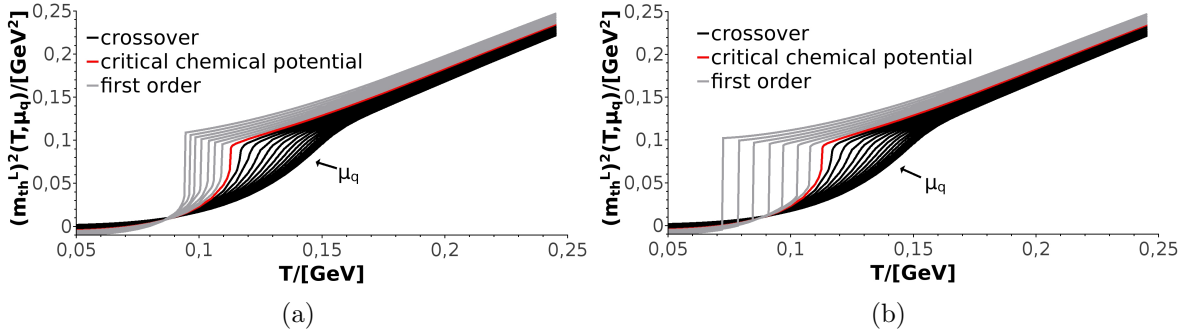


Figure 3.5: Thermal mass resulting from $N_f = 2+1$ quark-loops plotted against the temperature and shown for various chemical potentials (every chemical potential between $\mu_q = 0$ MeV and $\mu_q = 240$ MeV in steps of 10 MeV). While in figure (a) the thermal mass is demonstrated for quarks and gluons corresponding to the crossover (black lines) and the upper spinodal solution (gray lines), figure (b) shows the crossover (black lines) and the lower spinodal solution (gray lines). In both figures the red line represents the thermal mass against the temperature for the critical chemical potential.

below $\mu_q^c = 170$ MeV, it is discontinuous above this critical value. Later on we will denote the chemical potential region below the critical chemical potential as crossover region and the region above as first order region. Furthermore we can distinguish between two stable solutions above the critical chemical potential, calculated with different starting guesses and different calculation directions. For more information see Appendix C.4 and the next section. In both cases we can observe, that the thermal mass behavior becomes steeper the closer one gets to the critical chemical potential and turns into a discontinuity above this critical value. The temperature where the discontinuity appears, decreases with rising chemical potential but differently for the two stable solutions. Additionally we can see that for high temperatures the behavior of the thermal mass can be described by a straight line with a chemical potential independent slope and different offsets for different chemical potentials $\left((m_{th}^L)^2(T \rightarrow \infty, \mu_q) \approx m \cdot T + b(\mu_q) \right)$. This property, however, is in contrast to hard thermal loop (HTL) calculations, which (to one loop order) predict $(m_{th}^L)^2 \propto T^2$ for high temperatures.

3.3.3 Chiral symmetry order parameter

Until now we investigated the quark and gluon propagators for different temperatures and chemical potentials. However, we already know that these propagators are impossible to measure experimentally because of confinement and gauge invariance. Thus in this section we will investigate observables for chiral symmetry, which are calculated from the fundamental degrees of freedom, but are experimentally measurable. For chiral symmetry we already discussed that we can consider the dynamical generated quark mass $M(\vec{p}^2, \omega_p)$ the chiral susceptibility $\chi(\vec{p}^2, \omega_p)$ and the (regularized) quark condensate $\langle \bar{\Psi}\Psi \rangle(T, \mu_q)$ ($\Delta(T, \mu_q)$). In the following we will utilize the regularized quark condensate, which is defined in (2.139) and describes mainly the dynamically generated part of the quark condensate. The results for the regularized quark condensate for different temperatures and chemical potentials are shown in figure 3.6.

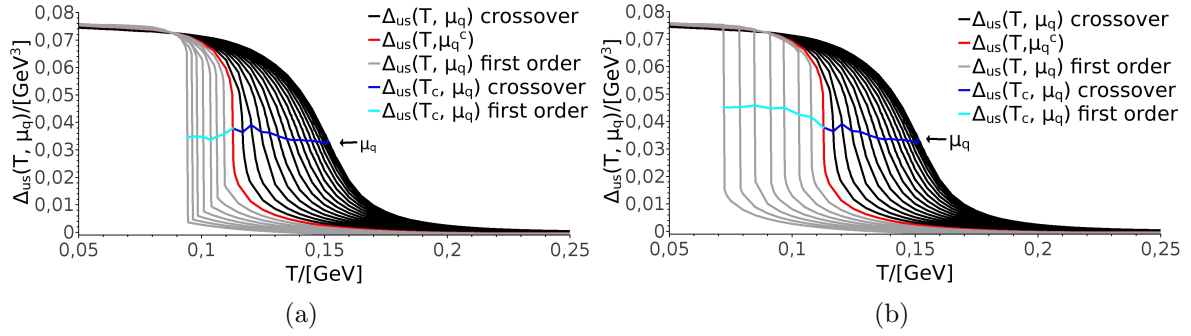


Figure 3.6: Regularized quark condensate against the temperature for different chemical potentials (every chemical potential between $\mu_q = 0$ MeV and $\mu_q = 240$ MeV in steps of 10 MeV). While in figure (a) the regularized quark condensate is shown for the crossover (black lines) and upper spinodal solution (gray lines), figure (b) demonstrate the regularized quark condensate for the crossover (black lines) and lower spinodal solution (gray lines). In both figures the red line represents the regularized condensate against the temperature for the critical chemical potential μ_q^c and the blue lines show the corresponding development of the regularized quark condensate at the (pseudo-) critical temperature $T_c(\mu_q)$.

For high chemical potential and temperature the regularized quark condensate trends towards zero, which is related to a restoration of chiral symmetry. The chiral symmetry, however, is never fully restored since we consider the physical case away from chiral limit. In this case the chiral symmetry gets broken by the explicit mass term independent from the thermodynamic circumstances. Additionally we can observe that for high temperatures and chemical potentials the regularized quark condensate becomes slightly negative, which is a problem of the calculation method and is more detailed in Appendix C.4.

Furthermore we can see a continuous behavior of the regularized quark condensate for small chemical potentials. For increasing chemical potential and for approaching a critical chemical potential of $\mu_q^c = 170$ MeV the decrease of the regularized condensate becomes steeper and turns into a discontinuity above this critical value. With this behavior we can define and distinguish two types of transitions, a continuous transition for chemical potentials below a critical chemical potential of $\mu_q^c = 170$ MeV and a discontinuous phase transition above it. At this point, the discontinuous phase transitions for chemical potentials above the critical chemical potential are phase transitions of first order (we can observe a jump in the curve of the regularized quark condensate). The transition at the critical chemical potential itself is a phase transition of second order (only the first derivative of the curve is discontinuous). Furthermore we find two stable solutions above the critical chemical potential. How these two spinodals can be chosen is detailed in Appendix C.4. For chemical potentials above the critical value we have a distinct temperature for the phase transition between the chiral broken and the chiral symmetric, which equals the temperature of the discontinuity. In the crossover region below the critical chemical potential, however, a transition point is not properly defined as already mentioned in section 2.3.2. Although, the crossover does not describe a real phase transition, we were able to define a pseudo-critical temperature. We introduced two possible definitions for the (pseudo-) critical temperature, which are applicable for the crossover region as well as the first order region. But

while the defined temperatures differ in the crossover region, they are equal in the first order phase transition region. In the following, we will utilize the inflection point method in equation (2.143) as definition of the (pseudo-) critical temperature. By doing so we can observe the development of the regularized quark condensate at the (pseudo-) critical temperature (see the blue lines in figure 3.6). Additionally we can see that the pseudo-critical temperature $T_c(\mu_q)$ decreases in the crossover region (dark blue line) and also in the first order phase transition region (blue line). For the later one we can say, that the critical temperature of the second solution (lower spinodal) decreases faster. Therefore we have our first hints for the behavior and properties of the coexistence lines in the QCD phase diagram. With this in mind we now can turn our interest onto the QCD phase diagram.

3.3.4 QCD phase diagram

In the last section we investigated the regularized quark condensate for different chemical potentials and temperatures and already saw some hints on the QCD phase diagram. In this section we now will discuss the properties of the phase diagram, resulting from the presented quark condensate for $N_f = 2 + 1$ quark flavors. In the phase diagram we show transition lines and mention their type of transition. For this purpose, we use the same pseudo-critical temperature as in the last chapter for the crossover region (denoting the crossover as a phase transition in the following, although this is a false description, since it is a continuous change) and the temperature where the discontinuity appears for the critical temperature of the first order phase transitions. With this in mind we get the QCD phase diagram presented in figure 3.7.

The crossover transition line starts at $T_c^{infl}(\mu_q = 0) = 151.25$ MeV and turns at the second order critical end point into a phase-coexistence-area, specified by the upper and lower spinodals. In this area the phases exist simultaneously but locally separated. The second order critical end point, which separates the crossover region from the first order phase transition region, is given at the point

$$(T^c, \mu_q^c) = (112.75(50), 170.0(5)) \text{ MeV} \quad (3.27)$$

The critical end point as well as the pseudo-critical temperature at vanishing chemical potential differs slightly from previous calculations in reference [2], but can be explained by little changes in the numerical evaluation - for example the separation of the real and imaginary part of the quark DSE shown in equation (C.17). Direct comparisons showed almost perfect agreement. Also the overall behavior corresponds very well with the previous results. For more information to the QCD phase diagram see reference [2].

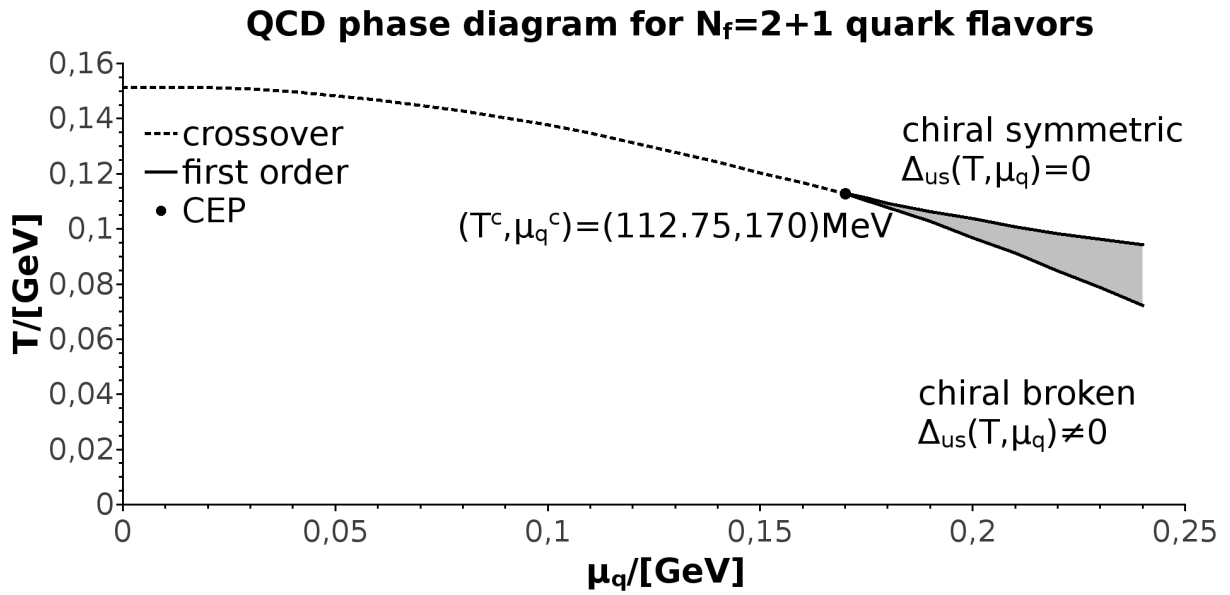


Figure 3.7: QCD phase diagram for $N_f = 2 + 1$ quark flavors. The dashed line represents the crossover transition line, this means a continuous transition between the chiral symmetric and the chiral broken phase, where we defined a pseudo-critical temperature as transition point. The normal line in contrast represents a first order phase transition line, so a discontinuous (first order) phase transition, which limits a phase-coexistence-area where both phases exists simultaneously but at different locations (gray area). The big dot shows the point of the second order phase transition critical end point (CEP).

Chapter 4

Quarks and pions in cold dense matter

If we are searching for an adequate toy model for first results of the quark and pion dressing functions, the Maris-Tandy ansatz is the best choice. Not only that the ansatz leads to the correct pion mass, it also provides the perfect framework to test new results to quarks and pions at finite chemical potential. But at first we compare with the more elaborate model discussed before, by calculating the corresponding QCD phase diagram. To begin with, we have to introduce the truncation scheme.

4.1 Truncation scheme

As already mentioned in section 3.1 the infinite tower of coupled integral equations has to be approximated by imposing a suitable truncation scheme. In this chapter we will utilize a stronger approximation, in which we will introduce a fit function for the running coupling. Therefore we will not calculate the gluon or ghost DSE, neglecting unquenching and coupling effects between different quark flavors. Further we use the Landau gauge ($\xi = 0$) and approximate the vertex by the first Ball-Chiu term:

$$\Gamma_\nu^f(p, q, k) = \gamma_\nu \left(\Gamma_s^f \delta_{\nu s} + \Gamma_4^f \delta_{\nu 4} \right) \Gamma(\vec{k}^2, \omega_k) \quad (4.1)$$

with $\Gamma_s^f = \frac{A^f(\vec{p}^2, \omega_p) + A^f(\vec{q}^2, \omega_q)}{2}$ and $\Gamma_4^f = \frac{C^f(\vec{p}^2, \omega_p) + C^f(\vec{q}^2, \omega_q)}{2}$ in medium and

$$\Gamma_\nu^f(p, q, k) = \gamma_\nu \Gamma_{BC}^f \Gamma(k^2) \quad (4.2)$$

with $\Gamma_{BC}^f = \frac{A^f(p^2) + A^f(q^2)}{2}$ in vacuum. The desired truncation scheme is the so-called Maris-Tandy approximation, which was first proposed in [40]. In this approximation we combine the vertex Γ and gluon Z dressing functions to a renormalization-group invariant coupling α . But for the possibility of an inclusion of thermal mass we will define a new effective coupling $\Omega = \frac{\alpha}{k^2}$,

whereby we get the following connection to the gluon (2.47) and vertex (4.2) in vacuum

$$\frac{1}{\tilde{Z}_3} \frac{g^2}{4\pi} D_{\epsilon\nu}(k) \Gamma_\nu^f(p, q, k) = P_{\epsilon\nu}^{\mathcal{G}}(k) \Omega(k^2) \gamma_\nu \Gamma_{BC}^f \quad (4.3)$$

and correspondingly in medium

$$\frac{1}{\tilde{Z}_3} \frac{g^2}{4\pi} D_{\epsilon\nu}(k) \Gamma_\nu^f(p, q, k) = \left[P_{\epsilon\nu}^T(k) \Omega_T(\vec{k}^2, \omega_k) + P_{\epsilon\nu}^L(k) \Omega_L(\vec{k}^2, \omega_k) \right] \gamma_\nu \left(\Gamma_s^f \delta_{\nu s} + \Gamma_4^f \delta_{\nu 4} \right) \quad (4.4)$$

with the gluon and vertex tensor-structures given in (2.46) and (4.1). The effective coupling Ω for the different cases

$$\begin{aligned} \Omega(k^2) &= \tilde{\Omega}(k^2) \\ \Omega_{T/L}(\vec{k}^2, \omega_k) &= \begin{cases} \tilde{\Omega} \left(\vec{k}^2 + \omega_k^2 + \left(m_{th}^{T/L} \right)^2 \right) & \text{for model with thermal mass} \\ \tilde{\Omega} \left(\vec{k}^2 + \omega_k^2 \right) & \text{for model without thermal mass} \end{cases} \end{aligned} \quad (4.5)$$

is then replaced by

$$\tilde{\Omega}(s) = \pi \frac{\eta^7}{\Lambda^2} x e^{-\eta^2 x} + \tilde{\Omega}_{UV}(s), \quad \tilde{\Omega}_{UV}(s) = \frac{1}{s} \frac{2\pi\gamma_m \left(1 - e^{-s/\Lambda_t^2} \right)}{\ln \left[e^2 - 1 + \left(1 + s/\Lambda_{QCD}^2 \right)^2 \right]} \quad (4.6)$$

with $x = \frac{s}{\Lambda^2}$. The infrared s^2 behavior in the coupling α (correspondingly the s behavior in Ω) only occur for technical convenience. It cancels not only the $\frac{1}{k^2}$ factor of the gluon propagator but also the kinematic singularity stemming from the transverse projector in Landau gauge. The problem with this model is, that the infrared part of the effective coupling Ω vanishes for $s \rightarrow 0$. In opposite, the interaction with one less power in s produces brunch cuts in the integrand [30], but now the infrared part of the effective coupling is constant for $s \rightarrow 0$. Many observables are insensitive to the deep-infrared behavior of the interaction, due to the freeze-out of dynamical quark mass in the infrared part. This is also true for the replacement $\pi\eta^7 x \rightarrow 2\pi\eta^5$ which was suggested in reference [41] with slight readjustment of the parameters. This variation of the model is now called the Qin-Chang-model, which is given by the following equation where the UV part $\tilde{\Omega}_{UV}(s)$ stays the same.

$$\tilde{\Omega}(s) = 2\pi \frac{\eta^5}{\Lambda^2} e^{-\eta^2 x} + \tilde{\Omega}_{UV}(s) \quad (4.7)$$

For both versions (Maris-Tandy and Qin-Chang) the latter term accounts for the right ultraviolet running with the anomalous dimension of the quark mass function $\gamma_m = \frac{12}{11N_c - 2N_f}$ and fixed quark flavor number $N_f = 4$. The corresponding UV parameters for four quark flavors are $\Lambda_t = 1\text{GeV}$ and $\Lambda_{QCD} = 0.234\text{GeV}$. The non-perturbative physics, on the other hand, is encoded in the first term, which is characterized by two parameters: the infrared scale $\Lambda = 0.72\text{GeV}$ and a dimensionless parameter $\eta = 1.8$. The scale Λ , together with the quark mass, is fixed by

experimental data, while the dimensionless parameter η remains free.¹ The only remaining piece is the longitudinal and transversal thermal mass $m_{th}^{L/T}$. For this purpose we can, for example, employ the thermal mass values used in reference [12], which are given by

$$\begin{aligned} (m_{th,HTL}^T)^2 &= 0 \\ (m_{th,HTL}^L)^2 &= \frac{16}{5} \left(T^2 + \frac{6}{5\pi^2} \mu_q^2 \right) \end{aligned} \quad (4.8)$$

Further we can choose if the first Ball-Chiu terms (Γ_s and Γ_4) are used or if they are replaced by the quark wave-function renormalization constant $Z_2^{vac}(\mu, \Lambda)$. Finally we can set $\tilde{Z}_1 = 1$ since the ghost-gluon-vertex is not ultraviolet divergent in Landau gauge. To get the cold dense matter case, we again have to exchange the discrete Matsubara frequencies by the fourth component of the four vector.

4.2 Results for the quark propagator and the QCD phase diagram

In this section we will present our results related to the QCD phase diagram for the simplified truncation presented in this chapter. Since we already discussed the fundamental degrees of freedom - the quark and gluon propagator - in detail in the last chapter, we only will mention some modifications of the quark propagator. Then we will present our results for the quark propagator for cold dense matter. Additionally we will touch upon the chiral symmetry order parameter and show the resulting phase diagram stemming from the new truncation scheme. In addition to the new truncation scheme we use another renormalization point $\mu = 19$ GeV for the quark and calculate the quark mass renormalization constant for a high mass, to circumvent the problem presented in section 2.1.5. The results will be given with the model parameters of the respective ansatz (Maris-Tandy or Qin-Chang). Like in the previous chapter, the strange quark chemical potential is kept zero. Due to the fact that the separation of the imaginary and real part of the quark self-energy, presented in equation (C.17), is not possible for the calculation of the quark on the chemical potential axes until now, we neglect this correction for the following results. To be able to compare our phase diagram for the simplified truncation, we will reproduce the results from reference [42]. Therefore we first have to mention the changes of the quark propagator if we consider the chiral limit.

4.2.1 Quark propagator and condensate in chiral limit

To investigate the influence of the quark mass onto the quark propagator, we will use the vacuum case for sake of simplicity. If, in this case, we approach the chiral limit, the vector dressing

¹The description with Λ and η is a newer definition and the relationship with the usual parameters (ω or σ, D) used in reference [12] is given by $\omega = \frac{\Lambda}{\eta}$ and $D = \eta\Lambda^2$.

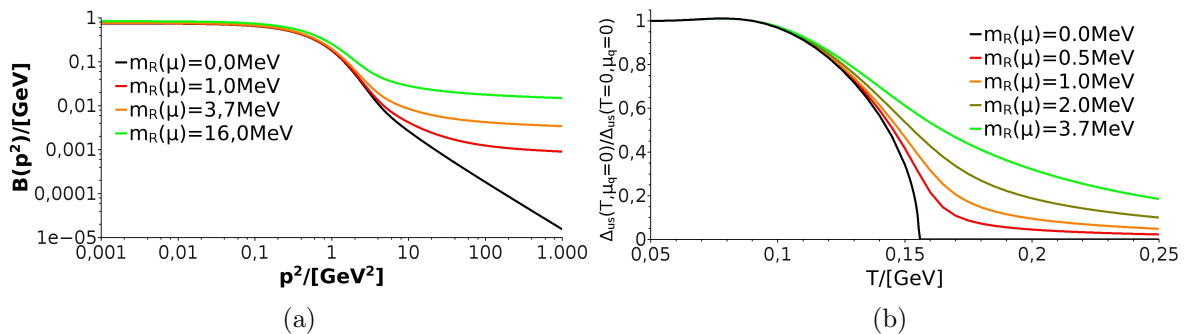


Figure 4.1: (a): Vacuum ($T = 0$ MeV and $\mu_q = 0$ MeV) scalar dressing function $B(p^2)$ for different quark masses $m_R(\mu)$. (b): Normalized regularized quark condensate against the temperature for vanishing chemical potential and various quark masses. The normalization is done by dividing the regularized quark condensate for finite temperatures by the corresponding value in vacuum. The results of both figures are calculated with the Maris-Tandy ansatz presented in equation (4.6) with the parameters given in the section 4.1.

function is not affected very much. As we can see in figure 4.1a, the scalar dressing function converges to a new ultraviolet behavior, if we decrease the quark mass. Ultimately the ultraviolet behavior of the chiral limit is described by the regular asymptotic form shown in equation (2.69) and detailed in section 2.1.5. Further we can see that the infrared part increases with the mass. But the ratio between the maximal dynamical contribution in the infrared and the quark mass input at the renormalization point $\frac{B(0)}{B(\mu)}$ decrease for increasing quark masses.

The next step is to study the impact of the quark mass on the quark condensate. To compare the results for different quark masses it is necessary to consider the regularized quark condensate. The related results for the regularized quark condensate for vanishing chemical potential, but different quark masses and temperatures are shown in figure 4.1b. We can see that the normalized, regularized quark condensates coincide for low temperatures, but show a continual decrease with different strengths for large temperatures. The vacuum limit for the unnormalized, but regularized quark condensate increases slowly for increasing quark masses. By decreasing the quark mass and therefore approaching the chiral limit the dynamical part of the quark condensate decreases, but approaches the zero only in case of the chiral limit. Further we can observe, that the crossover for finite quark masses turns into a phase-transition of second order in the case of the chiral limit. The corresponding critical temperature for the chiral limit with a Maris-Tandy ansatz given by (4.6) is $T_c(\mu_q = 0) = 156.0$ MeV.

4.2.2 Quark propagator and condensate for cold dense matter

To complete the QCD phase diagram we need results for the chemical potential axes, which, in the following, we will refer to as the cold dense matter case. In Appendix C.2 we discuss two possible calculation methods for this case and select a method, which uses quark dressing functions depending on the four momentum q and an angle $z_q = \cos(\theta_q)$ between the four momentum and the fourth component of the same. The corresponding DSE's for the quark

dressing functions are given by

$$\begin{aligned}
 A^f(p^2, z_p) &= Z_2 + \frac{Z_2^2 C_F \alpha(\mu'')}{4\pi^2 p^2 (1 - z_p^2)} \int_{\epsilon^2}^{\Lambda^2} dq^2 \int_{-1}^1 dy_q \int_{-1}^1 dz_q \sqrt{1 - z_q^2} \frac{q^2}{D^f(q^2, z_q)} \\
 &\quad \cdot \left[A^f(q^2, z_q) K_{AA} + C^f(q^2, z_q) (|q|z_q + i\mu_q) K_{AC} \right] \\
 B^f(p^2, z_p) &= Z_2 Z_m m_R(\mu) + \frac{Z_2^2 C_F \alpha(\mu'')}{4\pi^2} \int_{\epsilon^2}^{\Lambda^2} dq^2 \int_{-1}^1 dy_q \int_{-1}^1 dz_q \sqrt{1 - z_q^2} \frac{q^2 B^f(q^2, z_q) K_{BB}}{D^f(q^2, z_q)} \\
 C^f(p^2, z_p) &= Z_2 + \frac{Z_2^2 C_F \alpha(\mu'')}{4\pi^2 (|p|z_p + i\mu_q)} \int_{\epsilon^2}^{\Lambda^2} dq^2 \int_{-1}^1 dy_q \int_{-1}^1 dz_q \sqrt{1 - z_q^2} \frac{q^2}{D^f(q^2, z_q)} \\
 &\quad \cdot \left[A^f(q^2, z_q) K_{CA} + C^f(q^2, z_q) (|q|z_q + i\mu_q) K_{CC} \right]
 \end{aligned} \tag{4.9}$$

with the angle $y_q = \cos(\Psi_q)$ between the external and internal three momentum: $\vec{p}\vec{q} = |\vec{p}||\vec{q}|y_q$. The related angular kernels are presented in (B.14). In this section, we will show our results for these quark dressing functions and the corresponding quark condensate. To check the validity of the results for the cold dense matter case, we have three possible tests: a ‘‘vacuum limit’’ and a ‘‘medium limit’’ as well as the consistency of the quark condensate. To investigate the chemical potential dependency of the quark dressing functions first, we will start with the vacuum limit, where we study if the cold dense matter results trend towards the vacuum result, when we decrease the chemical potential.

The vacuum limit for the real part of the quark dressing functions is given in figure 4.2. The first observation is that the dressing functions are not strongly dependent on the chemical potential. However, there are a few properties, which can be discussed. While the first vector dressing function in figure 4.2a only shows some marginal variations in the middle momentum region and a slight decrease in the infrared, the scalar dressing function in figure 4.2b increases in the infrared region, if the chemical potential is increased. Furthermore, both dressing functions have in common that the chemical potential effects become negligible in the ultraviolet. The second vector dressing function, in contrast, contains chemical potential effects in the UV. As one can see in figure 4.2d, the dressing function strongly varies for different angles z_p between the four momentum p and the fourth component of the same. For certain angles, we have different UV limits, which implies that the O(4)-invariance is broken. Furthermore the difference between these individual UV limits increase with increasing chemical potential. In the infrared area of the second vector dressing function, presented in figure 4.2c, the behavior of the dressing function is similar to the one of the first vector dressing function: we only observe a small decrease of the dressing function, if the chemical potential is increased.

Additionally, another feature of the finite chemical potential can be stated, which will become more important later on. This feature is connected to the angle mentioned earlier and entails that all dressing functions vary in the middle momentum region. This variation is more or less pronounced for the different dressing functions, but increases for all dressing functions if the chemical potential is increased. While the variation strongly affects the scalar and second vector dressing function, the first vector dressing function shows almost no variation. Furthermore, the

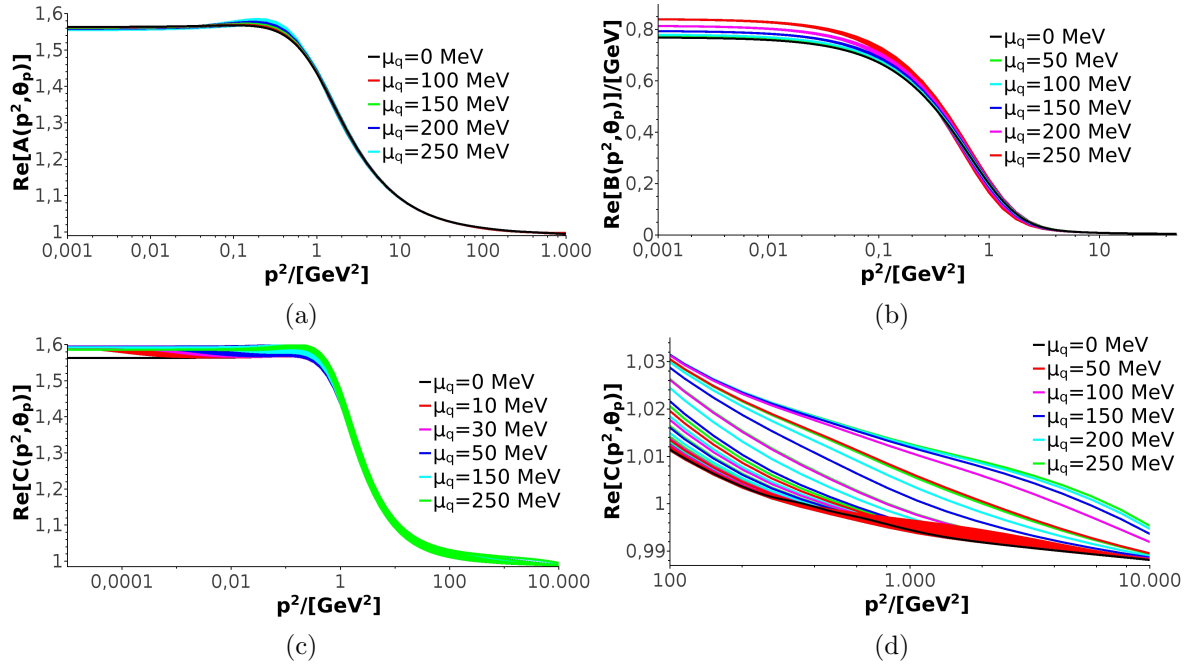


Figure 4.2: Vacuum limit of the real part of the quark dressing functions for vanishing temperature and different chemical potentials including the vacuum case (black line). In figure (a) the real part of the first vector dressing function $A(p^2, \theta_p)$ is plotted against the four momentum p^2 for different angles between the four momentum and the fourth component of the same. The remaining figures are the corresponding displays for the scalar dressing function $B(p^2, \theta_p)$ (b) and the second vector dressing function $C(p^2, \theta_p)$ (c) and (d). The figure (d) therefore is the UV limit of the second vector dressing function. The results are calculated with the Maris-Tandy ansatz presented in (4.6) and the parameters given in section 4.1. Additionally the quark mass is given by $m_R(\mu) = 3.7 \text{ MeV}$ at a renormalization point of $\mu = 19 \text{ GeV}$.

variation of all dressing functions vanish in the IR limit. In the UV limit, however, the variation only vanishes for the first vector and scalar dressing function. Next we study the behavior of the imaginary part of all dressing functions. These imaginary parts decrease continually, if we approach the vacuum limit and ultimately vanish. Furthermore the relation (3.25), found for the medium, also holds for the cold dense matter case. In this case it is given by

$$X^*(p^2, z = \cos(\theta)) = X(p^2, -z) \quad (4.10)$$

with X representing one of the quark dressing functions. If we consider the vacuum limit, it is obvious that the first vector and scalar dressing function trend towards the vacuum solution and that the difference of the individual UV limits of the second vector dressing function vanishes. Furthermore the imaginary parts of all dressing functions vanish and the variation in the middle momentum region decreases. The infrared limit of the second vector dressing function, however, is more complicated since the solutions of the cold dense matter case and the vacuum case differ for all chemical potential. For decreasing chemical potential, the variation of the dressing function (due to different angles) is shifted to the infrared, with the result that the vacuum and the cold dense matter solution coincide for certain angles. If we further calculate the vacuum dressing functions with the cold dense matter method - this means calculating the first and second vector dressing function separately and integrating over a further angle explicitly as shown in equation (4.9) - and set the chemical potential to zero, the actual vacuum result is reproduced perfectly. This includes that the vector dressing function degenerate. Finally, we can say that the vacuum limit is fulfilled for all dressing functions and independent from the calculation method, which is used to calculate the vacuum.

In the following, we will consider a fixed chemical potential and compare the quark dressing function solution of the cold dense matter case with corresponding results for finite temperature. By turning down the temperature, we will study if the finite temperature results trend towards the cold dense matter solution. We will call this vanishing temperature limit: “medium limit”. The corresponding results of all dressing functions in this limit are presented in figure 4.3.

At first, we will consider the medium limit of the real parts of the quark dressing functions, before we will look for the imaginary part. In figure 4.3a and 4.3b we immediately see that the temperature and chemical potential effects in the UV limit of the first vector and the scalar dressing function vanishes for all temperatures. If we further consider decreasing temperatures, the finite temperature results match the IR part of the cold dense matter dressing functions the better, the lower the temperature is. On the other hand, for higher temperatures above 90 MeV, there still is a strong difference between the finite temperature and the cold dense matter results. This difference, however, is less pronounced in case of the scalar dressing function. To achieve good results for the medium limit of the second vector dressing function, it is necessary to improve the numeric. This is done using more and more explicit Matsubara frequencies, the higher the chemical potential is. Applying this high precision, we observe in figure 4.3c that the difference between the finite temperature and the cold dense matter results is clearly visible,

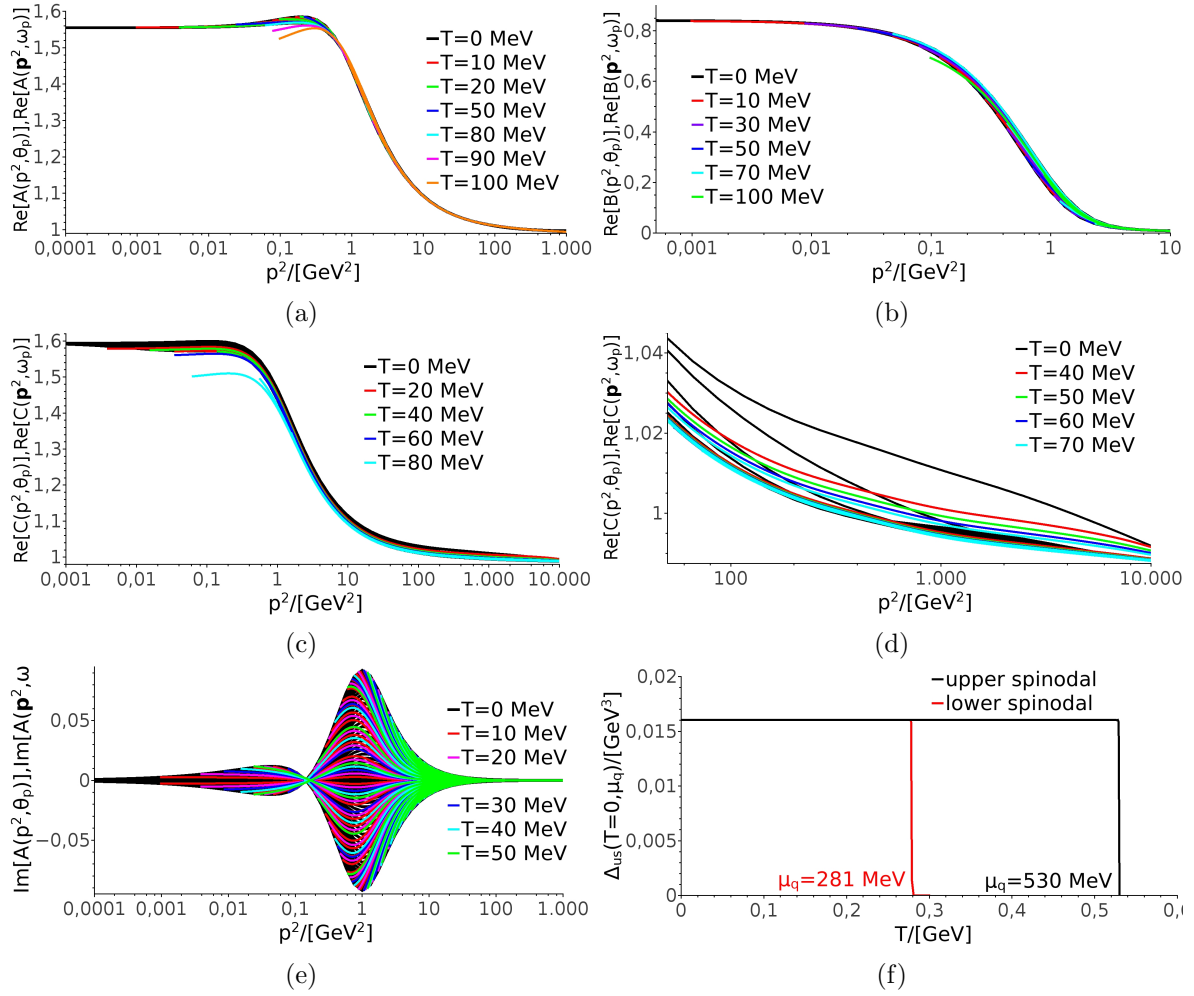


Figure 4.3: Medium limit of the quark dressing functions for fixed chemical potential and different temperatures, as well as the (regularized) quark condensate for the upper and lower spinodal. Figure (a) to (e) are calculated with the Maris-Tandy ansatz given in (4.6), a quark mass of $m_R(\mu) = 3.7$ MeV at a renormalization point of 19 GeV and the parameters given in section 4.1. The result given in figure (f) is calculated with the same Maris-Tandy ansatz but without the UV part of the interaction and two different masses at the same renormalization point, as well as the parameter set $(\eta, \Lambda) = (1.5625, 0.8 \text{ GeV})$. The upper spinodal is calculated in chiral limit, but for the lower spinodal we have to introduce a quark mass of $m_R(\mu) = 1$ KeV. Figure (a) and (e) show the real and imaginary part of the first vector dressing function A for a chemical potential of $\mu_q = 250$ MeV and various temperatures, plotted against the four momentum for different Matsubara frequencies and angles between the four momentum and the fourth component of the same. Figure (b) to (e) are the corresponding ones for the other dressing functions, with figure (b) showing the real part of the scalar dressing function B and (c) and (d) the real part of the second vector dressing function C , where (d) is the UV limit. For the latter two we used an other chemical potential of $\mu_q = 100$ MeV. Figure (f) represents the (regularized) quark condensate in cold dense matter.

already at small temperatures. Additionally, this difference increases fast, so that we can observe a distinct gap between the finite temperature and cold dense matter results in the infrared region for a small temperature of $T = 60$ MeV. To study the UV limit of the second vector-dressing function, we consider figure 4.3d. Here we can see that the zeroth Matsubara frequency, which breaks the $O(4)$ -invariance (compare with figure 3.2d and the discussion in the related section 3.3.1), increases for decreasing temperature and trends towards the cold dense matter solution. This yields that the $O(4)$ -invariance, which is mainly broken by the chemical potential and only slightly by the temperature, gets restored to some extent for increasing temperatures.

It is to note that the higher Matsubara frequencies coincide with the cold dense matter solution, too, if vanishing temperatures are considered. This property is possible, due to the variation of the dressing functions resulting from the different angles. That the higher Matsubara frequencies coincide too, can especially be seen in figure 4.3e. In this figure, we consider the imaginary part of the first vector dressing function. The observations are also applicable for the other dressing functions. We can see that the variation of the dressing functions, due to the different angles z_p , is more pronounced in the imaginary part. Furthermore, all Matsubara frequencies coincide with the cold dense matter solution, as long as the temperature is small enough. While the first vector and the scalar dressing function vanish in the UV and the IR limit, this property does not hold for the second vector dressing function. The second vector dressing function only vanishes in the IR limit. Since an inclusion of the regularization detailed in equation (C.17) into the cold dense matter calculation is not possible until now, we only consider finite temperature results, where this regularization method is not used. The corresponding finite temperature results do not vanish in the UV and coincide with the cold dense matter case, if the temperature is decreased. Finally we can state, that the medium limit is fulfilled.

The remaining test is the consistency of the (regularized) quark condensate. Therefore, we consider the related results given in figure 4.3f, where we use the chiral limit and a simplified version of the Maris-Tandy ansatz. In this case, the Maris-Tandy ansatz given in equation (4.6) without the UV term will be used, to compare with the results of reference [42]. For the same reason, we indicate the results for the condensate of the lower and upper spinodal. As one can see, the (regularized) quark condensate is constant up to the phase-transition points. As result, the Silverblaze property and therefore the last test is fulfilled. Furthermore, we get two critical temperatures ($\mu_q^{lower} = 281$ MeV and $\mu_q^{upper} = 530$ MeV) for the observed discontinuous phase-transition of first order. For the lower solution, we introduced a small mass and considered the regularized quark condensate. While the behavior of the condensate is unchanged if the model is varied and physical masses are considered, the behavior of the quark dressing functions changes. To proof this, we show the results for the vector and scalar dressing functions corresponding to the results presented in 4.3f, plotted against the four momentum for different chemical potentials, in figure 4.4.

While the vacuum limit is still fulfilled, we observe a different behavior especially for the vector dressing function. If we consider figure 4.4b, we see that the scalar dressing function does not change its behavior very strongly. Only the variation of the dressing function, connected

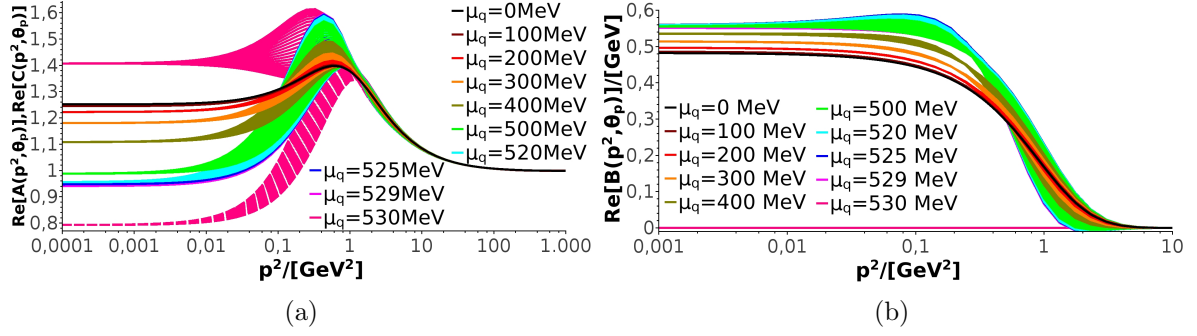


Figure 4.4: Real part of the quark dressing functions for vanishing temperatures and different chemical potentials plotted against the four momentum for different angles between the four momentum and the fourth component of the same. The dressing functions are calculated in chiral limit with an Maris-Tandy ansatz given by (4.6) without the UV part and the parameter set $(\eta, \Lambda) = (1.5625, 0.8 \text{ GeV})$. In figure (a) both vector dressing functions are presented. While the first vector dressing function $A(p^2, \theta_p)$ is represented by solid lines, the second vector dressing function $C(p^2, \theta_p)$ is given by dashed lines. Figure (b) then shows the scalar dressing function $B(p^2, \theta_p)$.

to the different angles, is more pronounced. Additionally, it is striking that the scalar dressing function becomes slightly negative. In the UV, the chemical potential effects are negligible again. Also noteworthy is that the scalar dressing function and therefore the dynamical mass and the quark condensate vanishes above a critical chemical potential of $\mu_q^c = 530 \text{ MeV}$. Above this critical chemical potential the chiral symmetry is completely restored, since there is no explicit chiral symmetry breaking term due to a finite quark mass. Consequently, we have found the critical chemical potential for the discontinuous phase-transition of first order between the chiral broken phase and the chiral symmetric phase. The results for both vector dressing functions, however, are given in figure 4.4a, where the solid line of each color represents the first and the dashed line of the same color the second vector dressing function for a certain temperature. One can immediately see, that there only is a difference between the first and the second vector dressing function for chemical potentials above the already mentioned critical chemical potential of $\mu_q^c = 530 \text{ MeV}$. This also is the case for the lower spinodal solutions with another critical temperature of $\mu_q^c = 281 \text{ MeV}$ and the difference, that the scalar-dressing function does not vanish. In both cases - the chiral limit for the upper spinodal and the small quark mass for the lower spinodal - problems appear in the chiral symmetric phase, which are related to the convergence of the iteration. A discussion to this topic can be found in appendix C.2. Apart from the degeneration of the vector dressing functions and the behavior of the iteration, also the chemical potential dependence increases, if a simplified model and the chiral limit are applied. With increasing chemical potential the infrared part of the vector dressing functions decrease, while the variation due the different angles increase. For the sake of comparison, we finally conclude by mentioning some previous works [33], [43], [44] to the quark at finite chemical potential.

4.2.3 QCD phase diagram

With the discussion of the previous two sections in mind we can investigate the phase diagram resulting from the (regularized) quark condensate. As in the previous chapter we show transition lines with the corresponding type of phase-transition in the phase diagram in figure 4.5.

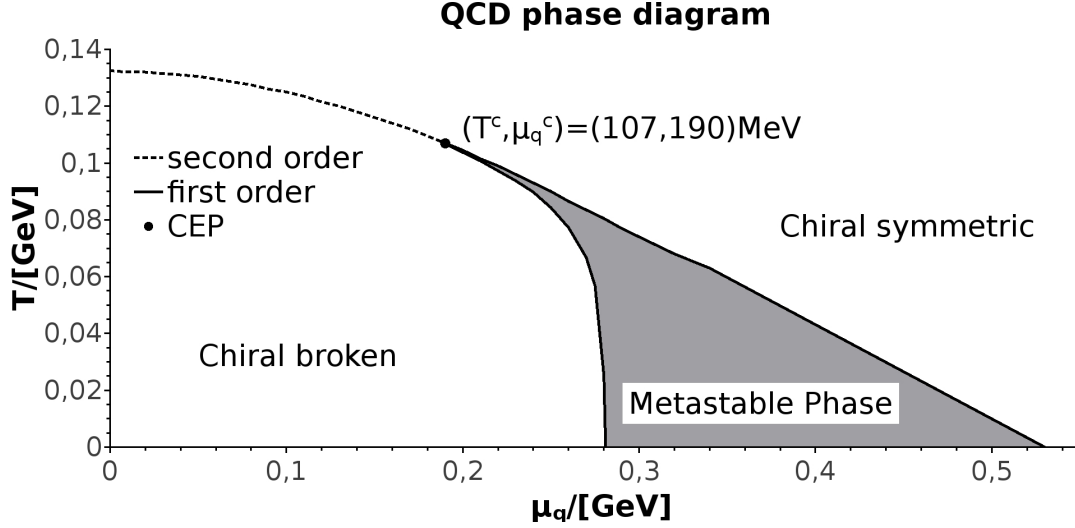


Figure 4.5: Chiral limit phase diagram for the Maris-Tandy ansatz given in equation (4.6) without the UV-part and the parameter set $(\eta, \Lambda) = (1.5625, 0.8 \text{ GeV})$. While the dashed line represents a second order phase-transition, the solid lines are first order phase-transitions limiting the area where both phases appear simultaneously but locally separated (gray area). This phase-coexistence-area between the chiral broken $\langle \bar{\Psi}\Psi \rangle \neq 0$ and the chiral symmetric $\langle \bar{\Psi}\Psi \rangle = 0$ phase, represents a metastable phase where both phases exist simultaneously but locally separated. The big dot shows the position of the second order critical end point (CEP).

In case of chiral limit we observe actual phase-transitions between the chiral symmetric and the chiral broken phase, since there is no additional explicit chiral symmetry breaking that we have to be aware of. As result the transition point is the temperature where the condensate vanishes. In the (chiral limit) QCD phase diagram we can observe, that the second order transition line starts at $T_c(\mu_q = 0) = 132.5 \text{ MeV}$ and turns at the second order critical end point into a phase-coexistence-area, specified by the upper and lower spinodals. The second order critical end point therefore is given at the point

$$(T^c, \mu_q^c) = (107.0(5), 190(1)) \text{ MeV} \quad (4.11)$$

For increasing chemical potential, the critical temperatures of the upper and lower spinodal further decrease, until the solutions intersect with the chemical potential axes at the points:

$$\mu_q^{lower} = 281(1) \text{ MeV} \quad \text{and} \quad \mu_q^{upper} = 530(1) \text{ MeV} \quad (4.12)$$

The second order region of the coexistence line and the upper spinodal show qualitative good agreement with the results presented in [42], but the corresponding critical temperatures calculated in this work are slightly smaller. Since the phase diagram should be reflected for negative

chemical potentials, without a non-analyticity (kink) at the temperature axis, we can argue that the flatter behavior at small chemical potentials is reasonable. Although the qualitative behavior is in good agreement, we see, that the critical end point and the lower spinodal near this point are very different. The reason for this is that we used a different order parameter. In reference [42] the susceptibility was used instead of the regularized quark condensate. Additionally, it is numerically challenging to distinguish between a first and a second order phase-transition in a certain chemical potential area, so that we were obliged to define the critical end point by the point where the upper and lower spinodal degenerate. Finally, we can compare the intersection points of the lower and upper spinodal with the chemical potential axes. While in the lower case we see a good agreement, the upper spinodal is too high by a value of 30 MeV (6%). At the end, we can mention that the QCD phase diagram for the Maris-Tandy ansatz shown in equation (4.6) with the thermal masses (4.8) and physical quark masses can be found in reference [12].

4.3 Pion equations in vacuum and for finite chemical potential

Before we can discuss new results for the pion at finite chemical potential, we have to specify our approximations for the calculation. Instead of using the full pion tensor-structure

$$\Gamma_\pi(P, p) = -i\gamma_5 E(P, p) + \gamma_5 \not{P} F(P, p) + \gamma_5 \not{p} G(P, p) + \gamma_5 [\not{P}, \not{p}] H(P, p) \quad (\text{in vacuum}), \quad (4.13)$$

we only will study the leading pion dressing function $E(P, p)$ in the following results of the vacuum and the cold dense matter case. An extension to the full pion is easy to achieve, but the first pion dressing function already is sufficient to make first statements to the pion properties at finite chemical potential. In Appendix B.2, we discuss two possible parameterizations of the homogeneous BSE for the first pion dressing function. For the following results, we will use the parameterization

$$P = (0, 0, 0, im_\pi), \quad p = (|\vec{p}|(0, 0, 1), p_4), \quad q = (|\vec{q}|(0, \sin(\Psi_q), \cos(\Psi_q)), q_4), \quad (4.14)$$

for the relative momenta p and q as well as the total momentum P , where \vec{p} and p_4 as well as the analogs of q are given by (C.9). This parameterization yields the following representation of the BSE for the first pion dressing function expand in Chebyshev polynomials

$$\begin{aligned} \tilde{E}_j(p^2, P^2) &= \frac{3C_F Z_2^2}{2\pi^2 N} \sum_{n=0}^{N-1} \tilde{T}_j(z_n^p) \int_{\epsilon^2}^{\Lambda^2} dq^2 q^2 \int_{-1}^1 dy_q \int_{-1}^1 dz_q \sqrt{1 - z_q^2} \frac{\alpha(k^2)}{k^2} K_{EE}(q_+, q_-) \\ &\quad \cdot \sum_{l=0}^{\tilde{N}} \tilde{E}_l(q^2, P^2) \tilde{T}_l(z_q) (i)^{l-j} \end{aligned} \quad (4.15)$$

where \tilde{E} corresponds to the modified Chebyshev polynomials $\tilde{T}_k(z_q)$ and is connected to E by $\tilde{E}_j(P^2, p^2) = \left(\frac{1}{\sqrt{2}} \delta_{j,0} + (1 - \delta_{j,0}) \right) E_j(P^2, p^2)$. The angles in this equation are given by

$z_q = \cos(\theta_q)$ and $y_q = \cos(\Psi_q)$. While $\pm q_{\pm} = q \pm \frac{P}{2}$ represents the momenta of the quark and antiquark, $k = q - p$ is the momentum of the gluon. Additionally, N represents the number of external angular grid points $z_n^p = \cos(\frac{2n+1}{2N}\pi)$ and \tilde{N} the order of the Chebyshev polynomial, which is maximally taken into account. Since the quark propagator is the only ingredient of the BSE that changes from vacuum to the cold dense matter case, alone the kernel $K_{EE}(q_+, q_-)$ has to be given separately for these two cases. In vacuum the kernel is given by (B.19), while in cold dense matter it is defined by (B.20). The kernel also is the only ingredient that changes in the normalization factor

$$\begin{aligned}
 \mathcal{N}^2 = \frac{3}{2\pi^3} \frac{\partial}{\partial P^2} & \left(\int_{\epsilon^2}^{\Lambda^2} dq^2 q^2 \int_{-1}^1 dy_q \int_{-1}^1 dz_q \sqrt{1 - z_q^2} K_{EE}(q_+, q_-) \sum_{j,k=0}^{\tilde{N}} \tilde{E}_j(q^2, P_i^2) \cdot \right. \\
 & \left. \cdot \tilde{T}_j(-z_q) \tilde{E}_k(q^2, P_i^2) \tilde{T}_k(-z_q) \right)_{P=P_i}
 \end{aligned} \tag{4.16}$$

of the first pion dressing function ($E = \frac{E_N}{\mathcal{N}}$). The pion decay constant, however, has to be considered separately for the vacuum

$$\begin{aligned}
 f_{\pi} = - \frac{3Z_2^{f,vac}}{4\pi^3 P^2} & \int_{\epsilon^2}^{\Lambda^2} dq^2 q^2 \int_{-1}^1 dy_q \int_{-1}^1 dz_q \sqrt{1 - z_q^2} \sum_{k=0}^{\tilde{N}} \tilde{E}_k^N(q^2, P^2) \tilde{T}_k(z_q) \cdot \\
 & \cdot \frac{B(q_-^2) A(q_+^2) P q_+ + A(q_-^2) B(q_+^2) P q_-}{D(q_-^2) D(q_+^2)}
 \end{aligned} \tag{4.17}$$

and the cold dense matter case

$$\begin{aligned}
 f_{\pi}^t = - \frac{3Z_2^{f,vac}}{4\pi^3 P} & \int_{\epsilon^2}^{\Lambda^2} dq^2 q^2 \int_{-1}^1 dy_q \int_{-1}^1 dz_q \sqrt{1 - z_q^2} \sum_{k=0}^{\tilde{N}} \tilde{E}_k^N(q^2, P^2) \tilde{T}_k(z_q) \cdot \\
 & \cdot \frac{B(\bar{q}^2, q_{4-}) C(\bar{q}^2, q_{4+}) \tilde{q}_{4+} + C(\bar{q}^2, q_{4-}) B(\bar{q}^2, q_{4+}) \tilde{q}_{4-}}{D(\bar{q}^2, q_{4-}) D(\bar{q}^2, q_{4+})},
 \end{aligned} \tag{4.18}$$

since the decay constant is decomposed into two individual decay constants in the cold dense matter case, as discussed in section 2.2.4. In the following results, we only will calculate the temporal part of the pion decay constant, since the parameterization mentioned above does not allow to calculate the spacial part, which one can see in equation (B.28). Because the total momentum P is purely imaginary for the on-shell condition $P^2 = -m_{\pi}^2$ of the homogeneous BSE and the input of the quark consequently has to be calculated on the complex plane, it is necessary to show the method of calculating the quark for complex momenta. To calculate the quark propagator on the complex plane, there are multiple possibilities. The simplest one is to calculate the quark on the real axis first and to perform a further iteration step of the DSE's (presented in section B.1.1 for the vacuum and in equation (4.9) for the cold dense matter case) with complex external but real internal momentum afterwards. This method is straightforward, but involves some problems. The integral over the internal momentum q only converges as long as the external momentum p is close to the real axis. Additionally, one has to

compute the effective interaction for complex arguments, but most of the effective interactions are only designed to reproduce the behavior of the running coupling of QCD $\alpha_s(k^2)$ on the real axis. A more elaborated approach, which does not suffer from this problem, was introduced in reference [45]. Here, the integration variable of the DSE is shifted from the quark to the gluon. Consequently, the complex external momentum now appears in the quark and the effective interaction is only needed on the real axis. This, however, requires the knowledge of the quark dressing functions for complex momenta during the iteration. To calculate the quark in the complex plane during the iteration, we can use the Cauchy method, where we calculate the quark dressing functions iteratively on a hyperbola γ in the complex plane and use the equation

$$f(p_0) = \frac{\oint_{\gamma} \frac{f(p)}{p-p_0} dp}{\oint_{\gamma} \frac{1}{p-p_0} dp} \quad (4.19)$$

to calculate the dressing functions for complex or real momenta inside of this hyperbola. In this work we will use the first simple method. In the corresponding results, we additionally see that we get a better result for the vacuum pion dressing function, if we use the two vector dressing functions A and C instead of only one for the vacuum calculation.

4.4 Results for the pion in vacuum and for finite chemical potential

Finally, we are at the point, where we discuss the pion in the QCD phase diagram. In previous works [8], [46], [47] the pion was calculated for finite temperature and chemical potential with an simplified Maris-Tandy ansatz. In this work, we will restrict ourselves to finite chemical potential but use the full Maris-Tandy ansatz. In this section, we therefore will present the corresponding new results for the pion at finite chemical potential. For this purpose, we need data for the pion in vacuum on which we can build on. We will use the vacuum results for a test of the vacuum limit and generally to compare with the results of the cold dense matter case.

4.4.1 Pion in vacuum

To build a foundation for the following cold dense matter studies, we will consider the normalized first pion dressing function E_N , before we study the observables of the pion (the pion mass and decay constant). The first pion dressing function, which depends on the four momentum and the angle between the four momentum and the fourth component of the same, will be expressed by Chebyshev polynomials, which defines the angular dependency. The corresponding results in form of Chebyshev coefficients are given in figure 4.6.

The zeroth Chebyshev coefficient is related to a constant Chebyshev polynomial. It is given in figure 4.6a and has the biggest contribution to the whole pion dressing function. The coefficient is constant in the infrared but proportional to p^{-2} in the ultraviolet. Therefore, the zeroth coefficient is the only coefficient, which has a non-vanishing contribution in the infrared. The

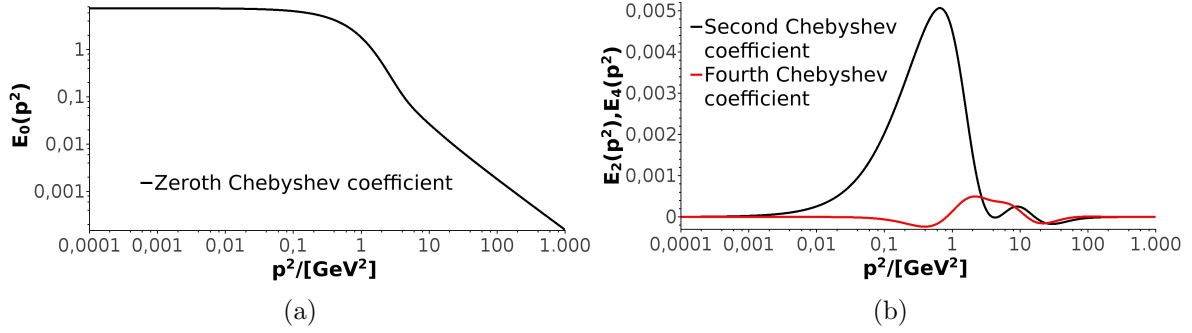


Figure 4.6: First pion dressing function expressed by even Chebyshev coefficients up to the fourth order, plotted against the relative four momentum between the quark and the antiquark. Only the non-vanishing Chebyshev coefficients are presented. The results are calculated using a Maris-Tandy ansatz given in (4.6) with the parameters defined in the related section 4.1. For the quark and the antiquark, quark masses of $m_R(\mu) = 3.7 \text{ MeV}$ at a renormalization point of $\mu = 19 \text{ GeV}$ are used.

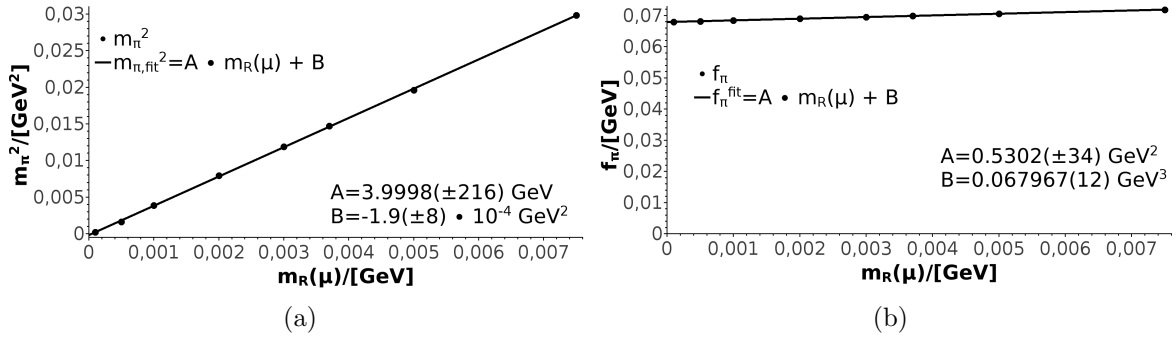


Figure 4.7: Quark mass dependency of the pion mass m_π in (a) and the pion decay constant f_π in (b). While the dots represent the calculated values, the straight line defines a linear fit function with the fit parameters given in the related figure. The results correspond to the first pion dressing function shown in figure 4.6 and some other quark masses.

remaining coefficients trends towards zero for the IR and the UV, with the result, that they only contribute for the momentum interval, where the slope of the zeroth Chebyshev coefficient appears. Additionally we see, that the higher the order of the Chebyshev polynomial is, the lower is the contribution of the corresponding coefficient to the whole pion dressing function. Due to the constrain of C-parity invariance, the coefficients corresponding to odd Chebyshev polynomials vanish. Also the imaginary part of the coefficients can be neglected. These two properties, however, only are possible because of the equal momentum partitioning. At the end, we consider the second and fourth coefficients represented in figure 4.6b. For the second coefficient we can observe an oscillating behavior after the main contribution. This oscillating behavior depends on the manner we calculate the pion dressing function, as we will see later on. The observables, however, are not affected significantly, if the calculation method is changed. As we can see, the fourth component already is small enough to neglect it. Next we examine the observables, which are given in figure 4.7.

As one immediately sees in figure 4.7a, the qualitative behavior of the GMOR relation is fulfilled, since the pion mass m_π is proportional to the root of the quark mass. This further involves that

the pion mass vanishes in chiral limit. Within the applied precision, we can confirm this behavior in our calculation. According to reference [31] we can reproduce a pion mass of $m_\pi = 138.5$ MeV and a pion decay constant of $f_\pi = 92.4$ MeV, under consideration of all tensor-structures of the pion and by using a quark mass of $m_R(\mu) = 3.7$ MeV at the renormalization point $\mu = 19$ GeV. Since we only consider the first pion dressing function, we get a pion mass of $m_\pi = 121.25$ MeV and a pion decay constant of $f_\pi = 69.88$ MeV for the same quark mass. To reproduce the correct pion mass mentioned above we would need a quark mass of $m_R(\mu) = 4.84$ MeV. But in this case, we would get a pion decay constant of $f_\pi = 70.49$ MeV. Consequently it is unavoidable to include the remaining tensor-structures of the pion, to get the right results for the observables. A discussion of the pion in vacuum, which includes up to four tensor structures, can be found in reference [48]. Another discrepancy, due to the omission of the other tensor-structures, is the quantitative behavior of the results given in figure 4.7a. The connection between the pion mass and the quark mass is given by the GMOR relation in equation (2.127) and implies for the fit parameter $A = \frac{2\langle\bar{\Psi}\Psi\rangle}{f_\pi^2}$. If, however, we insert the chiral condensate given by $\langle\bar{\Psi}\Psi\rangle = 0.02057$ GeV³ the fit parameter should be $A = 8.4255$ GeV. Comparisons with Esther Weil, although, showed good agreement for the first pion dressing function. If we consider the quark mass dependency of the pion decay constant, the almost constant behavior of the decay constant is striking. But under closer examination, we see that the pion decay constant actually increases with increasing quark mass with a small gradient. Utilizing the corresponding fit function of the pion decay constant, we can determine the pion decay constant to be $f_\pi = 67.97$ MeV in chiral limit. Finally with all the results from the vacuum in mind, we can study the pion in the cold dense matter case.

4.4.2 Pion for finite chemical potential

In this section, we want to study the chemical potential behavior of the pion properties. For this purpose, we consider the chemical potential dependency of the pion amplitude first. Furthermore, we will show that the vacuum limit of the pion amplitude and the observables is fulfilled. Again, we only will consider the first pion dressing function expressed by Chebyshev polynomials. The related results are presented in figure 4.8.

As one can see, the main contribution to the whole pion dressing function still results from the zeroth Chebyshev coefficient. But the contributions of the other coefficients strongly increase with increasing chemical potential. Furthermore, we observe that the contribution from all Chebyshev polynomials with even orders are positive for rising chemical potential, while the odd orders are negative. Due to this non-vanishing contribution of the odd polynomials for the case of non-vanishing chemical potential, we can clearly state that the C-parity is broken. The vacuum limit of vanishing chemical potential, however, vanishes. Consequently the C-parity is restored if we decrease the chemical potential. As one can see in figure 4.8a, the dominant zeroth contribution is almost independent from chemical potential. We observe that the slope of the function as well as its UV behavior matches the one of the vacuum. Additionally, the function

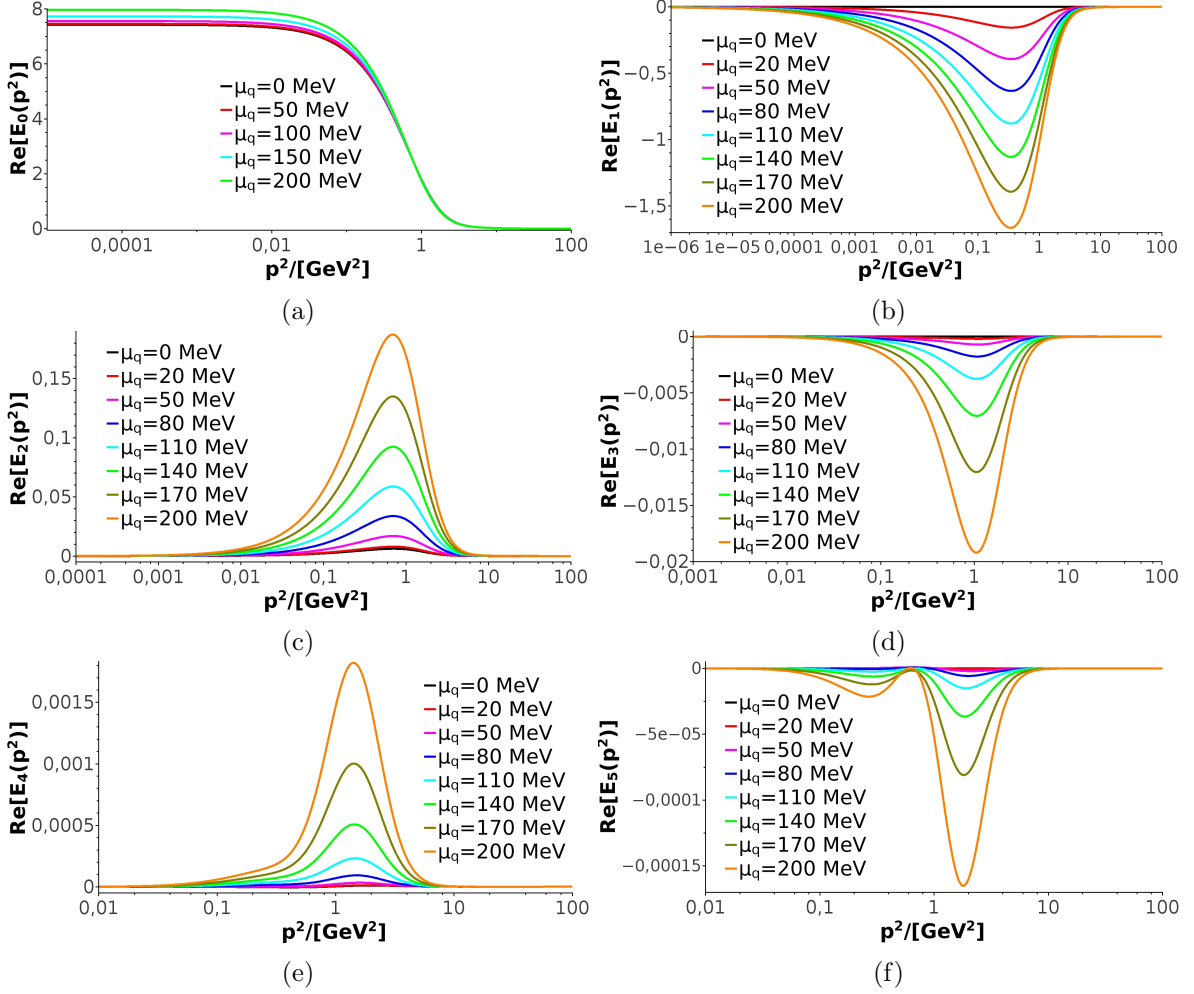


Figure 4.8: Chemical potential dependency of the first six Chebyshev coefficients of the first pion dressing function, plotted against the relative four momentum p^2 between the two constituents. While figure (a) shows the real part of the zeroth Chebyshev coefficient of the first pion dressing function $E_0(p^2, P^2)$ for different chemical potentials including the vacuum, figure (b) to (f) represent the remaining first to fifth Chebyshev coefficients $E_{1-5}(p^2, P^2)$. The results are calculated with a Maris-Tandy ansatz presented in (4.6) with parameters from the related section 4.1. The pion results correspond to light quarks with a quark mass of $m_R(\mu) = 3.7$ MeV at a renormalization point of $\mu = 19$ GeV.

increases slightly in the IR for increasing chemical potential. Furthermore, the vacuum limit of the zeroth coefficient of the first pion dressing function is clearly fulfilled. The remaining coefficients show a much stronger and with the order of the Chebyshev polynomial increasing chemical potential dependence. Since these coefficients trend continuously towards the vacuum solution for decreasing chemical potential, we can easily state that the vacuum limit of the higher coefficients is fulfilled, too. A further observation is that the non-constant coefficients vanish in the UV and the IR just like in the vacuum case. Their contribution is mainly concentrated near the slope of the zeroth Chebyshev coefficient and is shifted to higher momentum intervals for increasing polynomial orders. Finally we can state, that the contribution of every coefficient decreases, at least by one order of magnitude, for every higher polynomial order. Before we discuss the observables, we have to mention that there are two possible methods to calculate the vacuum limit of the pion amplitude. The difference between the two methods is the complex quark input for equation (4.15). In the following we will contrast the two different approaches of the quark:

Method one: The two vacuum quark dressing functions for complex momenta are calculated as explained in section 4.3. This means that we perform a further iteration step of the following DSE with complex external $\tilde{p}^2 = (p \pm i\frac{m_\pi}{2})^2$ but real internal q momentum.

$$\begin{aligned}
 A_{\Im}^f(\tilde{p}^2) &= Z_2 + \frac{Z_2^2 C_F}{2\pi^2 \tilde{p}^2} \int_{\epsilon^2}^{\Lambda^2} dq^2 \frac{q^2 A_{\Re}^f(q^2)}{D_{\Re}^f(q^2)} \int_{-1}^1 dz_q \sqrt{1 - z_q^2} \Omega(k^2) \left(\frac{\tilde{p}^2 + q^2}{2} + \frac{(\tilde{p}^2 - q^2)^2}{2k^2} - k^2 \right) \\
 B_{\Im}^f(\tilde{p}^2) &= Z_2 Z_m m_R(\mu) + \frac{3Z_2^2 C_F}{2\pi^2} \int_{\epsilon^2}^{\Lambda^2} dq^2 \frac{q^2 B_{\Re}^f(q^2)}{D_{\Re}^f(q^2)} \int_{-1}^1 dz_q \sqrt{1 - z_q^2} \Omega(k^2)
 \end{aligned} \tag{4.20}$$

The gluon momentum $k^2 = \tilde{p}^2 + q^2 - 2|\tilde{p}||q|z_q$ consequently is complex. While the dressing function on the right hand side X_{\Re} are the vacuum quark dressing functions on the real axis, the dressing function on the left hand side X_{\Im} are the complex ones.

Method two: The easiest way to calculate the vacuum limit of the quark dressing functions in the cold dense matter case is to set the chemical potential to zero in equation (4.9). As already discussed in section 4.2.2, the two vector dressing functions $A(p^2, z_p)$ and $C(p^2, z_p)$ consequently degenerate for real momenta and lose their angular dependency z_p . To calculate the vacuum quark dressing functions for complex momenta with equation (4.9), we have to set $\mu_q = 0$ and to insert the two degenerated quark vector dressing functions $A_{\Re}(p^2)$ and $C_{\Re}(p^2) = A_{\Re}(p^2)$ as well as the scalar dressing function $B_{\Re}(p^2)$ on the real axis. Furthermore, only the external fourth momentum component is complex $\tilde{p}_4 = p_4 \pm i\frac{m_\pi}{2}$, if we use the parameterization shown

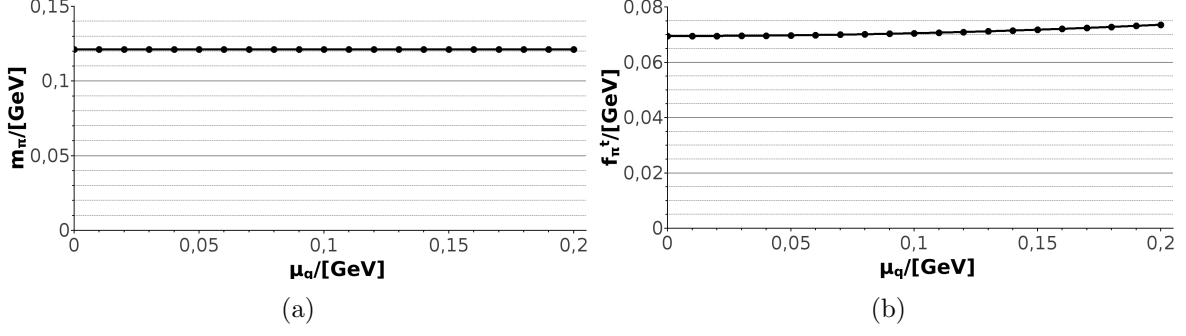


Figure 4.9: Chemical potential dependency of the pion mass m_π (a) and the temporal pion decay constant f_π^t (b) for a quark mass of $m_R(\mu) = 3.7$ MeV at a renormalization point of $\mu = 19$ GeV. The observables correspond to the first pion dressing functions presented in figure 4.8.

in section 4.3. The quark dressing functions for complex momenta therefore are given by

$$\begin{aligned}
 A_{\mathfrak{S}}^f(\vec{p}^2, \tilde{p}_4) &= Z_2 + \frac{Z_2^2 C_F}{4\pi^2 \tilde{p}^2} \int_{\epsilon^2}^{\Lambda^2} dq^2 \frac{q^2 A_{\mathfrak{R}}^f(q^2)}{D_{\mathfrak{R}}^f(q^2)} \int_{-1}^1 dy_q \int_{-1}^1 dz_q \sqrt{1 - z_q^2} \Omega(k^2) \cdot \\
 &\quad \cdot \left[\vec{p}\vec{q} + 2 \frac{\vec{p}\vec{k}}{k^2} (\vec{q}\vec{k} + q_4 k_4) \right] \\
 B_{\mathfrak{S}}^f(\vec{p}^2, \tilde{p}_4) &= Z_2 Z_m m_R(\mu) + \frac{3Z_2^2 C_F}{4\pi^2} \int_{\epsilon^2}^{\Lambda^2} dq^2 \frac{q^2 B_{\mathfrak{R}}^f(q^2)}{D_{\mathfrak{R}}^f(q^2)} \int_{-1}^1 dy_q \int_{-1}^1 dz_q \sqrt{1 - z_q^2} \Omega(k^2) \\
 C_{\mathfrak{S}}^f(\vec{p}^2, \tilde{p}_4) &= Z_2 + \frac{Z_2^2 C_F}{2\pi^2 \tilde{p}_4} \int_{\epsilon^2}^{\Lambda^2} dq^2 \frac{q^2 A_{\mathfrak{R}}^f(q^2)}{D_{\mathfrak{R}}^f(q^2)} \int_{-1}^1 dy_q \int_{-1}^1 dz_q \sqrt{1 - z_q^2} \Omega(k^2) \frac{k_4}{k^2} [\vec{q}\vec{k} + q_4 k_4] \quad (4.21)
 \end{aligned}$$

with the gluon four momentum $k^2 = \vec{k}^2 + k_4^2$, the real gluon three momentum $\vec{k}^2 = \vec{q}^2 + \vec{p}^2 - 2|\vec{p}||\vec{q}|y_q$ and the complex fourth component $k_4 = q_4 - \tilde{p}_4$. The spacial \vec{q} and temporal q_4 internal momenta are connected to the four momentum by equation (C.9).

Inserting the two or three complex quark dressing functions of method one or two into the kernels (B.19) or (B.20) of the equation (4.15), yields two possible methods to calculate the pion amplitude in vacuum. We observe that the pion results of the two methods only differ slightly. The vacuum limit, however, is better fulfilled if we use the second method. If we compare with the results presented in figure 4.6, mainly the oscillating behavior of the second Chebyshev polynomial vanishes.

Next we consider the observables and their chemical potential dependence. As one can see in figure 4.9a the pion mass m_π stays constant for all chemical potentials up to $\mu_q = 200$ MeV. The temporal pion decay constant f_π^t in figure 4.9b, in contrast, is almost constant up to a chemical potential of $\mu_q \approx 50$ MeV and increases thereafter. Thereby, the temporal pion decay constant increases only by 4 MeV up to a chemical potential of $\mu = 200$ MeV. At the end we can conclude by saying that the Silverblaze property is fulfilled, since the pion mass and decay constant stay constant approximately up to half of the pion mass $\mu_q = \frac{m_\pi}{2} \approx 60$ MeV of the quark chemical potential.

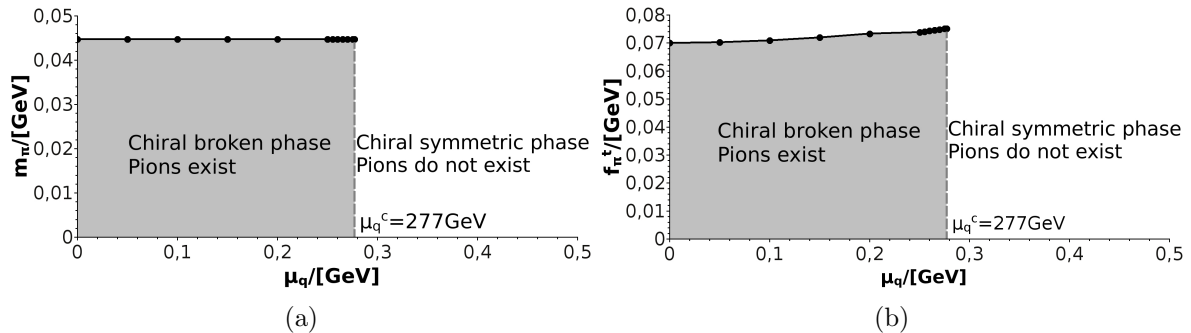


Figure 4.10: Chemical potential dependency of the pion mass m_π (a) and the temporal pion decay constant f_π^t (b) up to the point of chiral phase transition for a quark mass of $m_R(\mu) = 0.5$ MeV at a renormalization point of $\mu = 19$ GeV. The results are calculated with a Maris-Tandy ansatz presented in (4.6) with parameters from the related section 4.1.

Previous works [8], [49], [50] for the pion mass and decay constant for finite chemical potential showed almost the same qualitative behavior. In this context, the same qualitative behavior means that in most of these works the pion mass is almost chemical potential independent and the pion decay constant rises at higher chemical potential. In these references a (simplified) Maris-Tandy ansatz and the Rainbow-ladder approximation $\Gamma_\nu(p, q, k) = \gamma_\nu$ are employed to calculate the quark dressing functions for finite chemical potential at first. Then the pion decay constants, shown in section 2.2.4, are calculated with the approximation $\Gamma_\pi(p) = \frac{B(p)}{f_\pi}$. The pion mass, however is calculated by the GMOR relation (2.127). In reference [49], the pion decay constant stays constant up to a chemical potential of $\mu_q = 200$ MeV and increases thereafter. The pion mass stays constant up to $\mu_q = 200$ MeV too and decreases slightly for higher chemical potential. In reference [50] the chemical potential dependence of the pion mass is stronger. Here the pion mass decreases at first, but increases later on at high chemical potential $\mu_q \geq 280$ MeV. The pion decay constant stays constant up to a chemical potential of $\mu_q \approx 175$ MeV and increases for higher chemical potential. For a critical chemical potential of $\mu_q^c \approx 375$ MeV the pion mass and the pion decay constant exhibit a phase transition and vanish for higher chemical potential. However, in the later work [8] of the same group, the pion mass again is almost chemical potential independent and only decreases slightly. The decay constant, on the other hand, increases strongly already for low chemical potential. In this work a phase transition is found for a critical chemical potential of $\mu_q^c \approx 280$ MeV.

In the following, we want to investigate the pion at this (chiral) phase transition. Since we are not able to find a reasonable QCD phase diagram for physical masses and the Maris-Tandy ansatz presented in (4.6), we have to reconsider the chiral limit QCD phase diagram, which is shown in figure 4.5. We remember that the lower spinodal is calculated with a small mass of $m_R(\mu) = 1$ keV. Consequently, there exists a reasonable QCD phase diagram for small quark masses. In the following, we increase the quark mass up to $m_R(\mu) = 0.5$ MeV, to be able to observe pion masses that are large enough. The resulting pion mass and decay constant for finite chemical potential are shown in figure 4.10. As in the physical case, the pion mass m_π in figure 4.10a stays constant up to a critical chemical potential of $\mu_q^c = 277$ MeV. Above this

critical chemical potential, no pion solution of the BSE can be found anymore, which means that there exist no more pions. Also the temporal pion decay constant f_π^t in figure 4.10b behaves like in the physical case. This means, the temporal pion decay constant stays constant up to the half of the pion mass and increases thereafter until the critical chemical potential $\mu_q^c = 277$ MeV is reached. This critical chemical potential, however, matches very well with the already mentioned one of reference [8]. Furthermore, we have make clear that this critical chemical potential, which marks the point where no pions exist anymore, is connected to the critical chemical potential of the lower spinodal of the chiral symmetry for vanishing temperature and not a confinement-deconfinement phase transition. The quark condensate behave like in figure 4.3f with a phase transition of the lower spinodal at $\mu_q^c = 277$ MeV.

Chapter 5

Conclusion and outlook

The first goal of this work was to reproduce the QCD phase diagram for $N_f = 2 + 1$ quark flavors with lattice fits as input and included unquenching effects, by the back-coupling of the quarks onto the Yang-Mills part. We studied the quark and the unquenched gluon propagators for finite temperature and chemical potential and used the regularized quark condensate as order parameter for the chiral symmetry breaking. In the related QCD phase diagram we found continuous and sharp “phase” transitions, which are in accordance with previous works given by [2]. Because of some numerical changes the critical end point (CEP) is shifted slightly to $(T^c, \mu_q^c) = (112.75(50), 170.0(5))$ MeV. Due to the quark back-coupling onto the Yang-Mills part, we were able to study the thermal mass resulting from the quark-loop. Additionally we successfully implemented the idea of Christian Welzbacher to use a new regularization to prevent errors in the imaginary part of the quark dressing function, which spoiled up to this point the calculation of a quark density. Furthermore we proposed some improvements for the numerical calculation of the quark and gluon at finite temperature and chemical potential.

For an additional, simplified interaction, namely the known Maris Tandy ansatz but without the UV-part and in chiral limit, we calculated the QCD phase diagram using the quark condensate as order parameter for the chiral symmetry again. A comparison with previous results from reference [42] showed good agreement, although the critical end point $(T^c, \mu_q^c) = (107.0(5), 190(1))$ MeV is different. Thereafter, we studied the quark at finite chemical potential and vanishing temperature for the full Maris Tandy model and physical masses as well as in chiral limit and discussed the influence of the chemical potential onto the quark dressing functions. Additionally we proved that the vacuum and medium limit are fulfilled, before we investigated the chemical potential influence on the quark condensate. Here we saw, that the Silverblaze property is fulfilled. Furthermore, we were able to study the phase transition of the chiral symmetry on the chemical potential axis in chiral limit and for small quark masses. Here, the results matches very well with [42].

At the end we calculated the first pion dressing function and the related pion mass and decay constant and discussed their quark mass dependency. We showed that the Gell-Mann-Oakes-Renner relation is qualitatively fulfilled in vacuum. Finally we calculated the first pion dressing

function for finite chemical potential and showed that the vacuum limit is fulfilled. For this purpose, we considered two possible calculation methods for the complex quark. Then, we discussed the chemical potential dependency of the pion mass and decay constant. Here, the pion mass and decay constant showed a behavior, which is in good agreement with the Silverblaze property. Furthermore, we observed that the behaviors of the pion mass and decay constant match qualitatively with the results from reference [49] and [8]. Additionally, we were able to study the behavior of the pion properties at the phase transition of the chiral symmetry for small quark masses. We observed that no pions exist anymore for chemical potentials above the critical chemical potential $\mu_q^c = 277$ MeV of the chiral symmetry phase transition. This critical chemical potential is almost identical to the one found in reference [8].

In the future we will add the full tensor-structure of the pion first, before we expand the pion calculation to finite temperatures. We will study the impact of the inclusion of the remaining tensor-structures and the temperature on the pion mass and decay constant as well as the pion amplitude. Then we will use the unquenched quark as input for the pion, whereby we will extend the unquenched quark to the case of cold dense matter. Next, we repeat the study for further mesons. Ultimately we want to be able to calculate back-coupling effects of the pion and further mesons onto the quark and latter on onto the QCD phase diagram (especially onto the critical end point).

Appendix A

Conventions

The definition of the underlying quantities and shortcuts used in this work are very important to comprehend the theory and the results. Therefore we will present all basis-elements and their corresponding shortcuts based on their appearance in the wave-function of a physical particle. A physical particle is an irreducible representation of the Poincaré group with fixed spin and mass. In QCD two more quantum numbers have to be included, the flavor and the color of the particle. Consequently the wave-function of a physical particle can be decomposed into a color, a flavor and a Dirac part, which further includes the momentum dependence and the spin part.

$$\Psi = \underbrace{\Psi_{\text{Dirac}}}_{\Psi_{\text{Momentum}} \otimes \Psi_{\text{Spin}}} \otimes \Psi_{\text{Color}} \otimes \Psi_{\text{Flavor}} \quad (\text{A.1})$$

In the following we will mention some features for the individual parts. We begin with the Dirac part. But first we mention some shortcuts, which will be used throughout all parts. The Einstein sum convention states that we have to sum over indices, which appear twice.

$$a \cdot b = a_i b^i := \sum_i a_i b^i \quad (\text{A.2})$$

with the arbitrary vectors a and b and the superindex i . Additionally we use the shortcuts $\int_p = \int \frac{d^4 p}{(2\pi)^4}$ and $\int_x = \int d^4 x$ for the momentum and spacial integrals. Further on we will apply natural units $c = 1$, $\hbar = 1$ and $e = 1$ throughout this work.

A.1 Dirac-part

The Dirac-part classifies types of particles by their behavior under Poincaré transformation. The related quantum numbers, corresponding to an invariance under this transformation, are the spin and the mass of the considered irreducible representation. In the following we will consider two types of particles separately, the fermionic spin- $\frac{1}{2}$ -particles and the bosonic spin-1-particles. We will start with the latter one.

A.1.1 Spin-1-particles

The spin-1-particles are the gauge bosons of the underlying theory, which mediate the interaction. In case of the QCD, gluon fields mediate the strong interaction. These fields transform under Poincaré transformation as Lorentz vectors. Consequently their propagators are two-dimensional tensors, described by two Lorentz indices. From QFT courses we further know, that the gluon propagator is transversal to the gluon four momentum. As result we introduced the projectors $P_{\epsilon\nu}^{\mathcal{L}/\mathcal{T}}(k)$ in equation (2.28), which project onto the direction transversal and longitudinal to the gluon four momentum. In this section we will prove that the operators defined in equation (2.28) are actually projectors and we will show some of their properties. The rules that the operators have to fulfill to be projectors are

- idempotency: $P_{\lambda}^2 = P_{\lambda}$
- \exists orthogonal projector: $P_{\lambda} + P_{\lambda}^{\perp} = \mathbb{1}$

Naturally the square of $P_{\epsilon\nu}^{\mathcal{T}/\mathcal{L}}(k)$ stays the same

$$P_{\epsilon\nu}^{\mathcal{T}/\mathcal{L}}(k)P_{\nu\lambda}^{\mathcal{T}/\mathcal{L}}(k) = P_{\epsilon\lambda}^{\mathcal{T}/\mathcal{L}}(k) \quad (\text{A.3})$$

and the mentioned orthogonal projector is just the counterpart, so that the following equation is valid

$$P_{\epsilon\nu}^{\mathcal{T}}(k) + P_{\epsilon\nu}^{\mathcal{L}}(k) = \delta_{\epsilon\nu} \quad (\text{A.4})$$

which implies

$$P_{\epsilon\nu}^{\mathcal{T}}(k)P_{\epsilon\nu}^{\mathcal{L}}(k) = 0 \quad (\text{A.5})$$

too. Consequently the projector rules are fulfilled. Additionally we can state some properties needed for the given projectors:

$$\text{tr}_L \left[P_{\epsilon\nu}^{\mathcal{T}}(k) \right] = 3 \quad \text{and} \quad \text{tr}_L \left[P_{\epsilon\nu}^{\mathcal{L}}(k) \right] = 1 \quad (\text{A.6})$$

In case of finite temperature and cold dense matter we had to introduce projectors that projects (2.41) longitudinal and transversal to the fourth momentum component. For these projectors, we want to prove the rules of projectors once more and additionally we want to show that the new projectors act on the subspace defined by the transversal (w.r.t. gluon four momentum) projector. The property of idempotency again is naturally fulfilled

$$P_{\epsilon\nu}^{T/L}(k)P_{\nu\lambda}^{T/L}(k) = P_{\epsilon\lambda}^{T/L}(k) \quad (\text{A.7})$$

and there is an orthogonal projector to $P_{\epsilon\nu}^{T/L}(k)$ which is the addition of $P_{\epsilon\nu}^{L/T}(k)$ and $P_{\epsilon\nu}^{\mathcal{L}}(k)$. As result the addition of both new projectors $P_{\epsilon\nu}^{T/L}(k)$ equals the transversal (w.r.t. gluon four

momentum) projector

$$P_{\epsilon\nu}^T(k) + P_{\epsilon\nu}^L(k) = P_{\epsilon\nu}^{\mathcal{J}}(k) \quad (\text{A.8})$$

which proves that the new thermal projectors act on the subspace transversal to the gluon four momentum. Similarly we can see this property, if we apply the longitudinal or transversal projectors (w.r.t. the gluon four momentum) at first and then the new projectors

$$P_{\epsilon\nu}^{T/L}(k)P_{\nu\lambda}^{\mathcal{L}}(k) = 0 \quad P_{\epsilon\nu}^{T/L}(k)P_{\nu\lambda}^{\mathcal{J}}(k) = P_{\epsilon\lambda}^{T/L}(k) \quad (\text{A.9})$$

Finally it only remains to mention some further properties of the new projectors:

$$\begin{aligned} P_{\epsilon\nu}^T(k)P_{\nu\lambda}^L(k) &= 0 \\ \text{tr}_L [P_{\epsilon\nu}^T(k)] &= 2 \quad \text{and} \quad \text{tr}_L [P_{\epsilon\nu}^L(k)] = 1 \end{aligned} \quad (\text{A.10})$$

A.1.2 Spin- $\frac{1}{2}$ -particles

Fermionic spin- $\frac{1}{2}$ -particles, such as the elementary quarks, are defined by the Dirac equation of motion

$$(i\cancel{\partial} + g\mathcal{A} - M)\Psi = 0, \quad \bar{\Psi}(i\overleftarrow{\cancel{\partial}} - g\mathcal{A} + M) = 0 \quad (\text{A.11})$$

acting on the quark spinor field Ψ and its counterpart $\bar{\Psi} = \Psi^\dagger\gamma_0$. The vector \mathcal{A}^μ represents the gauge boson, which mediates the interaction and M is the mass matrix $M = \text{diag}(m^{f_1}, \dots, m^{f_{N_f}})$. In this equation we used the Dirac slash notation $\cancel{\partial} := \partial_\mu\gamma^\mu$ and the Dirac-basis elements γ^μ which are defined by the Clifford algebra in Minkowski space

$$\{\gamma_M^\mu, \gamma_M^\nu\} = 2g_-^{\mu\nu} \quad (\text{A.12})$$

where $g_-^{\mu\nu} = \text{diag}(1, -1, -1, -1)$ represents the metric of the Minkowski space, which connects covariant and contravariant vectors by $p_\mu = g_{\mu\nu}p^\nu$. A possible representation of the traceless Dirac-matrices γ^μ in Minkowski space is

$$\gamma^0 = \begin{pmatrix} \mathbb{1} & 0 \\ 0 & -\mathbb{1} \end{pmatrix} \quad \gamma^k = \begin{pmatrix} 0 & \sigma_k \\ -\sigma_k & 0 \end{pmatrix} \quad \gamma^5 = i\gamma^0\gamma^1\gamma^2\gamma^3 = \begin{pmatrix} 0 & \mathbb{1} \\ \mathbb{1} & 0 \end{pmatrix} \quad (\text{A.13})$$

which is called the standard or Weyl-representation. Other representations are possible too but they have to be unitary transformations $\gamma'_\mu = U\gamma_\mu U^\dagger$ of the already presented one. Another representation, which is important is the Chiral or Dirac representation. This representation is connected to the standard representation by the unitary matrix $U = \frac{1}{\sqrt{2}} \begin{pmatrix} \mathbb{1} & -\mathbb{1} \\ \mathbb{1} & \mathbb{1} \end{pmatrix}$. and can be

written as

$$\gamma^0 = \begin{pmatrix} 0 & \mathbb{1} \\ \mathbb{1} & 0 \end{pmatrix} \quad \gamma^k = \begin{pmatrix} 0 & \sigma_k \\ -\sigma_k & 0 \end{pmatrix} \quad \gamma^5 = \begin{pmatrix} \mathbb{1} & 0 \\ 0 & -\mathbb{1} \end{pmatrix} \quad (\text{A.14})$$

It is designed for the ultra-relativistic and the chiral limit, where in both cases the quark masses are neglectable. In these cases the Weyl-spinors Ψ_{\pm} transform separately, which we discussed in section 2.3.1. Due to the last representation we can define chiral projectors

$$P_{\pm} = \frac{1}{2}(\mathbb{1} \pm \gamma_5) \quad \longrightarrow \quad P_{\omega} = P_{\omega}^{\dagger}, \quad \sum_{\omega} P_{\omega} = \mathbb{1}, \quad P_{\omega}^2 = P_{\omega}, \quad P_{\omega}P_{-\omega} = 0 \quad (\text{A.15})$$

who projects the Dirac-spinor Ψ onto the right-handed (+) or left-handed (-) Weyl-spinor Ψ_{ω}

$$\Psi_{\omega} = P_{\omega}\Psi, \quad \bar{\Psi}_{\omega} = \bar{\Psi}P_{-\omega} \quad (\text{A.16})$$

by using the property $\bar{P}_{\omega} = \gamma_0 P_{\omega}^{\dagger} \gamma_0 = P_{-\omega}$. In both representations (standard or chiral) greek indices usually represent the whole four vector, while latin indices address only the spatial part of the four vector ($k \in \{1, 2, 3\}$). For now on we will use the standard representation. The corresponding Pauli matrices, from which the gamma matrices inherit their Clifford algebra, are thereby given by

$$\sigma_1 = \begin{pmatrix} 0 & 1 \\ 1 & 0 \end{pmatrix} \quad \sigma_2 = \begin{pmatrix} 0 & -i \\ i & 0 \end{pmatrix} \quad \sigma_3 = \begin{pmatrix} 1 & 0 \\ 0 & -1 \end{pmatrix} \quad (\text{A.17})$$

To complete the set of basis generators for the Lorentz transformation in four-dimensional representation

$$\{\gamma^A\}_{A=1}^{16} = \{\mathbb{1}, \gamma_{\mu}, i\gamma_{\mu}\gamma_5, \sigma_{\mu\nu}\}, \quad (\text{A.18})$$

we have to define the generators of the Clifford algebra

$$\sigma_{\mu\nu} = \frac{i}{2}[\gamma_{\mu}, \gamma_{\nu}] \quad (\text{A.19})$$

In the dressed quark propagator the tensor-structure, already appearing in the bare quark propagator, gets a momentum dependence by introducing dressing functions belonging to the different basis-elements. To extract these dressing functions we need a method to identify the corresponding basis elements. The desired method is to multiply the propagator with an appropriate projector, who projects the desired dressing function onto a tensor-structure which is not traceless anymore, while the tensor-structures related to the other dressing functions are still traceless. By taking the Dirac-trace we consequently can separate the individual dressing functions. To utilize this method, it is useful to mention some important Dirac-trace rules.

Dirac-trace rules

Using the Clifford algebra presented before and the cyclicity of the trace ($\text{tr}[UV] = \text{tr}[VU]$ with U and V representing some arbitrary $n \times n$ -matrices), we can derive the following general equation in Minkowski space

$$\begin{aligned} \text{tr}_D(\gamma^{\alpha_1} \gamma^{\alpha_2} \dots \gamma^{\alpha_{2n}}) &= g^{\alpha_1 \alpha_2} \text{tr}_D(\gamma^{\alpha_3} \dots \gamma^{\alpha_{2n}}) - g^{\alpha_1 \alpha_3} \text{tr}_D(\gamma^{\alpha_2} \gamma^{\alpha_4} \dots \gamma^{\alpha_{2n}}) + \dots \\ &\quad + g^{\alpha_1 \alpha_n} \text{tr}_D(\gamma^{\alpha_2} \dots \gamma^{\alpha_{2n-1}}) \end{aligned} \quad (\text{A.20})$$

This equation further holds for odd numbers of Dirac-matrices as well, but since the Dirac-matrices are traceless and we can reduce the trace over N Dirac-traces to the trace over one or two Dirac-traces by adding and subtracting the trace of permutations of the first term of the last equation, we can see, that the trace over an odd number of Dirac matrices vanishes.

$$\text{tr}_D(\gamma^{\alpha_1} \gamma^{\alpha_2} \dots \gamma^{\alpha_{2n}} \gamma^{\alpha_{2n+1}}) = 0 \quad \text{with} \quad n \in \mathbb{N} \quad (\text{A.21})$$

The most important applications of the equation (A.20) in this work are

$$\begin{aligned} \text{tr}_D(\gamma^\alpha \gamma^\beta) &= 4g^{\alpha\beta} \\ \text{tr}_D(\gamma^\alpha \gamma^\beta \gamma^\gamma \gamma^\delta) &= 4(g^{\alpha\beta} g^{\gamma\delta} - g^{\alpha\gamma} g^{\beta\delta} + g^{\alpha\delta} g^{\beta\gamma}) \end{aligned} \quad (\text{A.22})$$

A.1.3 Euclidean space

Until now we considered most of the properties of the Dirac part in the Minkowski space, but since we use the Euclidean space for all n-point functions in this work, in particular because of the Matsubara formalism, it is useful to show the connection between the Minkowski and the Euclidean space. The main property of the Euclidean space is, that the difference between co- and contravariant vectors vanishes and that the spacial and temporal parts therefore are not longer separated anymore. This yields a metric of the form $g_{\mu\nu} \rightarrow \delta_{\mu\nu}$ and a scalar product as well as the anti-commutator relation given by

$$a_E \cdot b_E = \sum_{\mu=0}^4 a_{E,\mu} b_E^\mu = \sum_{\nu,\mu=0}^4 a_E^\nu b_E^\mu \delta_{\nu\mu} = \vec{a}_E \vec{b}_E + a_E^4 b_E^4, \quad \{\gamma_E^\mu, \gamma_E^\nu\} = 2\delta_{\mu\nu} \quad (\text{A.23})$$

which is also applicable for the Dirac slash notation by exchanging b_E with γ_E . To achieve this property, we have to modify the Lorentz-vectors, -tensors and gamma matrices in the following way

$$a_E^\mu = \begin{pmatrix} \vec{a} \\ ia_0 \end{pmatrix}, \quad \gamma_E^\mu = \begin{pmatrix} -i\vec{\gamma} \\ \gamma_0 \end{pmatrix}, \quad T_E^{\mu\nu} = \begin{pmatrix} T^{ij} & iT^{i0} \\ iT^{0j} & -T^{ij} \end{pmatrix}, \quad \gamma_E^5 = \gamma^5 \quad (\text{A.24})$$

where 'E' stands for Euclidean and no subscript refers to the Minkowski quantity. Instead of a zeroth component we refer now to a fourth one. Because of the sign convention for Euclidean

gamma matrices, the signs in the Clifford algebra relation change, which implies $(\gamma_E^i)^2 = 1$ $\forall i \in \{1, 2, 3, 4\}$. Consequently we can choose the gamma matrices to be hermitian $\gamma_E^\mu = (\gamma_E^\mu)^\dagger$. The standard representation then reads

$$\gamma_E^0 = \begin{pmatrix} \mathbb{1} & 0 \\ 0 & -\mathbb{1} \end{pmatrix} \quad \gamma_E^k = \begin{pmatrix} 0 & -i\sigma_k \\ i\sigma_k & 0 \end{pmatrix} \quad \gamma_E^5 = i\gamma^0\gamma^1\gamma^2\gamma^3 = \begin{pmatrix} 0 & \mathbb{1} \\ \mathbb{1} & 0 \end{pmatrix} \quad (\text{A.25})$$

where σ_k are again the Pauli-matrices presented above. Also the generators of the Clifford algebra are then hermitian

$$\sigma^{\mu\nu} = \frac{i}{2}[\gamma^\mu, \gamma^\nu] \quad \longrightarrow \quad \sigma_M^{\mu\nu} = -\frac{i}{2}[\gamma_M^\mu, \gamma_M^\nu], \quad (\sigma_M^{\mu\nu})^\dagger = \sigma_M^{\mu\nu} \quad (\text{A.26})$$

Further noteworthy are the alternations of the Lorentz transformation properties. In Minkowski space the quark spinors transform under Lorentz transformation as follows

$$\begin{aligned} \Psi'(x') &= D(\Lambda)\Psi(x) \\ \bar{\Psi}'(x') &= \bar{\Psi}(x)D^{-1}(\Lambda) = \bar{\Psi}(x)\gamma_0 D^\dagger(\Lambda)\gamma_0 \end{aligned} \quad (\text{A.27})$$

with the representation matrix for spin- $\frac{1}{2}$ -particles

$$D(\Lambda) = \exp \left[-\frac{i}{4}\omega_{\mu\nu}\sigma^{\mu\nu} \right] \quad (\text{A.28})$$

which yields that the bilinear $\bar{\Psi}\Psi$ is a Lorentz-invariant. If we consider the Euclidean case the gamma matrices are now hermitian, in contrast to the Minkowski case $(\gamma^0(\gamma^\mu)^\dagger\gamma^0 = \gamma^\mu)$, with the result that the Euclidean generator of the Clifford algebra does not fulfill the equation $\gamma^0(\sigma^{\mu\nu})^\dagger\gamma^0 = \sigma^{\mu\nu}$ anymore. That $\gamma^4 D^\dagger(\Lambda)\gamma^4 = D^{-1}(\Lambda)$ still holds is due to the fact how the infinitesimal Lorentz transformation $\omega_E^{\mu\nu}$ is related to its Minkowski counterpart via (A.24). Finally the bilinear $\bar{\Psi}\Psi$ is still a Lorentz-invariant and $\bar{\Psi}\gamma_E^\mu\Psi$ transforms like a Lorentz vector. At the end we can demonstrate the replacement rules between the Minkowski and the Euclidean space, following from the properties and representations above:

$$a_E \cdot b_E = -a \cdot b, \quad \not{x}_E = i\not{x}, \quad (\partial \cdot a)_E = (\partial \cdot a), \quad \not{\partial}_E = -i\not{\partial}, \quad \square_E = -\square \quad (\text{A.29})$$

For the Dirac traces above we only have to exchange the Minkowski metric $g_{\mu\nu}$ by the Euclidean one $\delta_{\mu\nu}$. Furthermore we have to discuss the integral transformation. By using a Wick rotation we can transform the integral over the Minkowski time to an integral over the Euclidean time

$$\lim_{T \rightarrow \infty(1-i\epsilon)} i \int_{-T}^T dx_0 = \lim_{\tau \rightarrow \infty} \int_{-\tau}^{\tau} dx_4 \quad (\text{A.30})$$

where the infinitesimal variable ϵ is necessary because of the poles of the propagator. With these replacements rules in mind, we now can transform the generating functional in Minkowski space

into the Euclidean space, using the example of the fermionic action.

$$e^{iS} = \exp \left[i \int d^4x \bar{\Psi}(x) (i\not{\partial} - m) \Psi(x) \right] = \exp \left[- \int d^4x_E \bar{\Psi}(x_E) (\not{\partial}_E + m) \Psi(x_E) \right] = e^{-S_E} \quad (\text{A.31})$$

If we start from the Euclidean action, we perform all calculations in Euclidean space until the end where we arrive at Lorentz-invariant quantities. Those are for example the momentum dependent dressing functions of the Green-functions and Bethe-Salpeter amplitudes or observables such as masses. Thereby Lorentz-invariant scalar products only differ by minus signs in Minkowski and Euclidean conventions. Consequently we can transform trivially between Minkowski and Euclidean formulas.

A.1.4 Momentum space

Apart from the Minkowski and Euclidean space it is important to mention another space, the momentum space. Since all calculations are done in the momentum space, especially the DSE derivation and calculation, it is useful to give some rules to connect the normal space with the momentum space. To transform between both spaces, we use the Fourier transformation

$$\varphi(x) = \int \frac{d^4p}{(2\pi)^4} e^{-ipx} \varphi(p), \quad \varphi(p) = \int d^4x e^{ipx} \varphi(x) \quad (\text{A.32})$$

where φ stands for the quark spinor field $\Psi_{a,i}^f$ and the gluon vector field A_μ^g as well as the ghost field c_a . For the case of finite temperature we further have to consider equation (2.37) for the fourth component of the four momentum. We can transform the action and therefore the generating functional of a system into the momentum space using the following substitutions

$$\begin{aligned} \partial \cdot a &= \partial_\mu a^\mu \longrightarrow ip_\mu a^\mu = ip \cdot a, & \square &= \partial_\mu \partial^\mu \longrightarrow -p_\mu p^\mu = -p^2 \\ \Psi_{a,i}^f(x) &\longrightarrow \Psi_{a,i}^f(p), & A_\mu^g(x) &\longrightarrow A_\mu^g(k), & c_a(x) &\longrightarrow c_a(k) \end{aligned} \quad (\text{A.33})$$

In the last equation we indicated the Minkowski space by distinguishing co- and contravariant vectors, but the substitutions holds for the Euclidean space, too. Finally we can transform the fermionic action, mentioned before, as example:

$$e^{iS} = \exp \left[-i \int d^4p \bar{\Psi}(p) (\not{p} + m) \Psi(p) \right] = \exp \left[- \int d^4p_E \bar{\Psi}(p_E) (i\not{p}_E + m) \Psi(p_E) \right] = e^{-S_E} \quad (\text{A.34})$$

A.2 Color and flavor part

Next we will consider the color and flavor part of the wave-function. Therefore we have to mention the properties of the $SU_C(N_c)$ -group. In this work two possible representations of this group will be used, the fundamental one for the quark and the adjoint one for the gluon and the

f_{abc}	abc	d_{abc}	abc
1	123	$1/\sqrt{3}$	118, 228, 338
$1/2$	147, 246, 257, 345	$1/2$	146, 157, 256, 344, 355
$-1/2$	156, 367	$-1/2$	247, 366, 377
$\sqrt{3}/2$	458, 678	$-1/2\sqrt{3}$	448, 558, 668, 778
		$-1/\sqrt{3}$	888

Table A.1: Antisymmetric f_{abc} and symmetric d_{abc} structure constants for the color group $SU_C(3)$. The values for the remaining indices are obtained via permutation.

ghost. In both cases the group has $N_c^2 - 1$ hermitian traceless generators, which form the basis of a Lie algebra with the commutation relations

$$[t_a, t_b] = i f_{abc} t_c \quad (\text{A.35})$$

where f_{abc} are the totally anti-symmetric and real structure constants of $SU_C(N_c)$. Additionally the generators fulfill the relations

$$\text{tr}_c [t_a t_b] = T(R) \delta_{ab} \quad \text{and} \quad \left(\sum_{a=1}^{N_c^2-1} t_a^2 \right)_{ij} = C(R) \delta_{ij} \quad (\text{A.36})$$

where $T(R)$ is the Dynkin index and $C(R)$ the Casimir in the representation R . Before we specify the color number we discuss the possible representations separately:

- Fundamental representation: $T(R) = \frac{1}{2}$, $C(R) = \frac{N_c^2-1}{2N_c}$
- Adjoint representation: $T(R) = C(R) = N_c$

While the adjoint representation is given by $(t_a)_{bc} = -i f_{abc}$ and therefore by $(N_c^2 - 1) \times (N_c^2 - 1)$ -matrices, the fundamental representation is given by $N_c \times N_c$ -matrices which further satisfy the anticommutation relation

$$\{t_a, t_b\} = \frac{1}{N_c} \delta_{ab} + d_{abc} t_c \quad (\text{A.37})$$

with the totally symmetric and real structure constants d_{abc} . In nature we have three color flavors ($N_c = 3$), which yields for the structure constants the values given in the tabular A.1. Additionally in case of $SU_C(3)$ we can represent the generators of the fundamental representation by the 3×3 Gell-Mann matrices ($t_a = \frac{\lambda_a}{2}$)

$$\begin{aligned} \lambda_1 &= \begin{pmatrix} 0 & 1 & 0 \\ 1 & 0 & 0 \\ 0 & 0 & 0 \end{pmatrix} & \lambda_2 &= \begin{pmatrix} 0 & -i & 0 \\ i & 0 & 0 \\ 0 & 0 & 0 \end{pmatrix} & \lambda_3 &= \begin{pmatrix} 1 & 0 & 0 \\ 0 & -1 & 0 \\ 0 & 0 & 0 \end{pmatrix} & \lambda_4 &= \begin{pmatrix} 0 & 0 & 1 \\ 0 & 0 & 0 \\ 1 & 0 & 0 \end{pmatrix} \\ \lambda_5 &= \begin{pmatrix} 0 & 0 & -i \\ 0 & 0 & 0 \\ i & 0 & 0 \end{pmatrix} & \lambda_6 &= \begin{pmatrix} 0 & 0 & 0 \\ 0 & 0 & 1 \\ 0 & 1 & 0 \end{pmatrix} & \lambda_7 &= \begin{pmatrix} 0 & 0 & 0 \\ 0 & 0 & -i \\ 0 & i & 0 \end{pmatrix} & \lambda_8 &= \frac{1}{\sqrt{3}} \begin{pmatrix} 1 & 0 & 0 \\ 0 & 1 & 0 \\ 0 & 0 & -2 \end{pmatrix} \end{aligned} \quad (\text{A.38})$$

The flavor part of the quark and gluon propagator is diagonal and has not to be considered here, but for the case of the pseudoscalar mesons, we have a relevant flavor part. We only will consider mesons built by two equal quark flavors (up and down) in this work. These mesons are called pions or ρ -mesons, depending on their spin state and their flavor part can be represented by Pauli-matrices in the following way

$$\begin{aligned}
|\pi^+\rangle &= |ud^\dagger\rangle = \frac{1}{2}(\sigma_1 + i\sigma_2) \\
|\pi^-\rangle &= |du^\dagger\rangle = \frac{1}{2}(\sigma_1 - i\sigma_2) \\
|\pi^0\rangle &= \left| \frac{1}{\sqrt{2}}(uu^\dagger - dd^\dagger) \right\rangle = \frac{1}{\sqrt{2}}\sigma_3
\end{aligned} \tag{A.39}$$

with the shortcuts $u^\dagger = (1, 0)$ and $d^\dagger = (0, 1)$. The flavor-functions which enter the wave-function of the pion are therefore connected with the upper representations by $r^e = \sqrt{N_f} |\pi^e\rangle$ and fulfill the orthogonality relation

$$tr_f \left[(r^e)^\dagger r^{e'} \right] = N_f \delta_{ee'} \tag{A.40}$$

Appendix B

Projected equations

In this chapter we will derive and present the projected DSE'S and BSE's for the quark and gluon dressing functions as well as for the pion dressing functions for the truncations presented in this work. For this purpose, we derive the equations at first in general using only the truncation properties that the truncation schemes have in common.

B.1 Projected DSE's

Since we projected the DSE's already onto the tensor-structure to introduce the renormalization, we are left with the determination of the quark and gluon selfenergy only. To remember: We derived the projected quark DSE's in vacuum (2.67) and medium (2.68) by defining projected self-energies (2.63) and taking the Dirac trace A.1.2. The analog for the projected gluon DSE in vacuum is given in (3.16) and in medium by (3.20). Therefore we had to introduce the projected quark-loop's (3.17) and (3.19) as well as to use the gluon projector rules A.1.1. To recapitulate the connection of the renormalized quark-loop, see section 3.2.

In the following, we will derive these projected self-energies. At first we include the gluon tensor-structure ((2.46) or (2.47)) and further the gluon and vertex (3.7) truncations into the quark self-energy and the quark-loop (2.29). Doing so and comparing the color diagonal tensor-structure on both sides ($[t_a t_a]^{fund.} = C_F \mathbf{1} = \frac{N_c^2 - 1}{2N_c} \mathbf{1}$) in the quark DSE, but taking the color-trace ($tr_c [t_g t_h]^{adj.} = N_c \delta_{gh}$) in the quark-loop, we end up with the following self-energies in vacuum

$$\begin{aligned} \tilde{\Sigma}^f(p) &= C_F g^2 \int_q \gamma_\epsilon S^f(q) \gamma_\nu \Gamma_{BC}^f \Gamma(k^2) \frac{Z(k^2)}{k^2} P_{\epsilon\nu}^{\mathcal{T}}(k) \\ \Pi_{\epsilon\nu}^f(k) &= - \frac{g^2 Z_2^{f,vac}}{2} \int_q tr_D \left[\gamma_\epsilon S^f(q) \gamma_\nu S^f(p) \right] \Gamma_{BC}^f \Gamma(p^2 + q^2) \end{aligned} \quad (\text{B.1})$$

and in medium

$$\Pi_{\epsilon\nu}^f(k) = - \frac{g^2 Z_2^{f,vac}}{2} \sum_q tr_D \left[\gamma_\epsilon S^f(q) \gamma_\nu S^f(p) \right] \left(\Gamma_s^f \delta_{\nu s} + \Gamma_4^f \delta_{\nu 4} \right) \Gamma(p^2 + q^2)$$

$$\begin{aligned} \tilde{\Sigma}^f(p) = & C_F g^2 \sum_q \gamma_\epsilon S^f(q) \gamma_\nu \left(\Gamma_s^f \delta_{\nu s} + \Gamma_4^f \delta_{\nu 4} \right) \Gamma(k^2) \left[\frac{Z_L(\vec{k}^2, \omega_k)}{k^2} P_{e\nu}^L(k) + \right. \\ & \left. + \frac{Z_T(\vec{k}^2, \omega_k)}{k^2} P_{e\nu}^T(k) \right] \end{aligned} \quad (\text{B.2})$$

where we used the argument $p^2 + q^2$ in Γ for the case of the quark-loop because of multiplicative renormalizability. Since the ghost-gluon-vertex is not ultraviolet divergent in Landau gauge we were able to set $\tilde{Z}_1 = 1$. With these equations in mind, we can derive the already mentioned and introduced projected quark and gluon self-energies. To highlight different aspects of interest we will discuss the vacuum and in-medium case separately.

B.1.1 Vacuum

To calculate the projected quark and gluon self-energies, it remains only to insert the quark tensor-structure (2.45) into the truncated quark and gluon self-energies (B.1) and to calculate the traces presented in (2.63) and (3.17). The result is

$$\begin{aligned} \tilde{\Sigma}_A^f(p) &= \frac{4\pi C_F \alpha(\mu'')}{p^2} \int_q^\Lambda \frac{A^f(q^2) \Gamma_{BC}^f}{D^f(q^2)} K_{AA} \\ \tilde{\Sigma}_B^f(p) &= 12\pi C_F \alpha(\mu'') \int_q^\Lambda \frac{B^f(q^2) \Gamma_{BC}^f}{D^f(q^2)} K_{BB} \end{aligned} \quad (\text{B.3})$$

for the quark self-energy and

$$\Pi_{vac}^{reg}(k) = -\frac{8\pi\alpha(\mu'')}{3k^2} \sum_f^{N_f} Z_2^{f,vac} \int_q^\Lambda \frac{A^f(q^2)}{D^f(q^2)} \frac{A^f(p^2)}{D^f(p^2)} \Gamma(p^2 + q^2) \Gamma_{BC}^f \left[8 \frac{(kp)(kq)}{k^2} - 2pq \right] \quad (\text{B.4})$$

for the gluon quark-loop. The angular kernels given in the quark self-energy are thereby defined by

$$\begin{aligned} K_{AA} &= \frac{\Gamma(k^2) Z(k^2)}{k^2} \left(-k^2 + \frac{p^2 + q^2}{2} + \frac{(p^2 - q^2)^2}{2k^2} \right) \\ K_{BB} &= \frac{\Gamma(k^2) Z(k^2)}{k^2} \end{aligned} \quad (\text{B.5})$$

In both self-energies we used the shortcut $D^f(q^2) = q^2 A_f^2(q^2) + B_f^2(q^2)$ and the internal quark momentum q^2 . For the quark self-energy we utilized the momentum routing $k_\mu = q_\mu - p_\mu$ and for the quark-loop $p_\mu = q_\mu - k_\mu$. The running coupling $\alpha(\mu'')$ at a choosen scale μ'' is given by $\alpha(\mu'') = \frac{g^2}{4\pi} = 0.3$. For more details of the numerical solution of this coupled system of integral equations see Appendix C.

B.1.2 Finite temperature

Like in the vacuum case we insert the quark tensor-structure (2.44) into the truncated quark and gluon self-energy (B.2), yielding the following projected self-energies

$$\begin{aligned}
 \tilde{\Sigma}_A^f(p) &= \frac{4\pi C_F \alpha(\mu'')}{\bar{p}^2} \sum_q^{\Lambda_f} \frac{1}{D^f(\vec{q}^2, \omega_q)} \left[A^f(\vec{q}^2, \omega_q) \left(\Gamma_s^f K_{AAS} + \Gamma_4^f K_{AA4} \right) + \right. \\
 &\quad \left. + C^f(\vec{q}^2, \omega_q) \tilde{\omega}_q \left(\Gamma_s^f + \Gamma_4^f \right) K_{AC} \right] \\
 \tilde{\Sigma}_B^f(p) &= 4\pi C_F \alpha(\mu'') \sum_q^{\Lambda_f} \frac{1}{D^f(\vec{q}^2, \omega_q)} \left[B^f(\vec{q}^2, \omega_q) \left(\Gamma_s^f K_{BBS} + \Gamma_4^f K_{BB4} \right) \right] \\
 \tilde{\Sigma}_C^f(p) &= \frac{4\pi C_F \alpha(\mu'')}{\tilde{\omega}_p} \sum_q^{\Lambda_f} \frac{1}{D^f(\vec{q}^2, \omega_q)} \left[A^f(\vec{q}^2, \omega_q) \left(\Gamma_s^f + \Gamma_4^f \right) K_{CA} + \right. \\
 &\quad \left. + C^f(\vec{q}^2, \omega_q) \tilde{\omega}_q \left(\Gamma_s^f K_{CCS} + \Gamma_4^f K_{CC4} \right) \right]
 \end{aligned} \tag{B.6}$$

for the quark, after taking traces of the form (2.63). The angular kernels in the quark self-energy are therefore defined by

$$\begin{aligned}
 K_{AAS} &= \left[\frac{Z_L(\vec{k}^2, \omega_k)}{k^2} \frac{\omega_k^2}{k^2} \left(\vec{p}\vec{q} - 2 \frac{(\vec{p}\vec{k})(\vec{q}\vec{k})}{k^2} \right) + 2 \frac{Z_T(\vec{k}^2, \omega_k)}{k^2} \frac{(\vec{p}\vec{k})(\vec{q}\vec{k})}{k^2} \right] \Gamma(k^2) \\
 K_{AA4} &= \frac{Z_L(\vec{k}^2, \omega_k)}{k^2} \frac{\vec{k}^2}{k^2} \vec{p}\vec{q} \Gamma(k^2) \quad , \quad K_{BB4} = -K_{CC4} = \frac{Z_L(\vec{k}^2, \omega_k)}{k^2} \frac{\vec{k}^2}{k^2} \Gamma(k^2) \\
 K_{AC} &= \frac{Z_L(\vec{k}^2, \omega_k)}{k^2} \frac{(\vec{p}\vec{k})\omega_k}{k^2} \Gamma(k^2) \quad , \quad K_{CA} = \frac{Z_L(\vec{k}^2, \omega_k)}{k^2} \frac{(\vec{q}\vec{k})\omega_k}{k^2} \Gamma(k^2) \\
 K_{BBS} &= K_{CCS} = \left[2 \frac{Z_T(\vec{k}^2, \omega_k)}{k^2} + \frac{Z_L(\vec{k}^2, \omega_k)}{k^2} \frac{\omega_k^2}{k^2} \right] \Gamma(k^2)
 \end{aligned} \tag{B.7}$$

In the quark and the following gluon self-energies the shortcut $D^f(\vec{q}^2, \omega_q) = \vec{q}^2 A_f^2(\vec{q}^2, \omega_q) + \tilde{\omega}_q^2 C_f^2(\vec{q}^2, \omega_q) + B_f^2(\vec{q}^2, \omega_q)$ is used and the running coupling $\alpha(\mu'')$ is defined like in the vacuum case before. To reduce the numerical effort and since the restoration of O(4)-invariance is already given for the zeroth Matsubara frequency in case of the gluon, the following ‘‘zeroth Matsubara frequency approximation’’ is introduced for the gluon dressing functions

$$Z_{T/L}(\vec{k}^2, \omega_k) \approx Z_{T/L}(\vec{k}^2 + \omega_k^2, 0) \tag{B.8}$$

This reduces the necessary transversal and longitudinal parts of the quark-loop to the following equations and is used throughout the work.

$$\begin{aligned}
 \Pi_T^{reg}(\vec{k}^2, 0) &= - \frac{8\pi\alpha(\mu'')}{\vec{k}^2} \sum_f^{N_f} Z_2^{f,vac} \sum_q^{\Lambda_f} \frac{\Gamma(p^2 + q^2)}{D^f(\vec{q}^2, \omega_q) D^f(\vec{p}^2, \omega_p)} \left(3 \frac{(\vec{p}\vec{k})(\vec{q}\vec{k})}{k^2} - \vec{p}\vec{q} \right) \\
 &\quad \cdot A^f(\vec{q}^2, \omega_q) A^f(\vec{p}^2, \omega_p) \Gamma_s^f
 \end{aligned}$$

$$\begin{aligned}
 \Pi_L^{reg}(\vec{k}^2, 0) = & -\frac{8\pi\alpha(\mu'')}{\vec{k}^2} \sum_f^{N_f} Z_2^{f,vac} \sum_q^{\Lambda_r} \frac{\Gamma(p^2 + q^2)}{D^f(\vec{q}^2, \omega_q) D^f(\vec{p}^2, \omega_p)} \cdot \\
 & \cdot \left\{ A^f(\vec{q}^2, \omega_q) A^f(\vec{p}^2, \omega_p) \left[\Gamma_s^f \left(2 \frac{(\vec{p}\vec{k})(\vec{q}\vec{k})}{\vec{k}^2} - \vec{p}\vec{q} \right) + \Gamma_4^f \vec{p}\vec{q} \right] - \right. \\
 & \left. - C^f(\vec{q}^2, \omega_q) C^f(\vec{p}^2, \omega_p) \tilde{\omega}_p \tilde{\omega}_q (\Gamma_s^f + \Gamma_4^f) + B^f(\vec{q}^2, \omega_q) B^f(\vec{p}^2, \omega_p) (\Gamma_4^f - \Gamma_s^f) \right\} \quad (\text{B.9})
 \end{aligned}$$

As already mentioned in section 3.2 we split the quark-loop into a divergence free part (regular part) (3.23) and a thermal mass (3.22), which we calculate with higher accuracy. After expressing the quark-loop with the quark dressing functions, we can give explicit equations for the thermal masses. These equations are given by

$$\begin{aligned}
 (m_{th}^T)^2(T, \mu_q) = & 0 \\
 (m_{th}^L)^2(T, \mu_q) = & -\frac{2\alpha(\mu'')}{\pi} \sum_f^{N_f} Z_2^{f,vac} \sum_{R,q}^{\Lambda_r} \frac{\Gamma(2q^2)}{D_f^2(\vec{q}^2, \omega_q)} \{ A_f^2(\vec{q}^2, \omega_q) \vec{q}^2 \cdot \\
 & \cdot \left[C^f(\vec{q}^2, \omega_q) - \frac{1}{3} A^f(\vec{q}^2, \omega_q) \right] - C_f^2(\vec{q}^2, \omega_q) \tilde{\omega}_q^2 \left[A^f(\vec{q}^2, \omega_q) + C^f(\vec{q}^2, \omega_q) \right] + \\
 & + B_f^2(\vec{q}^2, \omega_q) \left[C^f(\vec{q}^2, \omega_q) - A^f(\vec{q}^2, \omega_q) \right] \} \quad (\text{B.10})
 \end{aligned}$$

where $\int_{R,q}^{\Lambda}$ represents the radial part of the integral only and is defined in Appendix C. The regular part of the quark-loop, on the other hand, is simply determined by subtracting the divergence, which resulting from the thermal mass. For this purpose, it is important to apply the same precision for the thermal mass. In contrast, we add a more precise thermal mass term to the regular part, to get back the regularized quark-loop. In this way we can extract the thermal mass with an high accuracy. For more details to the thermal mass, the approximation used in this section, the regulator definition and the numerical solution in general see Appendix C.

B.1.3 Cold dense matter

For the cold dense matter case, we only considered the quark propagator until now. For this purpose, we adopt the projected quark DSE's from the medium case and exchange the discreet Matsubara frequencies by the continuous fourth momentum component ($\omega_x(T) \rightarrow x_4$). Additionally we integrate over the fourth momentum component instead of summing the discreet Matsubara frequencies ($\int_q^{\Lambda} \rightarrow \int_q^{\Lambda}$). Because we are calculating only the quark, without back-coupling it onto the gluon, we can set the transversal and longitudinal (in the sense of the fourth momentum component) gluon dressing function to the vacuum gluon dressing function $Z_{T/L}(\vec{k}^2, k_4) = Z(k^2)$. The reason for this is that only unquenching effects (thermal mass) produce a difference between these two dressing functions. Considering the mentioned variations,

yields the following quark self-energies

$$\begin{aligned}
 \tilde{\Sigma}_A^f(p) &= \frac{4\pi C_F \alpha(\mu'')}{\bar{p}^2} \int_q^\Lambda \frac{1}{D^f(\bar{q}^2, q_4)} \left[A^f(\bar{q}^2, q_4) \left(\Gamma_s^f K_{AAS} + \Gamma_4^f K_{AA4} \right) + \right. \\
 &\quad \left. + C^f(\bar{q}^2, q_4) \tilde{q}_4 \left(\Gamma_s^f + \Gamma_4^f \right) K_{AC} \right] \\
 \tilde{\Sigma}_B^f(p) &= 4\pi C_F \alpha(\mu'') \int_q^\Lambda \frac{1}{D^f(\bar{q}^2, q_4)} \left[B^f(\bar{q}^2, q_4) \left(\Gamma_s^f K_{BBS} + \Gamma_4^f K_{BB4} \right) \right] \\
 \tilde{\Sigma}_C^f(p) &= \frac{4\pi C_F \alpha(\mu'')}{\tilde{p}_4} \int_q^\Lambda \frac{1}{D^f(\bar{q}^2, q_4)} \left[A^f(\bar{q}^2, q_4) \left(\Gamma_s^f + \Gamma_4^f \right) K_{CA} + \right. \\
 &\quad \left. + C^f(\bar{q}^2, q_4) \tilde{q}_4 \left(\Gamma_s^f K_{CCS} + \Gamma_4^f K_{CC4} \right) \right] \tag{B.11}
 \end{aligned}$$

with the related angular kernels

$$\begin{aligned}
 K_{AAS} &= \frac{Z(k^2)}{k^2} \left[\tilde{p}\vec{q} \frac{k_4^2}{k^2} + 2 \frac{(\tilde{p}\vec{k})(\vec{q}\vec{k})}{k^2} \right] \Gamma(k^2) \quad , \quad K_{AA4} = \frac{Z(k^2)}{k^2} \frac{\vec{k}^2}{k^2} \tilde{p}\vec{q} \Gamma(k^2) \\
 K_{AC} &= \frac{Z(k^2)}{k^2} \frac{(\tilde{p}\vec{k})k_4}{k^2} \Gamma(k^2) \quad , \quad K_{CA} = \frac{Z(k^2)}{k^2} \frac{(\vec{q}\vec{k})k_4}{k^2} \Gamma(k^2) \\
 K_{BBS} = K_{CCS} &= \frac{Z(k^2)}{k^2} \left[2 + \frac{k_4^2}{k^2} \right] \Gamma(k^2) \quad , \quad K_{BB4} = -K_{CC4} = \frac{Z(k^2)}{k^2} \frac{\vec{k}^2}{k^2} \Gamma(k^2) \tag{B.12}
 \end{aligned}$$

If we further neglect the first Ball-Chiu terms $\Gamma_s = \Gamma_s = Z_2$, the quark self-energy simplifies to

$$\begin{aligned}
 \tilde{\Sigma}_A^f(p) &= \frac{4\pi Z_2 C_F \alpha(\mu'')}{\bar{p}^2} \int_q^\Lambda \frac{A^f(\bar{q}^2, q_4) K_{AA} + C^f(\bar{q}^2, q_4) \tilde{q}_4 K_{AC}}{D^f(\bar{q}^2, q_4)} \\
 \tilde{\Sigma}_B^f(p) &= 4\pi Z_2 C_F \alpha(\mu'') \int_q^\Lambda \frac{B^f(\bar{q}^2, q_4) K_{BB}}{D^f(\bar{q}^2, q_4)} \\
 \tilde{\Sigma}_C^f(p) &= \frac{4\pi Z_2 C_F \alpha(\mu'')}{\tilde{p}_4} \int_q^\Lambda \frac{A^f(\bar{q}^2, q_4) K_{CA} + C^f(\bar{q}^2, q_4) \tilde{q}_4 K_{CC}}{D^f(\bar{q}^2, q_4)} \tag{B.13}
 \end{aligned}$$

with the angular kernels

$$\begin{aligned}
 K_{AA} &= \frac{Z(k^2)}{k^2} \left[\tilde{p}\vec{q} + 2 \frac{(\tilde{p}\vec{k})(\vec{q}\vec{k})}{k^2} \right] \Gamma(k^2) \quad , \quad K_{AC} = 2 \frac{Z(k^2)}{k^2} \frac{(\tilde{p}\vec{k})k_4}{k^2} \Gamma(k^2) \\
 K_{BB} &= 3 \frac{Z(k^2)}{k^2} \Gamma(k^2) \\
 K_{CC} &= 2 \frac{Z(k^2)}{k^2} \left[1 - \frac{\vec{k}^2}{k^2} \right] \Gamma(k^2) \quad , \quad K_{CA} = 2 \frac{Z(k^2)}{k^2} \frac{(\vec{q}\vec{k})k_4}{k^2} \Gamma(k^2) \tag{B.14}
 \end{aligned}$$

A detailed description of the treatment of the integrals is given in Appendix C.

Quenched QCD with Maris-Tandy model: In this truncation we do not calculate the gluon and introduce an effective interaction instead. For this purpose, we have to exchange the following equations in relation (B.5), (B.7) and (B.12). In section 4.1 the possible ansätze for Ω

are presented.

$$\begin{aligned}\Omega(k^2) &= \alpha(\mu'')\Gamma(k^2)\frac{Z(k^2)}{k^2} \\ \Omega_{L/T}(\vec{k}^2, \omega_k) &= \alpha(\mu'')\Gamma(k^2)\frac{Z_{L/T}(\vec{k}^2, \omega_k)}{k^2}\end{aligned}\quad (\text{B.15})$$

B.2 Projected BSE's

Similar to the quark and gluon propagators, we want to derive projected BSE's for the pseudoscalar mesons, more precisely the pions, in this section. For this purpose, we will use the decomposition (2.104) first and project onto the dressing functions and afterwards we will expand the dressing functions with Chebyshev polynomials (2.105). The first step to get the BSE's for the dressing functions is to define appropriate projectors $T_X^\pi(P, p)$ ($X(P, p) = \text{tr}_D [T_X^\pi(P, p)\Gamma_\pi(P, p)]$) for the Dirac tensor-structure of the pions

$$\Gamma_\pi(P, p) = \gamma_5 [-iE(P, p) + \not{P}F(P, p) + \not{p}G(P, p) + [\not{P}, \not{p}]H(P, p)] \quad (\text{B.16})$$

after having removed the flavor and color dependency, by taking the trace or comparing the structure with the relations given in Appendix A.2. The mentioned projectors are given by

$$\begin{aligned}T_E^\pi(P, p) &= \frac{i}{4}\gamma_5, & T_F^\pi(P, p) &= \frac{p^2\not{P} - \not{p}(pP)}{4(p^2P^2 - (pP)^2)}\gamma_5, \\ T_G^\pi(P, p) &= \frac{P^2\not{p} - \not{P}(pP)}{4(P^2p^2 - (pP)^2)}\gamma_5, & T_H^\pi(P, p) &= \frac{[\not{P}, \not{p}]}{16(P^2p^2 - (pP)^2)}\gamma_5\end{aligned}\quad (\text{B.17})$$

In fact only the first pion dressing function $E(p, P)$ will be considered in this work. Therefore we restrict ourselves to the projected BSE's of the first pion dressing function in vacuum and the cold dense matter case, which are given by

$$E(p, P) = 12\pi C_F \left(Z_2^{f, vac} \right)^2 \int_q^\Lambda \frac{\alpha(k^2)}{k^2} K_{EE}(q_+, q_-) E(q, P) \quad (\text{B.18})$$

with the kernels and denominators

$$K_{EE}(q_+, q_-) = \frac{B(q_-^2)B(q_+^2) - q_+q_-A(q_-^2)A(q_+^2)}{D(q_-^2)D(q_+^2)}, \quad D(q^2) = q^2A^2(q^2) + B^2(q^2) \quad (\text{B.19})$$

for the vacuum and

$$\begin{aligned}K_{EE}(q_+, q_-) &= \left[\frac{B(\vec{q}_-^2, -q_{4-})B(\vec{q}_+^2, q_{4+})}{D(\vec{q}_-^2, -q_{4-})D(\vec{q}_+^2, q_{4+})} + \right. \\ &\quad \left. - \frac{\vec{q}_+\vec{q}_-A(\vec{q}_-^2, -q_{4-})A(\vec{q}_+^2, q_{4+}) + \tilde{q}_{4+}\tilde{q}_{4-}C(\vec{q}_-^2, -q_{4-})C(\vec{q}_+^2, q_{4+})}{D(\vec{q}_-^2, -q_{4-})D(\vec{q}_+^2, q_{4+})} \right] \\ D(\vec{q}^2, q_4) &= \vec{q}^2A^2(\vec{q}^2, q_4) + \tilde{q}_4^2C^2(\vec{q}^2, q_4) + B^2(\vec{q}^2, q_4)\end{aligned}\quad (\text{B.20})$$

for the cold dense matter case. To get these equations we projected the rhs of equation (2.91) onto the first pion dressing function and inserted the kernel (2.87) for an (at first) arbitrary coupling $\alpha(k^2)$. Later on we will set the coupling to one of the fit functions of the quenched chapter. Furthermore it is important to parameterize the occurring momenta. For this purpose, we have three options: we can either use the total momentum parameterization $P = (\vec{0}, im_\pi)$ or $P = (0, 0, im_\pi, 0)$ or a combination of both. If we use the first parameterization the quark momenta are given by

$$p = (|\vec{p}|(0, 0, 1), p_4) \quad q = (|\vec{q}|(0, \sin(\Psi_q), \cos(\Psi_q)), q_4) \quad (\text{B.21})$$

with \vec{p} , p_4 and the analogs of q given by (C.9). This parameterization yields an integral representation given by

$$\int_q^\Lambda = \frac{1}{8\pi^3} \int_{R,q}^\Lambda \int_0^\pi d\Psi_q \sin(\Psi_q) \int_0^\pi d\theta_q \sin^2(\theta_q) = \frac{1}{8\pi^3} \int_{R,q}^\Lambda \int_{-1}^1 dy_q \int_{-1}^1 dz_q \sqrt{1-z_q^2} \quad (\text{B.22})$$

with $z_q = \cos(\theta_q)$ and $y_q = \cos(\Psi_q)$. The problem, however, is that with this parameterization we are only able to calculate the temporal decay constant f_π^t , as we will see later on. In the second parameterization the quark momenta and the integral representation are given by

$$\begin{aligned} p &= (|\vec{p}|(0, \sin(\Psi_p), \cos(\Psi_p)), p_4) \\ q &= (|\vec{q}|(\sin(\Psi_q) \sin(\varphi_q), \sin(\Psi_q) \cos(\varphi_q), \cos(\Psi_q)), q_4) \\ \int_q^\Lambda &= \frac{1}{16\pi^4} \int_{R,q}^\Lambda \int_0^{2\pi} d\varphi_q \int_0^\pi d\Psi_q \sin(\Psi_q) \int_0^\pi d\theta_q \sin^2(\theta_q) \\ &= \frac{1}{16\pi^4} \int_{R,q}^\Lambda \int_0^{2\pi} d\varphi_q \int_{-1}^1 dy_q \int_{-1}^1 dz_q \sqrt{1-z_q^2} \end{aligned} \quad (\text{B.23})$$

where \vec{p} and p_4 as well as the analogs of q again are given by (C.9). With this parameterization we also have the problem, that we only can calculate one of the pion decay constants, but in this case the spacial part f_π^s . To obtain both parts of the decay constant and therefore the velocity of the bound-state in medium, we have to use the third parameterization. But due to the complexity of this parameterization, we restrict ourselves to the first parameterization for the first results. For this case we already mentioned, that the argument of the pion can be parameterized by three lorentz-invariants P^2 , p^2 and z_p . The only difference between the vacuum and the cold dense matter case is, that the quark propagator has a richer tensor-structure and depends itself on the angle z_p , if we consider the cold dense matter case. Consequently we only have to consider equation (B.18), if we want to derive the projected BSE's for the Chebyshev components of the first pion dressing function. By applying $\frac{2}{N} \sum_{n=0}^{N-1} \tilde{T}_j(z_n^p)(i)^{-j}$ onto the BSE of the first pion dressing function and expressing the internal pion dressing function by (2.105),

we get the final BSE for the Chebyshev coefficients of the first pion dressing function

$$\tilde{E}_j(p^2, P^2) = \frac{24\pi}{N} C_F \left(Z_2^{f,vac} \right)^2 \sum_{n=0}^{N-1} \tilde{T}_j(z_n^p) \int_q^\Lambda \frac{\alpha(k^2)}{k^2} K_{EE}(q_+, q_-) \sum_{l=0}^{\tilde{N}} \tilde{E}_l(q^2, P^2) \tilde{T}_l(z_q) (i)^{l-j} \quad (\text{B.24})$$

where \tilde{E} corresponds to the modified Chebyshev polynomials and is connected to E by $\tilde{E}_j(P^2, p^2) = \left(\frac{1}{\sqrt{2}} \delta_{j,0} + (1 - \delta_{j,0}) \right) E_j(P^2, p^2)$. The discussion how the BSE is numerically calculated is shifted to the Appendix C.5.

B.2.1 Meson amplitude normalization

Since the meson amplitude, calculated with the equation above, is not fixed in its scale, we have to include the normalization of the meson amplitude given in equation (2.98). Like in the BSE equation, we will include the decomposition (2.104) first, before including the Chebyshev expansion (2.105). Taking the traces, after including the first decomposition, yields

$$\mathcal{N}^2 = 24 \frac{\partial}{\partial P^2} \int_q^\Lambda K_{EE}(q_+, q_-) E(q, -P_i) E(q, P_i) \Big|_{P=P_i} \quad (\text{B.25})$$

where $K_{EE}(q_+, q_-)$ is defined by (B.19) in vacuum or (B.20) in the cold dense matter case. It is noteworthy, that we included the kernel given in (2.87), which is independent from the total momentum P and used the first momentum parameterization mentioned before to express $\frac{(P_i)_\mu}{2P_i^2} \frac{\partial}{\partial P_\mu} \Big|_{P=P_i} = \frac{\partial}{\partial P^2} \Big|_{P=P_i}$. Finally we include the Chebyshev expansion (2.105), with the result:

$$\mathcal{N}^2 = 24 \frac{\partial}{\partial P^2} \left(\int_q^\Lambda K_{EE}(q_+, q_-) \sum_{j,k=0}^{\tilde{N}} \tilde{E}_j(q^2, P_i^2) \tilde{T}_j(-z_q) \tilde{E}_k(q^2, P_i^2) \tilde{T}_k(-z_q) \right) \Big|_{P=P_i} \quad (\text{B.26})$$

We will use the difference quotient approximation $\frac{\partial f(P^2)}{\partial P^2} = \frac{f(P^2(1+\epsilon)) - f(P^2(1-\epsilon))}{2P^2\epsilon}$ with a small parameter ϵ for the derivative $\frac{\partial f(P^2)}{\partial P^2}$.

B.2.2 Meson decay constant

For the meson decay constant we have to distinguish between the vacuum (2.114) and the cold dense matter case (2.117). Again, we will calculate the traces by including the decomposition of the pion Bethe-Salpeter amplitude (2.104) and the quark propagator as well as the Chebyshev expansion (2.105). The results are

$$f_\pi = -\frac{12Z_2^{f,vac}}{P^2} \int_q^\Lambda \sum_{k=0}^{\tilde{N}} \tilde{E}_k(q^2, P^2) \tilde{T}_k(z_q) \frac{B(q_-^2)A(q_+^2)Pq_+ + A(q_-^2)B(q_+^2)Pq_-}{D(q_-^2)D(q_+^2)} \quad (\text{B.27})$$

for the vacuum and

$$\begin{aligned}
 -f_\pi^t &= \frac{3Z_2^{f,vac}}{(Pv)} \int_q^\Lambda \text{tr}_D [\gamma_5 \psi S(q_+) \Gamma_\pi(p, P) S(-q_-)] = \frac{12Z_2^{f,vac}}{P^2} \int_q^\Lambda \sum_{k=0}^{\tilde{N}} \tilde{E}_k(q^2, P^2) \tilde{T}_k(z_q) \cdot \\
 &\quad \cdot \frac{B(\vec{q}_-^2, q_{4-}) C(\vec{q}_+^2, q_{4+}) P_4 \tilde{q}_{4+} + C(\vec{q}_-^2, q_{4-}) B(\vec{q}_+^2, q_{4+}) P_4 \tilde{q}_{4-}}{D(\vec{q}_-^2, q_{4-}) D(\vec{q}_+^2, q_{4+})} \\
 |\bar{P}|=0 &\frac{12Z_2^{f,vac}}{P} \int_q^\Lambda \sum_{k=0}^{\tilde{N}} \tilde{E}_k(q^2, P^2) \tilde{T}_k(z_q) \frac{B(\vec{q}^2, q_{4-}) C(\vec{q}^2, q_{4+}) \tilde{q}_{4+} + C(\vec{q}^2, q_{4-}) B(\vec{q}^2, q_{4+}) \tilde{q}_{4-}}{D(\vec{q}^2, q_{4-}) D(\vec{q}^2, q_{4+})} \\
 -f_\pi^s &= \frac{3Z_2^{f,vac}}{P^2 - (Pv)^2} \int_q^\Lambda \text{tr}_D [\gamma_5 (\not{P} - (Pv)\not{v}) S(q_+) \Gamma_\pi(p, P) S(-q_-)] = \frac{12Z_2^{f,vac}}{P^2} \int_q^\Lambda \sum_{k=0}^{\tilde{N}} \cdot \\
 &\quad \cdot \tilde{E}_k(q^2, P^2) \tilde{T}_k(z_q) \frac{B(\vec{q}_-^2, q_{4-}) A(\vec{q}_+^2, q_{4+}) \vec{P} \vec{q}_+ + A(\vec{q}_-^2, q_{4-}) B(\vec{q}_+^2, q_{4+}) \vec{P} \vec{q}_-}{D(\vec{q}_-^2, q_{4-}) D(\vec{q}_+^2, q_{4+})} \Big|_{\bar{P}=0} 0 \quad (\text{B.28})
 \end{aligned}$$

for the cold dense matter case. In these equations we use the momentum integral shortcuts given in equation (C.4). For the latter case we had to project onto the two decay constants, by multiplying with $P_{\mu\nu}^{\mathcal{F}}(v)$ and $P_{\mu\nu}^{\mathcal{L}}(v)$ and taking the trace with respect to the Lorenz indices. For the calculation of the Bethe-Salpeter amplitude and the its normalization as well as the pion decay constant, we have to use quarks with complex momenta as input. The discussion of the calculation of the quark propagator in the complex plane is done in section 4.3.

Appendix C

Numerical details

In this Appendix we will discuss the numerical side of this work, beginning with the necessary momentum integral transformations and afterwards the numerical treatment of the same. Then we will continue with aspects of the thermal mass calculation and the renormalization and further with order parameters and phase diagram calculations. We conclude with the numerical details to the pion calculation.

C.1 Momentum integrals in vacuum and medium

At first we include hyperspherical coordinates

$$\int d^4q f(q) = \frac{1}{2} \int_0^\infty dq^2 q^2 \int_0^{2\pi} d\phi_q \int_0^\pi d\Psi_q \sin(\Psi_q) \int_0^\pi d\theta_q \sin^2(\theta_q) f(q^2, \phi_q, \Psi_q, \theta_q) \quad (\text{C.1})$$

into the four-dimensional integral $\int_q = \int \frac{d^4q}{(2\pi)^4}$ of the vacuum and the cold dense matter case and the corresponding spherical coordinates

$$\int d^3|\vec{q}| f(\omega_q, \vec{q}) = \frac{1}{2} \int_0^\infty d|\vec{q}|^2 |\vec{q}| \int_0^{2\pi} d\phi_q \int_0^\pi d\Psi_q \sin(\Psi_q) f(\omega_q, |\vec{q}|, \phi_q, \Psi_q) \quad (\text{C.2})$$

into the three-dimensional integral $\int_q = T \sum_{n_q} \int \frac{d^3|\vec{q}|}{(2\pi)^3}$ for finite temperatures. This yields the following equations

$$\begin{aligned} \int_q &= \int \frac{d^4q}{(2\pi)^4} = \int_0^\infty dq^2 \frac{q^2}{2} \int d\Omega_{4D} \\ \int_q &= T \sum_{n_q} \int \frac{d^3|\vec{q}|}{(2\pi)^3} = T \sum_{n_q} \int_0^\infty d|\vec{q}|^2 \frac{|\vec{q}|}{2} \int d\Omega_{3D} \end{aligned} \quad (\text{C.3})$$

which we have to regularize by introducing an UV hard O(4) momentum cutoff Λ .

$$\int_q^\Lambda = \int_{\epsilon^2}^{\Lambda^2} dq^2 \frac{q^2}{2} \int d\Omega_{4D} = \int_{R,q}^\Lambda \int d\Omega_{4D}$$

$$\sum_q^{\Lambda'} = T \sum_{n_q}^{|\omega_q| < \Lambda'} \int_{\epsilon^2}^{\vec{\Lambda}_{n_q}^2} d|\vec{q}|^2 \frac{|\vec{q}|}{2} \int d\Omega_{3D} = \sum_{R,q}^{\Lambda'} \int d\Omega_{3D} \quad (\text{C.4})$$

where the index R states, that the related integral symbol concerns only the radial part of the integration. Further, the three-dimensional momentum cutoff of the spacial part is given by $\vec{\Lambda}_{n_q}^2 = \Lambda'^2 - \omega_q^2(n_q)$ with the Matsubara frequency $\omega_q(n_q)$. In case of the quark self-energy, Λ' coincides with the UV hard $O(4)$ momentum cutoff Λ . For the quark-loop calculation, in contrast, we use a temperature dependent cutoff $\Lambda' = \pi T(2N + 2)$ with $N := \{\max(n) \in \mathbb{N} : \pi T(2n + 2) < \Lambda\}$, which represents the last Matsubara frequency below the actual UV hard $O(4)$ momentum cutoff Λ . We have to be mentioned, that this choice for the cutoff could be related to a problem of shaking quark condensate values near the pseudo-critical temperature for the crossover region. In following works this subject has to be investigated, but it is kept for the sake of comparison with previous works.

An additional point of concern is the treatment of the Matsubara sum. Here we have to distinguish between the quark self-energy and the quark-loop calculation. While we compute the whole sum explicitly for the quark-loop, this would slow down the program significantly in case of the quark self-energy. Since the quark-loop itself does not depend on the gluon the quark-loop has to be calculated only once for a fixed quark. The quark self-energy, by contrast, has to be iterated for a fixed gluon. Consequently the explicit sum for the quark-loop is numerically bearable and also necessary, but for the quark self-energy Matsubara sum the following integral approximation is introduced.

$$T \sum_{n_q}^{|\omega_q| < \Lambda'} f(\omega_q) = T \int_{-(\frac{\Lambda'}{2\pi T} - \frac{1}{2})}^{-N} dn_q f(\omega_q) + T \sum_{n_q=-N}^{N-1} f(\omega_q) + T \int_{N-1}^{\frac{\Lambda'}{2\pi T} - \frac{1}{2}} dn_q f(\omega_q) \quad (\text{C.5})$$

As we can see, the number of explicit Matsubara frequencies is reduced to $2N$ summands. Since the Matsubara frequencies above the given Matsubara-indices are only approximated, it seems natural that higher N values are needed for good results at lower temperature. The reason is that the momentum range which is covered by the explicit Matsubara sum decrease for decreasing temperatures and fixed N . Consequently we have to describe more and more parts of the dressing functions with an approximation. With the substitution $\omega_q = \pi T(2n_q - 1)$, $d\omega_q = 2\pi T dn_q$ we further can transform both integrals to the Matsubara frequencies.

$$T \sum_{n_q}^{|\omega_q| < \Lambda'} f(\omega_q) = \frac{1}{2\pi} \int_{-\Lambda'}^{\pi T(2(-N)+1)} d\omega_q f(\omega_q) + T \sum_{n_q=-N}^{N-1} f(\omega_q) + \frac{1}{2\pi} \int_{\pi T(2(N-1)+1)}^{\Lambda'} d\omega_q f(\omega_q) \quad (\text{C.6})$$

Since the integration in the self-energy and the quark-loop is defined over fermionic quark momenta we have to take fermionic Matsubara frequencies in the substitution. Further noteworthy is the integral representation in the case of cold dense matter. If we follow the final

lines of section 2.1.2, the integral is given by

$$\int_{cdm,q}^{\Lambda} = \int_{-\Lambda}^{\Lambda} dq_4 \int_{\epsilon^2}^{\bar{\Lambda}_{q_4}^2} d|\vec{q}|^2 \frac{|\vec{q}|}{2} \int d\Omega_{3D} \quad (\text{C.7})$$

where $\bar{\Lambda}_{q_4}^2 = \Lambda^2 - q_4^2$ is again the three-dimensional momentum cutoff of the spacial part, but this time for the four momentum q_4 . In this case the angular integral corresponds in this case with the one for finite temperature. After all, we conclude by mentioning different possibilities for the calculation of the angular part. This has to be done due to the stability of the solution, which is only achieved with a certain method for the angular calculation. But before we can show the angular integrals, we have to present the momentum parameterization for three cases, namely the vacuum, the cold dense matter and finite temperature. For this purpose we use (hyper-)spherical coordinates for the external and internal momenta, yielding

$$\begin{aligned} p &= |p|(0, 0, 0, 1), & q &= |q|(0, 0, \sin(\theta_q), \cos(\theta_q)) && \text{for the vacuum case,} \\ p &= (|\vec{p}|(0, 0, 1), p_4), & q &= (|\vec{q}|(0, \sin(\Psi_q), \cos(\Psi_q)), q_4) && \text{for cold dense matter,} \\ p &= (|\vec{p}|(0, 0, 1), \omega_p), & q &= (|\vec{q}|(0, \sin(\Psi_q), \cos(\Psi_q)), \omega_q) && \text{for finite temperature,} \end{aligned} \quad (\text{C.8})$$

where we can express the fourth component x_4 and the norm of the spacial three momentum $|\vec{x}|$ in the case of cold dense matter by the norm of the four momentum $|x|$:

$$|\vec{x}| = |x| \sin(\theta_x) \quad x_4 = |x| \cos(\theta_x) \quad (\text{C.9})$$

Since the presence of the chemical potential in the cold dense matter case leads to an assigned direction of the fourth component we need two variables in the angular kernels of the DSE's. These two variables can either be \vec{x} and x_4 or x and θ_x . The discussion about the choice between these two sets will be shifted to the next section. For now we choose the latter set, utilizing the connection (C.9). The integral representation for this set, however, is given by the first line of (C.4). Consequently we are left with two angular integrals, which we cannot calculate explicitly. The vacuum and finite temperature cases, in opposite, only include one angle between the external and internal three or four momenta. Therefore all angular integrals, except one, can be calculated explicitly. At first the angular integral presented in equations (C.1) and (C.2) can be reduced to

$$\begin{aligned} \int d\Omega_{4D} &= \frac{1}{4\pi^3} \int_0^\pi d\theta_q \sin^2(\theta_q) && \text{for vacuum,} \\ \int d\Omega_{4D} &= \frac{1}{8\pi^3} \int_0^\pi d\Psi_q \sin(\Psi_q) \int_0^\pi d\theta_q \sin^2(\theta_q) && \text{for cold dense matter,} \\ \int d\Omega_{3D} &= \frac{1}{4\pi^2} \int_0^\pi d\Psi_q \sin(\Psi_q) && \text{for finite temperature,} \end{aligned} \quad (\text{C.10})$$

which is used only in the vacuum quark-loop calculation and can be transformed into

$$\begin{aligned}
 \int d\Omega_{4D} &= \frac{1}{4\pi^3} \int_{-1}^1 dz_q \sqrt{1-z_q^2} && \text{for vacuum,} \\
 \int d\Omega_{4D} &= \frac{1}{8\pi^3} \int_{-1}^1 dy_q \int_{-1}^1 dz_q \sqrt{1-z_q^2} && \text{for cold dense matter,} \\
 \int d\Omega_{3D} &= \frac{1}{4\pi^2} \int_{-1}^1 dy_q && \text{for finite temperature,}
 \end{aligned} \tag{C.11}$$

by the substitutions $z_q = \cos(\theta_q)$, $dz_q = -\sin(\theta_q)d\theta_q$ and $y_q = \cos(\Psi_q)$, $dy_q = -\sin(\Psi_q)d\Psi_q$. This representation for the angular integration is used for all other calculations.

C.2 Numerical treatment of the momentum integrals

Since the quark and gluon integral equations are coupled, we have to calculate them simultaneously with a fix point iteration. For this purpose we use a Gauss-Legendre-integration (Gaussian quadrature and Legendre polynomials as sampling point/ grid-points) for all integrals. The internal grid unequals the external grid, which implies that we have to interpolate the quark and gluon dressing functions in space-like direction in case of finite temperatures. The temporal or better to say the heat-bath direction is therefore more complicated, since the Matsubara frequencies are only saved up to a maximal upper and lower Matsubara frequency $\omega_{p,max/min}^{\text{Quark}} = \pm\omega_p(n_p = M - 1) = \pm\pi T(2n_p + 1)$ for the quark and $\omega_{k,max/min}^{\text{Gluon}} = \pm\omega_k(n_k = M) = \pm 2\pi T n_k$ for the gluon. Usually we set $M = N$ for the quark self-energy, so that only the grid points for the Matsubara frequency integral approximation (C.6) are not saved and calculated explicitly. In case of the gluon we further apply a so-called zeroth Matsubara frequency approximation (M=0). This means that only the first bosonic Matsubara frequency is saved and the remaining Matsubara frequencies are consequently not calculated explicitly.

For these quark and gluon Matsubara frequencies, which are not saved and calculated explicitly, we have to introduce an approximation for the quark and gluon dressing functions in the integration. An important aspect to guide our search to find this approximation is the restoration of the O(4) invariance at high four momenta for the quark and gluon dressing functions. The restoration of the O(4) invariance at high four momenta means that the dressing function XY at (\vec{q}^2, ω_q) can be approximated by the corresponding dressing function for the last saved Matsubara frequency $\omega_{q,max}$ at the momentum $(\vec{q}^2 + \omega_q^2 - \omega_{q,max}^2, \omega_{q,max})$. Here XY represents one of the gluon or quark dressing functions. The exact equation for the approximation at high Matsubara frequencies ($\omega_p > \omega_{p,max}^{\text{Quark}}$) is therefore given by

$$\begin{aligned}
 X(\vec{p}^2, \pm\omega_p) &\approx X(\vec{p}^2 + \omega_p^2 - (\omega_{p,max}^{\text{Quark}})^2, \pm(\omega_{p,max}^{\text{Quark}})) \\
 Y(\vec{k}^2, \pm\omega_k) &\approx Y(\vec{k}^2 + \omega_k^2, 0)
 \end{aligned} \tag{C.12}$$

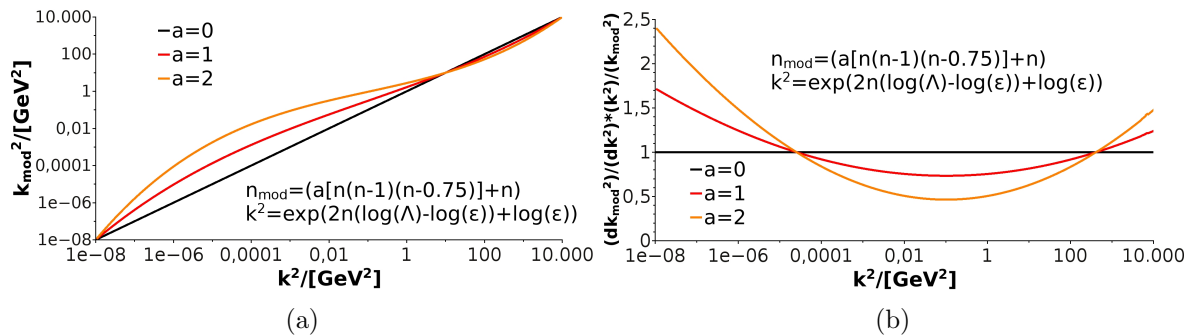


Figure C.1: Distribution function of the gluon grid for different parameters “ a ” of the variation function. In figure (a) the modified gluon grid points are displayed against the unmodified gluon grid. Figure (b) shows the change in the density of the gluon grid. For the black line the gluon grid is unchanged and therefore the grid points are logarithmically equidistant distributed. For values above one the logarithmic difference between the gluon grid points increase and therefore the density of the grid points decrease. Analog for values below one: the difference between the grid points decrease and therefore the grid point density increase. The parameter $a = 1$ is used throughout this work.

with X representing one of the three quark dressing functions (A , B or C) and Y one of the two gluon dressing functions (Z_L or Z_T). In this approximation we already employed the following facts: In case of the gluon the restoration of the $O(4)$ invariance is already fulfilled for the first gluonic Matsubara frequency, which is the reason that the zeroth Matsubara frequency approximation is valid. In contrast, we need at least five Matsubara frequencies in positive and negative direction to get a good approximation for the quark dressing function for higher Matsubara frequencies. For decreasing temperature the number of necessary Matsubara frequencies further increase.

To interpolate the space-like momentum we introduce one cubic spline object per dressing function and for every saved Matsubara frequency. In the finite temperature case the spline object is based on logarithmically equidistant distributed three momentum external grid points in case of the quark and a nearly equidistant distribution for the three momentum of the gluon. This distribution is parameterized by the function given in the figure C.1. A variation from the equidistant external grid is done to increase the grid point density in an interval very important for the integration. The vacuum case is much simpler. There, only one cubic spline object per dressing function is introduced, which is based on a logarithmically equidistant distribution of the external four momentum grid points.

The corresponding internal, radial three momentum grid (for finite temperature) or four momentum grid (in vacuum) is then divided by the external grid. This means, that we insert a Gauss-Legendre grid with a certain grid point number between every interval defined by two successive external grid points, which fulfill the constrain to be below the three or correspondingly four momentum cutoff. For the Matsubara frequencies, which are approximated by an integral, we have to mention, that we use a logarithmic Gauss-Legendre grid.

Until now we discussed the numerical treatment of the radial integrals in case of the vacuum and for finite temperatures. For the case of cold dense matter, however, we mentioned already

that the chemical potential introduces the necessity of an assigned direction for the fourth momentum component. Consequently the dressing functions need now two variables like in the temperature case ($X(\vec{p}^2, p_4)$ or $X(p^2, \theta_p)$). Further on, two possibilities to calculate the integral were discussed. As already shown in the last section one of these possibilities is to integrate the spacial part and the fourth momentum component separately, the other possibility is to use the connection (C.9) to express the spacial and temporal part by the four momentum and an angle between the four momentum and the fourth component of the same. For the latter case, the numerical treatment of the integration correspond to the vacuum, this means, that we create a logarithmically equidistant distribution of the external four momentum grid points and interpolate the dressing functions on an internal four momentum grid, which is given like in the vacuum case. Since the dressing function still depends on two variables (p and θ_p) we need multiple cubic spline objects for the different angles θ_p . We have one cubic spline object for every considered angle. Until now these angles are the grid points of a Gauß-Legendre-integration for the purpose to use them directly in the integration without interpolating them first. In the next work we pass over to an equidistant external grid for the angle, which yields the necessity of a two-dimensional interpolation of the two variables ($|p|$ and θ_p) on which the dressing functions depend on.

If we take the first possibility mentioned above the numerical treatment is a little bit more expensive, which we will explain in the following. The numerical treatment correspond to the one of finite temperature with the difference that we cannot use the dressing function approximation presented in (C.12). The reason is that the chemical potential alone breaks the O(4)-invariance strongly also at higher momenta. In the temperature case, the O(4)-invariance was broken at higher momenta only for the first Matsubara frequency, like shown in figure C.2. As a consequence we are obliged to save the external dressing functions up to the cutoff for the fourth momentum component, which yields much more p_4 -values for which we have to introduce an cubic spline object. Like in the temperature case, we introduce one cubic spline object per p_4 value. Until now these p_4 values are the grid points of a Gauß-Legendre-integration for the purpose to use them directly in the integration without interpolating them first. In future works we could introduce an equidistant external grid for p_4 and a two-dimensional interpolation method. It remains the question which of the two possibilities is more appropriate? Clearly the one, which yields smoother results and which is furthermore faster and need less memory storage. This is the case for the second possibility, since we need less angle grid points as p_4 grid points and therefore less cubic spline objects to get smoother results. The second possibility consequently will be used throughout this work. We have, however, to note that problems appear in the cold dense matter case, which are related to the convergence of the iteration. In the chiral symmetric phase of the results presented in figure 4.4, the vector dressing functions jump incessantly between possible solutions. As result the iteration never stops. Only by introducing a relaxation parameter "n" for the calculation ($X'_{new} = nX_{new} + (1-n)X_{old}$ with X representing one of the quark dressing functions) this issue is fixed.

Finally we specify the numerical treatment of the angular integration. For the angular integral

we use a normal Gauss-Legendre grid but the integration interval is split into two (in case of $z_q = \cos(\theta_q)$ or $y_q = \cos(\Psi_q)$ integration) or four (in case of θ_q or Ψ_q integration) intervals to improve the precision and to avoid exact zeros in the angular grid, which could lead to infinities and numerical artifacts. Therefore we take the two intervals $[-1, 0]$ and $[0, 1]$ for z_q and y_q and the four intervals $[0, \frac{\pi}{4}]$, $[\frac{\pi}{4}, \frac{\pi}{2}]$, $[\frac{\pi}{2}, \frac{3\pi}{4}]$ and $[\frac{3\pi}{4}, \pi]$ for θ_q and Ψ_q .

The dressing functions are only calculated and saved up to a given upper (and lower) momentum above (below) which the dressing function is extrapolated with a constant value which equals the last (first) dressing function value. For this purpose, we introduce an extrapolation method for the quark, which is defined by the following equation.

$$X(\bar{q}^2, \omega_q) \approx \begin{cases} X(\bar{q}^2 + \omega_q^2 - \omega_{q,min}^2, \omega_{q,min}) & \text{if } \bar{q}^2 + \omega_q^2 < \Lambda^2, \omega_q < \omega_{q,min} \\ X(\bar{q}^2, \omega_q) & \text{if } \bar{q}^2 + \omega_q^2 < \Lambda^2, \omega_{q,min} < \omega_q < \omega_{q,max} \\ X(\bar{q}^2 + \omega_q^2 - \omega_{q,max}^2, \omega_{q,max}) & \text{if } \bar{q}^2 + \omega_q^2 < \Lambda^2, \omega_{q,max} < \omega_q \\ X(\Lambda^2 + \omega_q^2 - \omega_{q,min}^2, \omega_{q,min}) & \text{if } \bar{q}^2 + \omega_q^2 > \Lambda^2, \omega_q < 0 \\ X(\Lambda^2 + \omega_q^2 - \omega_{q,max}^2, \omega_{q,max}) & \text{if } \bar{q}^2 + \omega_q^2 > \Lambda^2, 0 < \omega_q \end{cases} \quad (\text{C.13})$$

This extrapolation suffers from different problems, like the imbalance in the momentum boundary at which the extrapolation is done. Neither at a constant four nor at a constant three momentum the extrapolation is done. In contrast the extrapolation point depends on the Matsubara frequency. Further troublesome is that dressing functions of saved Matsubara frequencies ($\omega_{q,min} < \omega_q < \omega_{q,max}$) and four momenta above the $O(4)$ cutoff Λ are mapped onto the corresponding maximal Matsubara frequency $\omega_{q,min}$ or $\omega_{q,max}$. If we consider figure C.2, it is

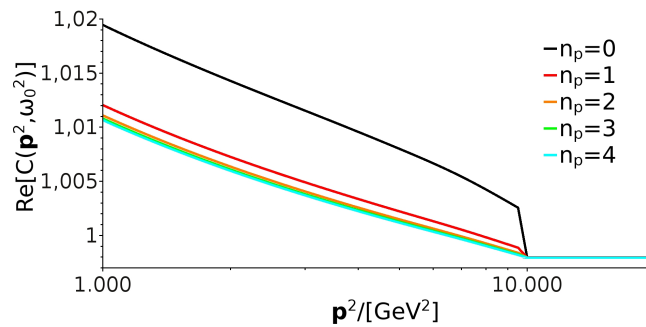


Figure C.2: Problem of the extrapolation routine (C.13). The real part of the second vector dressing function is shown against the three momentum for different Matsubara frequencies. Above a given three momentum the dressing function for all Matsubara frequencies are approximated constantly by the value of the highest Matsubara frequency.

most evident, that this mapping could produce problems. The figure shows the UV behavior of the second vector dressing function C for different Matsubara frequencies. As one can see the dressing functions are extrapolated with the wrong value. Despite these disadvantages, the extrapolation is used for the sake of comparison with previous works. It is also to mention, that this predominantly effects the thermal mass and only implicitly all other quantities. Nonethe-

$\mu_q/[GeV]$	$T/[GeV]$	$\Re[S]$	$\Im[S]$	$\Re[D_T]$	$\Re[D_L]$	$\langle \bar{\Psi}\Psi \rangle_u$	Δ_{us}	m_{th}^L
0.0	0.1	0.50%	0.27%	0.09%	1.91%	0.04%	0.00%	5.69%
0.0	0.2	6.35%	2.13%	0.42%	5.03%	0.07%	0.11%	5.86%
0.1	0.1	0.50%	386.12%	0.09%	1.87%	0.04%	0.00%	5.34%
0.1	0.2	4.72%	54.69%	0.39%	4.86%	0.04%	0.11%	5.63%
0.2	0.1	1.00%	117.97%	0.11%	2.59%	0.08%	0.01%	5.42%
0.2	0.2	2.40%	22.41%	0.33%	4.42%	0.01%	0.01%	5.06%

Table C.1: Relative difference of important observables between the two presented extrapolation methods for different temperatures and chemical potentials. S represents the maximum of the relative difference of all quark dressing functions. Analog $D_{L/T}$ shows the maximum of the relative difference of the transversal or longitudinal gluon dressing functions and the regular part too.

less, we will mention a suggestion for improvement for coming works. The following alternative, extrapolates the dressing functions for every Matsubara frequency at the same four momentum, which equals the $O(4)$ cutoff Λ . Furthermore every Matsubara frequency has it's own extrapolation value, which resolves the problem of the last extrapolation method. The new extrapolation method can be written as

$$X(\tilde{q}^2, \omega_q) \approx \begin{cases} X(\tilde{q}^2 - \omega_{q,min}^2, \omega_{q,min}) & \text{if } \omega_q < \omega_{q,min} \\ X(\tilde{q}^2 - \omega_q^2, \omega_q) & \text{if } \omega_{q,min} < \omega_q < \omega_{q,max} \\ X(\tilde{q}^2 - \omega_{q,max}^2, \omega_{q,max}) & \text{if } \omega_{q,max} < \omega_q \end{cases} \quad (\text{C.14})$$

with the four momentum

$$\tilde{q}^2 = \begin{cases} \tilde{q}^2 + \omega_q^2 & \text{if } \tilde{q}^2 + \omega_q^2 < \Lambda^2 \\ \Lambda^2 & \text{if } \tilde{q}^2 + \omega_q^2 > \Lambda^2 \end{cases} \quad (\text{C.15})$$

In table C.1 the effect on different quantities compared to the previous extrapolation method is recorded. We can additionally mention that the best extrapolation would be to replace the constant extrapolation by an extrapolation with a fit-function, but this can be a subject of a coming work.

Until now we only discussed the quark extrapolation, the gluon extrapolation, however, is kept much simpler. In the quenched case we access the functional form of the related fit-function without an extrapolation. Only in the unquenched case with Lattice-fits we have to add two terms, for which extrapolations become important. The first term is the thermal mass contribution, where we exactly know the functional form, but have a calculated parameter. The second term is the regular part of the renormalized quark-loop. While the first term is not extrapolated since the functional form is exactly known, the second term is extrapolated constantly at a constant three momentum (Λ) for every Matsubara frequency. The important aspect concerning the gluon is that the extrapolation does not affect any quantity very strong, unlike the quark extrapolation influenced the thermal mass. This implies that the extrapolation details are of

no consequence. Now that we discussed the extrapolation methods for the quark and the gluon for finite temperatures, we can mention that the extrapolation method for the vacuum and cold dense matter case, using the four momentum and the angle, is much simpler. Here the dressing functions are extrapolated constantly above a four momentum which equals the $O(4)$ cutoff Λ .

C.3 Thermal mass calculation

As already addressed previously, the quark-loop is split up into a infrared divergent part, proportional to the thermal mass of the gluon and a divergence free (regular) part. The latter one is not strongly sensitive to high accuracy and the explicit Matsubara sum, in contrast to the thermal mass. Consequently the mentioned separation is necessary and the thermal mass is calculated regarding the following two aspects: At first the thermal mass is calculated with higher accuracy, which means that a higher grid point number is used for the integration and the angular part is solved analytically. Furthermore we have to make sure that the $O(4)$ invariance is restored numerically by introducing the following variation

$$C(\vec{q}^2, \omega_q) \longrightarrow \left(1 - e^{-\frac{q^2}{\Lambda_{AC}}}\right) A(\vec{q}^2, \omega_q) + e^{-\frac{q^2}{\Lambda_{AC}}} C(\vec{q}^2, \omega_q) \quad (\text{C.16})$$

with the parameter $\Lambda_{AC} = 40\text{GeV}^2$. Secondly we use a higher cutoff - usually 2000GeV . This is done to compare with older works, where the higher cutoff was introduced because of a possible plateau of the thermal mass at higher $O(4)$ cutoff values, where the thermal mass is almost independent from the cutoff. In this work we cannot observe such a plateau. The problem with the use of the higher cutoff is that we have to pay attention on the way we extrapolate, since the thermal mass will be strongly dependent on the extrapolation method. There is the opportunity but also the necessity to improve this issue. Regarding the regular part of the quark-loop we have to mention that we have to make sure, that the thermal mass is subtracted with the same numeric, which means, that the same grid has to be used and that the angular part has to be calculated numerically - even though it could easily be calculated analytically. Naturally the variation given in equation (C.16) cannot be included for this purpose.

C.4 Renormalization, order parameter and the phase diagram calculation

After discussing the numerical side of the integral calculations we will focus at first on the renormalization. In the quark renormalization section was already mentioned, that the strange quark mass renormalization constant is set to the light quark mass renormalization constant ($Z_m^{\text{strange}} = Z_m^{\text{light}}$). The reason is that the regularized quark condensate changes the sign, if this settlement is skipped. As we have seen in the results for the unquenched case with lattice fits and for two plus one quark flavors the regularized quark condensate still changes the sign, but only for high temperature and chemical potential (see 3.6). Furthermore only small values are

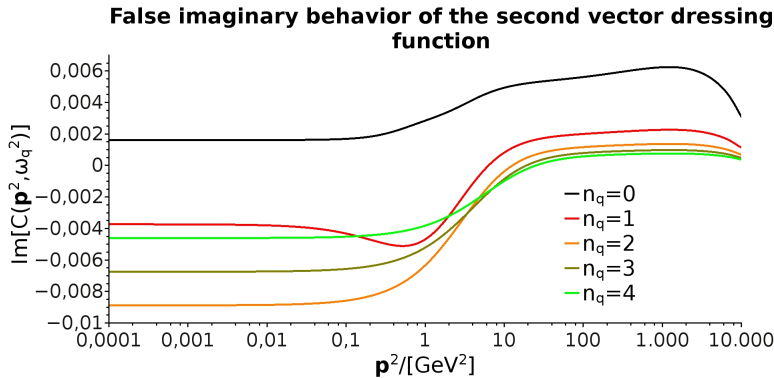


Figure C.3: Imaginary part of the second vector dressing function against the three momentum \vec{p}^2 at the phase diagram point $(T, \mu_q) = (100, 100)$ MeV for unquenched QCD with $N_f = 2 + 1$ quark flavors and lattice fits.

adopted if the regularized quark condensate changes the sign. The reason for the remaining change of the sign could be attributed to the fact that we set the mass renormalization constants to a value which already includes dynamical effects and lies in the region where the mass renormalization constant drops significantly in figure 2.2. Or it is attributed to the fact that we use vacuum renormalization although we should use a medium renormalization.

A possibility to avoid the problem of an inclusion of the dynamical effects could be to set $Z_m^{\text{light}} = Z_m^{\text{strange}}$ or to calculate the mass renormalization constant for a high mass and set Z_m^{light} and Z_m^{strange} to this value. Both possibilities can be discussed in coming works. Although $Z_m^{\text{light}} = Z_m^{\text{strange}}$ is the better choice we used $Z_m^{\text{strange}} = Z_m^{\text{light}}$ for the sake of comparison in this work.

Also for one other physical observables we have to go into the numerical details. The mentioned observable is the quark density, which is not calculated in this work, but for the sake of comparison with previous works, we have to mention the necessary numerical changes due to this calculation. In figure C.3 we can see, that the imaginary part of the quark dressing function does not decrease exponentially to zero, as it should, but instead does not vanish in ultraviolet - with the numeric presented up to this point. This behavior leads to errors in the calculation of the quark density, which we can remove if we separate the calculation of the real and imaginary part of the quark self-energy and increase the ultraviolet cutoff of the imaginary part by a factor “ a ”, which we normally set to 15. Additionally we change the regularization of the imaginary part, which leads to the following equations for the quark self-energy integrations in medium

$$\begin{aligned}
 \sum_q^{\Lambda_q} &= T \sum_{n_q}^{|\omega_q| < \Lambda} \int_{\epsilon^2}^{\tilde{\Lambda}_{n_q}^2} d|\vec{q}|^2 \frac{|\vec{q}|}{2} \int d\Omega_{3D} \Re [f(\vec{q}^2, \omega_q, \theta_q)] \\
 \sum_q^{\Lambda_q} &= T \sum_{n_q}^{|\omega_q| < a\Lambda} \int_{\epsilon^2}^{(a\Lambda)^2} d|\vec{q}|^2 \frac{|\vec{q}|}{2} \int d\Omega_{3D} \Im [f(\vec{q}^2, \omega_q, \theta_q)]
 \end{aligned} \tag{C.17}$$

Finally we conclude by giving some numerical details concerning the phase diagram calculation. As already introduced and calculated previously we know, that the crossover transition line turns

at the second order critical end point into a region of first order phase transitions, specified by the upper and lower spinodals. The question is now how we determine these spinodals. The two spinodals represent two different, stable solutions for the coupled system. We can control which solution we want to achieve by two contributions. First we set different starting guesses for the scalar dressing function B (1GeV for the upper and 0.01GeV for the lower spinodal) and secondly we can control which solution we get by choosing the direction of the phase diagram calculation. This means: In case of the upper spinodal we begin to calculate at the lower temperatures and then go to higher ones. For the lower spinodal, however, we go the other way around. For this purpose, it is to say that we utilize the iterated version of the quark dressing function from the last calculated temperature as starting guess for the new phase diagram calculation, after having determined the gluon for the quark starting guess $B = 1\text{GeV}$ or $B = 0.01\text{GeV}$. This procedure additionally accelerates our calculation.

C.5 Numerical details of the pion

In this last section we want to state some numerical details to the calculation of the Bethe-Salpeter amplitude. Since the homogeneous BSE (2.91) does not include an inhomogeneity factor, which stops the iteration, we need an abort criterion for the eigenvalue equation (2.92). For this purpose, we use the power iteration method, which utilizes the convergence of the eigenvalue as abort criterion. For the power iteration, we apply the kernel $\tilde{K}(P^2)$ iteratively onto a BSA $\Gamma_n(P^2)$. We start with an initial guess for the BSA $\Gamma_0(P^2)$, which is usually 1. In equations with functional notation this can be written as

$$\hat{K}(P^2) |\Gamma_n(P^2)\rangle = \lambda_n(P^2) |\Gamma_{n+1}(P^2)\rangle \quad (\text{C.18})$$

where we denoted the BSA $\Gamma_n(P^2)$ as Hilbert-vector $|\Gamma_n\rangle$ and the kernel $\tilde{K}(P^2)$ as operator \hat{K} . For increasing orders of application, the iterative eigenvalue trends towards the real eigenvalue $\lambda_n(P^2) \xrightarrow{n \rightarrow \infty} \lambda(P^2)$. The iterative eigenvalue is therefore calculated by

$$\lambda_n(P^2) = \frac{\langle \Gamma_n(P^2) | \Gamma_{n+1}(P^2) \rangle}{\langle \Gamma_n(P^2) | \Gamma_n(P^2) \rangle} \quad (\text{C.19})$$

The notation $\langle \Gamma_n |$ represents the charge conjugated BSA $\bar{\Gamma}_n(P^2)$. In order that the convergence works, we have to normalize the iterative BSA before we calculate the eigenvalue. Therefore we divided the last equation by $\langle \Gamma_n(P^2) | \Gamma_n(P^2) \rangle$. In full glory, using the Chebyshev expansion and only the first pion dressing function the eigenvalue is given by

$$\begin{aligned} \lambda_n(P^2) &= \frac{1}{\mathcal{N}} \int_q^\Lambda \sum_{k_1, k_2=0}^{\tilde{N}} \tilde{E}_{k_1}^n(q^2, P^2) \tilde{E}_{k_2}^{n+1}(q^2, P^2) \tilde{T}_{k_1}(z_q) \tilde{T}_{k_2}(z_q) \\ \mathcal{N} &= \int_q^\Lambda \sum_{k_1, k_2=0}^{\tilde{N}} \tilde{E}_{k_1}^n(q^2, P^2) \tilde{E}_{k_2}^n(q^2, P^2) \tilde{T}_{k_1}(z_q) \tilde{T}_{k_2}(z_q) \end{aligned} \quad (\text{C.20})$$

Acknowledgements

At the end, it remains me to express my gratitude to some supporters and friends: At first I want to thank my family and my girlfriend for their support throughout my studies. You were always there for me. Next I would like to thank my fellow students, especially Jonas Wilhelm, Jonas Schäfer and Daniel Zink, for an eventful and fascinating time during our studies. Particularly my gratitude goes to Christian Welzbacher to introduce me into the interesting topic of QCD phase diagram calculations. Additionally I want to thank him and the rest of the group for helpful discussions and their help every time. Finally I would like to express my appreciation for Richard Williams and Esther Weil as well as my soulmate Desiree Gölz for looking through my thesis. I conclude by thanking Christian Fischer to give me the opportunity to work in this supportive group.

Bibliography

- [1] L. P. Kadanoff, *Statistical Physics: Statics, Dynamics and Renormalization*. World Scientific, 2000, p. 483, ISBN: 9810237642. DOI: [10.1063/1.1397396](https://doi.org/10.1063/1.1397396). [Online]. Available: <https://books.google.com/books?id=22dadF5p6gYC%7B%5C%7Dpgis=1%7B%7D5Cnhttps://books.google.com/books?id=22dadF5p6gYC%7B%7D7B%7B%5C%7D%7B%7D7Dpgis=1>.
- [2] C. A. Welzbacher, “Quarks and gluons in the phase diagram of quantum chromodynamics,” PhD thesis, 2016.
- [3] O. Philipsen, “Lattice qcd at non-zero temperature and baryon density bt - modern perspectives in lattice qcd: quantum field theory and high performance computing,” *Modern Perspectives in Lattice QCD: Quantum Field Theory and High Performance Computing*, 2011. DOI: [10.1088/0954-3899/39/9/093002](https://doi.org/10.1088/0954-3899/39/9/093002). arXiv: [1009.4089](https://arxiv.org/abs/1009.4089). [Online]. Available: http://arxiv.org/abs/1009.4089v1%7B%7D5Cnfile:///Users/antonin/Documents/Biblioth%C3%A8que/antonin's%20Library/Library.papers3/Books/2011/Philipsen/2011%7B%5C_%7DPhilipsen.pdf%7B%7D5Cnpapers3://publication/uuid/31FFB998-194F-4BBD-B1B4-5F44D4935928.
- [4] —, “The qcd equation of state from the lattice,” *Progress in Particle and Nuclear Physics*, vol. 70, pp. 55–107, 2013, ISSN: 01466410. DOI: [10.1016/j.pnpnp.2012.09.003](https://doi.org/10.1016/j.pnpnp.2012.09.003). arXiv: [1207.5999](https://arxiv.org/abs/1207.5999).
- [5] J. M. Pawłowski, “Aspects of the functional renormalisation group,” *Annals of Physics*, vol. 322, no. 12, pp. 2831–2915, 2007, ISSN: 00034916. DOI: [10.1016/j.aop.2007.01.007](https://doi.org/10.1016/j.aop.2007.01.007). arXiv: [0512261v2](https://arxiv.org/abs/0512261v2) [[hep-th](#)].
- [6] B. -.-J. Schaefer and J. Wambach, “Renormalization group approach towards the qcd phase diagram,” *Physics of Particles and Nuclei*, vol. 39, no. 7, pp. 1025–1032, 2008, ISSN: 1063-7796. DOI: [10.1134/S1063779608070083](https://doi.org/10.1134/S1063779608070083). arXiv: [0611191](https://arxiv.org/abs/0611191) [[hep-ph](#)]. [Online]. Available: <http://arxiv.org/abs/hep-ph/0611191%7B%7D5Cnhttp://link.springer.com/10.1134/S1063779608070083>.
- [7] R. Aouane, F. Burger, E. M. Ilgenfritz, M. Müller-Preussker, and A. Sternbeck, “Landau gauge gluon and ghost propagators from lattice qcd with n f=2 twisted mass fermions at finite temperature,” *Physical Review D - Particles, Fields, Gravitation and Cosmology*, vol. 87, no. 11, pp. 1–11, 2013, ISSN: 15507998. DOI: [10.1103/PhysRevD.87.114502](https://doi.org/10.1103/PhysRevD.87.114502). arXiv: [1212.1102](https://arxiv.org/abs/1212.1102) [[hep-lat](#)].

-
- [8] C. D. Roberts and S. M. Schmidt, “Dyson-schwinger equations: density, temperature and continuum strong qcd,” *Progress in Particle and Nuclear Physics*, vol. 45, no. 1, p. 103, 2000, ISSN: 01466410. DOI: [10.1016/S0146-6410\(00\)90011-5](https://doi.org/10.1016/S0146-6410(00)90011-5). arXiv: [0005064 \[nucl-th\]](https://arxiv.org/abs/nucl-th/0005064). [Online]. Available: <http://www.sciencedirect.com/science/article/pii/S0146641000900115%7B%7D5Cnhttp://arxiv.org/abs/nucl-th/0005064>.
- [9] J. Luecker and C. S. Fischer, “Two-flavor qcd at finite temperature and chemical potential in a functional approach,” *Progress in Particle and Nuclear Physics*, vol. 67, no. 2, pp. 200–205, 2012, ISSN: 01466410. DOI: [10.1016/j.pnpnp.2011.12.018](https://doi.org/10.1016/j.pnpnp.2011.12.018). arXiv: [1111.0180](https://arxiv.org/abs/1111.0180).
- [10] C. S. Fischer, J. Luecker, and C. a. Welzbacher, “Phase structure of three and four flavor qcd,” *Physical Review D*, vol. 90, no. 3, p. 034022, 2014, ISSN: 1550-7998. DOI: [10.1103/PhysRevD.90.034022](https://doi.org/10.1103/PhysRevD.90.034022). arXiv: [1405.4762v2](https://arxiv.org/abs/1405.4762v2). [Online]. Available: <http://link.aps.org/doi/10.1103/PhysRevD.90.034022>.
- [11] Y. Jiang, L. J. Luo, and H. S. Zong, “A model study of quark number susceptibility at finite temperature beyond rainbow-ladder approximation,” *Journal of High Energy Physics*, vol. 2011, no. 2, pp. 1–17, 2011, ISSN: 11266708. DOI: [10.1007/JHEP02\(2011\)066](https://doi.org/10.1007/JHEP02(2011)066). arXiv: [arXiv:1102.1532v1](https://arxiv.org/abs/1102.1532v1).
- [12] F. Gao and Y.-x. Liu, “Interface effect in qcd phase transitions via dyson-schwinger equation approach,” pp. 1–9, 2016. DOI: [10.1103/PhysRevD.94.094030](https://doi.org/10.1103/PhysRevD.94.094030). arXiv: [1609.08038](https://arxiv.org/abs/1609.08038). [Online]. Available: <http://arxiv.org/abs/1609.08038%7B%7D0Ahttp://dx.doi.org/10.1103/PhysRevD.94.094030>.
- [13] S. X. Qin, L. Chang, Y. X. Liu, and C. D. Roberts, “Quark spectral density and strongly-coupled quark-gluon plasma,” *Physical Review D - Particles, Fields, Gravitation and Cosmology*, vol. 84, no. 1, pp. 3–6, 2011, ISSN: 15507998. DOI: [10.1103/PhysRevD.84.014017](https://doi.org/10.1103/PhysRevD.84.014017). arXiv: [1010.4231](https://arxiv.org/abs/1010.4231).
- [14] C. S. Fischer and J. a. Mueller, “Critical scaling at the qcd $n_f=2$ chiral phase transition,” *Physical Review D*, vol. 84, no. 5, p. 054013, 2011, ISSN: 1550-7998. DOI: [10.1103/PhysRevD.84.054013](https://doi.org/10.1103/PhysRevD.84.054013). arXiv: [1106.2700](https://arxiv.org/abs/1106.2700). [Online]. Available: <http://link.aps.org/doi/10.1103/PhysRevD.84.054013>.
- [15] S. X. Qin and D. H. Rischke, “Quark spectral function and deconfinement at nonzero temperature,” *Physical Review D - Particles, Fields, Gravitation and Cosmology*, vol. 88, no. 5, pp. 1–6, 2013, ISSN: 15507998. DOI: [10.1103/PhysRevD.88.056007](https://doi.org/10.1103/PhysRevD.88.056007). arXiv: [1304.6547](https://arxiv.org/abs/1304.6547).
- [16] F. Gao, S. X. Qin, Y. X. Liu, C. D. Roberts, and S. M. Schmidt, “Zero mode in a strongly coupled quark gluon plasma,” *Physical Review D - Particles, Fields, Gravitation and Cosmology*, vol. 89, no. 7, pp. 1–11, 2014, ISSN: 15502368. DOI: [10.1103/PhysRevD.89.076009](https://doi.org/10.1103/PhysRevD.89.076009). arXiv: [1401.2406](https://arxiv.org/abs/1401.2406).

- [17] N. Strodthoff, B.-J. Schaefer, and L. von Smekal, “Quark-meson-diquark model for two-color qcd,” no. 4, pp. 1–22, 2011. DOI: [10.1103/PhysRevD.85.074007](https://doi.org/10.1103/PhysRevD.85.074007). arXiv: [1112.5401](https://arxiv.org/abs/1112.5401). [Online]. Available: <http://arxiv.org/abs/1112.5401%7B%7D0Ahttp://dx.doi.org/10.1103/PhysRevD.85.074007>.
- [18] G. Eichmann, C. S. Fischer, and C. A. Welzbacher, “Baryon effects on the location of qcd’s critical end point,” *Physical Review D - Particles, Fields, Gravitation and Cosmology*, vol. 93, no. 3, 2016, ISSN: 15502368. DOI: [10.1103/PhysRevD.93.034013](https://doi.org/10.1103/PhysRevD.93.034013). arXiv: [1509.0208](https://arxiv.org/abs/1509.0208).
- [19] C. S. Fischer, D. Nickel, and J. Wambach, “Hadronic unquenching effects in the quark propagator,” *Physical Review D - Particles, Fields, Gravitation and Cosmology*, vol. 76, no. 9, pp. 1–27, 2007, ISSN: 15507998. DOI: [10.1103/PhysRevD.76.094009](https://doi.org/10.1103/PhysRevD.76.094009). arXiv: [0705.4407](https://arxiv.org/abs/0705.4407).
- [20] C. S. Fischer and R. Williams, “Beyond the rainbow: effects from pion back-coupling,” *Physical Review D - Particles, Fields, Gravitation and Cosmology*, vol. 78, no. 7, pp. 1–9, 2008, ISSN: 15507998. DOI: [10.1103/PhysRevD.78.074006](https://doi.org/10.1103/PhysRevD.78.074006). arXiv: [0808.3372](https://arxiv.org/abs/0808.3372).
- [21] G. Eichmann, *Einführung in die hadronenphysik lecturenotes*.
- [22] J. Luecker, “Chiral and deconfinement phase transitions in $n_f = 2$ and $n_f = 2 + 1$ quantum chromodynamics,” PhD thesis, 2013, pp. 1–125.
- [23] M. Le Bellac, *Thermal Field Theory*. Press syndicate of university of cambridge, 1996, p. 272, ISBN: 0521654777.
- [24] C. S. Fischer, “Non-perturbative propagators, running coupling and dynamical mass generation in ghost-antighost symmetric gauges in qcd,” p. 163, 2003. arXiv: [0304233](https://arxiv.org/abs/0304233) [[hep-ph](https://arxiv.org/abs/0304233)]. [Online]. Available: <http://arxiv.org/abs/hep-ph/0304233>.
- [25] M. Faber, *Quantenchromodynamik i lecturenotes*.
- [26] P. Cvitanovic, “Field theory,” *Nordita lecture notes*, no. January, 1983.
- [27] J. Berges, “Introduction to nonequilibrium quantum field theory,” *AIP Conference Proceedings*, vol. 739, no. 1, pp. 3–62, 2004, ISSN: 0094243X. DOI: [10.1063/1.1843591](https://doi.org/10.1063/1.1843591). arXiv: [0409233](https://arxiv.org/abs/0409233) [[hep-ph](https://arxiv.org/abs/0409233)]. [Online]. Available: <http://scitation.aip.org/content/aip/proceeding/aipcp/10.1063/1.1843591>.
- [28] M. Blank, “Properties of quarks and mesons in the dyson-schwinger/bethe-salpeter approach,” *Chemistry*, p. 108, 2011. arXiv: [1106.4843](https://arxiv.org/abs/1106.4843). [Online]. Available: <http://arxiv.org/abs/1106.4843>.
- [29] J. M. Cornwall, R. Jackiw, and E. Tomboulis, “Effective action for composite operators,” *Phys. Rev. D*, vol. 10, no. 8, pp. 2428–2445, 1974. DOI: [10.1103/PhysRevD.10.2428](https://doi.org/10.1103/PhysRevD.10.2428). [Online]. Available: <http://link.aps.org/doi/10.1103/PhysRevD.10.2428>.
- [30] G. Eichmann, “Hadron properties from qcd bound-state equations,” 2009. arXiv: [0909.0703](https://arxiv.org/abs/0909.0703). [Online]. Available: <http://arxiv.org/abs/0909.0703>.

-
- [31] P. Maris and C. D. Roberts, “Pi- and k-meson bethe-salpeter amplitudes,” *Physical Review C*, pp. 1–35, 1997, ISSN: 0556-2813. DOI: [10.1103/PhysRevC.56.3369](https://doi.org/10.1103/PhysRevC.56.3369). arXiv: [9708029](https://arxiv.org/abs/9708029) [nucl-th].
- [32] L. Fister and J. M. Pawłowski, “Quark confinement from correlation functions,” p. 8, 2013. DOI: [10.1103/PhysRevD.88.045010](https://doi.org/10.1103/PhysRevD.88.045010). arXiv: [1302.1373](https://arxiv.org/abs/1302.1373). [Online]. Available: <http://arxiv.org/abs/1302.1373>.
- [33] D. R. Müller, “[ph.d thesis] qcd at finite density with dyson-schwinger equations,” 2013.
- [34] T. K. Herbst, J. M. Pawłowski, and B. J. Schaefer, “The phase structure of the polyakov-quark-meson model beyond mean field,” *Physics Letters, Section B: Nuclear, Elementary Particle and High-Energy Physics*, vol. 696, no. 1-2, pp. 58–67, 2011, ISSN: 03702693. DOI: [10.1016/j.physletb.2010.12.003](https://doi.org/10.1016/j.physletb.2010.12.003). arXiv: [1008.0081](https://arxiv.org/abs/1008.0081).
- [35] T. K. Herbst, J. M. Pawłowski, and B.-j. Schaefer, “On the phase structure and thermodynamics of qcd,” p. 12, 2013, ISSN: 1550-7998. DOI: [10.1103/PhysRevD.88.014007](https://doi.org/10.1103/PhysRevD.88.014007). arXiv: [1302.1426](https://arxiv.org/abs/1302.1426). [Online]. Available: <http://arxiv.org/abs/1302.1426>.
- [36] C. S. Fischer, A. Maas, and J. A. Müller, “Chiral and deconfinement transition from correlation functions: su(2) vs. su(3),” *European Physical Journal C*, vol. 68, no. 1, pp. 165–181, 2010, ISSN: 14346044. DOI: [10.1140/epjc/s10052-010-1343-1](https://doi.org/10.1140/epjc/s10052-010-1343-1). arXiv: [1003.1960](https://arxiv.org/abs/1003.1960) [hep-ph].
- [37] R. Williams, “The quark-gluon vertex in landau gauge bound-state studies,” *European Physical Journal A*, vol. 51, no. 5, 2015, ISSN: 1434601X. DOI: [10.1140/epja/i2015-15057-4](https://doi.org/10.1140/epja/i2015-15057-4). arXiv: [arXiv:1301.3672v1](https://arxiv.org/abs/1301.3672v1).
- [38] L. Fister and J. M. Pawłowski, “Yang-mills correlation functions at finite temperature,” p. 18, 2011. arXiv: [1112.5440](https://arxiv.org/abs/1112.5440). [Online]. Available: <http://arxiv.org/abs/1112.5440>.
- [39] E. Rojas, J. P. B. C. De Melo, B. El-Bennich, O. Oliveira, and T. Frederico, “On the quark-gluon vertex and quark-ghost kernel: combining lattice simulations with dyson-schwinger equations,” *Journal of High Energy Physics*, vol. 2013, no. 10, 2013, ISSN: 11266708. DOI: [10.1007/JHEP10\(2013\)193](https://doi.org/10.1007/JHEP10(2013)193). arXiv: [1306.3022](https://arxiv.org/abs/1306.3022) [hep-ph].
- [40] P. Maris and P. C. Tandy, “Bethe-salpeter study of vector meson masses and decay constants,” *Physical Review C*, vol. 60, no. 5, p. 29, 1999, ISSN: 0556-2813. DOI: [10.1103/PhysRevC.60.055214](https://doi.org/10.1103/PhysRevC.60.055214). arXiv: [9905056](https://arxiv.org/abs/9905056) [nucl-th]. [Online]. Available: <http://prc.aps.org/abstract/PRC/v60/i5/e055214%7B%7D5Cnhttp://link.aps.org/doi/10.1103/PhysRevC.60.055214%7B%7D5Cnhttp://arxiv.org/abs/nucl-th/9905056>.
- [41] S. X. Qin, L. Chang, Y. X. Liu, C. D. Roberts, and D. J. Wilson, “Interaction model for the gap equation,” *Physical Review C - Nuclear Physics*, vol. 84, no. 4, pp. 1–5, 2011, ISSN: 05562813. DOI: [10.1103/PhysRevC.84.042202](https://doi.org/10.1103/PhysRevC.84.042202). arXiv: [1108.0603](https://arxiv.org/abs/1108.0603).

- [42] S.-x. Qin, L. Chang, H. Chen, Y.-x. Liu, and C. D. Roberts, “Phase diagram and critical endpoint for strongly-interacting quarks,” *Phys.Rev.Lett.*, vol. 106, p. 172301, 2011. DOI: [10.1103/PhysRevLett.106.172301](https://doi.org/10.1103/PhysRevLett.106.172301). arXiv: [1011.2876](https://arxiv.org/abs/1011.2876) [nucl-th].
- [43] H. Chen, W. Yuan, L. Chang, Y. X. Liu, T. Klähn, and C. D. Roberts, “Chemical potential and the gap equation,” *Physical Review D - Particles, Fields, Gravitation and Cosmology*, vol. 78, no. 11, 2008, ISSN: 15507998. DOI: [10.1103/PhysRevD.78.116015](https://doi.org/10.1103/PhysRevD.78.116015). arXiv: [arXiv: 0807.2755v1](https://arxiv.org/abs/0807.2755v1).
- [44] T. Klähn, C. D. Roberts, L. Chang, H. Chen, and Y. X. Liu, “Cold quarks in medium: an equation of state,” *Physical Review C - Nuclear Physics*, vol. 82, no. 3, pp. 1–5, 2010, ISSN: 05562813. DOI: [10.1103/PhysRevC.82.035801](https://doi.org/10.1103/PhysRevC.82.035801). arXiv: [0911.0654](https://arxiv.org/abs/0911.0654).
- [45] C. S. Fischer, P. Watson, and W. Cassing, “Probing unquenching effects in the gluon polarization in light mesons,” *Physical Review D - Particles, Fields, Gravitation and Cosmology*, vol. 72, no. 9, pp. 1–23, 2005, ISSN: 15507998. DOI: [10.1103/PhysRevD.72.094025](https://doi.org/10.1103/PhysRevD.72.094025). arXiv: [0509213v1](https://arxiv.org/abs/0509213v1) [arXiv:hep-ph].
- [46] C. D. Roberts and S. Schmidt, “Dyson-schwinger equations and the quark-gluon plasma,” pp. 1–13, 1999. arXiv: [9903075](https://arxiv.org/abs/9903075) [nucl-th]. [Online]. Available: <http://arxiv.org/abs/nucl-th/9903075>.
- [47] P. Maris and P. C. Tandy, “Mesons as bound states of confined quarks: zero and finite temperature,” no. July, 2001. arXiv: [0109035](https://arxiv.org/abs/0109035) [nucl-th]. [Online]. Available: <http://arxiv.org/abs/nucl-th/0109035>.
- [48] E. Weil, “Investigation of neutral pion decay within the dyson-schwinger framework,” 2016.
- [49] L. Yu-Xin, C. Jing-Yi, C. Lei, and Y. Wei, “Density dependence of the mass and decay constant of pion in nuclear matter in the dyson-schwinger equation approach of qcd,” *Chinese Physics Letters*, vol. 22, no. 1, pp. 46–49, Jan. 2005, ISSN: 0256-307X. DOI: [10.1088/0256-307X/22/1/014](https://doi.org/10.1088/0256-307X/22/1/014). [Online]. Available: <http://stacks.iop.org/0256-307X/22/i=1/a=014?key=crossref.b027b05451e69cf6a939591c1564ca88>.
- [50] C. D. Roberts, “Nonperturbative effects in qcd at finite temperature and density,” *Phys.Part.Nucl.*, vol. 30, pp. 223–257, 1999, ISSN: 10637796. DOI: [10.1134/1.953105](https://doi.org/10.1134/1.953105), [10.1134/1.953105](https://doi.org/10.1134/1.953105). arXiv: [nucl-th/9806088](https://arxiv.org/abs/nucl-th/9806088) [nucl-th].

Selbstständigkeitserklärung

Hiermit versichere ich, die vorgelegte Thesis selbstständig und ohne unerlaubte fremde Hilfe und nur mit den Hilfen angefertigt zu haben, die ich in der Thesis angegeben habe. Alle Textstellen, die wörtlich oder sinngemäß aus veröffentlichten Schriften entnommen sind, und alle Angaben die auf mündlichen Auskünften beruhen, sind als solche kenntlich gemacht. Bei den von mir durchgeführten und in der Thesis erwähnten Untersuchungen habe ich die Grundsätze gute wissenschaftlicher Praxis, wie sie in der ‚Satzung der Justus-Liebig-Universität zur Sicherung guter wissenschaftlicher Praxis‘ niedergelegt sind, eingehalten. Gemäß § 25 Abs. 6 der Allgemeinen Bestimmungen für modularisierte Studiengänge dulde ich eine Überprüfung der Thesis mittels Anti-Plagiatssoftware.

Datum

Unterschrift